Quench Sensitivity in 6xxx Series Aluminium Alloys

A Thesis Submitted for the Degree of

Doctor of Philosophy

by

Katharina Strobel
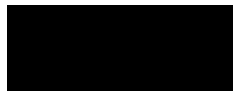
Department of Materials Engineering

Monash University

March 2013

Statement of Originality

This thesis does not contain material that has been submitted or accepted for the award of another degree, diploma or qualification at this or any other university or institution. To the best of my knowledge and belief, it does not contain any materials that have been previously published or written by any other person, except where dues reference is made in the text of the thesis.

Katharina Strobel

March 2013

Acknowledgements

I wish to acknowledge all the individuals and organisations that supported and assisted me in the completion of this PhD thesis. It is my pleasure to thank all of them, whilst the number is too large to mention each individually.

I would like to express my deepest gratitude to my supervisor Dr Mark Easton, for his guidance and support in this project. I highly value his guidance and patience, but probably value even more the trust and encouragement I experienced to pursue my own ideas and work independently.

Special thanks to Ms Lisa Sweet whose support, guidance and encouragement helped me greatly with completing my PhD. Further, I would like to acknowledge Dr Nick Parson, Dr Malcolm Couper and Prof. Jian-Feng Nie for the useful discussions throughout the course of my PhD study.

Great thanks go to Dr Matthew Lay for many fruitful discussions and proposing, conducting and analysing the positron lifetime annihilation spectroscopy (PALS) experiments at CSIRO Process Science and Engineering in Clayton. Additional thanks go to Dr Anita Hill for the very useful discussions of the PALS results.

I would also like to thank Dr Xinquan Zhang, A/Prof. Nick Birblis and Prof. Chris Davis for providing very useful feedback on my project as well as my development as a researcher.

Special thanks to Dr Suming Zhu, for his help with my initial transmission electron microscopy. I would also like to thank Dr Steve Pas for the uncomplicated training on the DSC, Ms Yeannette Lizama for the training on the equipment and Mr Graham Prior for his help with conducting experiments. I would also like to thank the staff of the

Abstract

Quench sensitivity, the dependence of strength and hardness on the cooling rate after extrusion or solution treatment, limits the applications of extrusions of heat treatable aluminium alloys. Reduced properties in slow cooled samples have long been attributed to the loss of solute on heterogeneous nucleation sites during cooling. While minimum cooling rates to avoid precipitation of Mg-Si-containing phases and reduced properties have been mapped out for a broad range of commercial alloys, little is understood about the physical mechanisms leading to quench sensitivity.

In this investigation the difference in hardness evolution between slow cooled and fast quenched samples of various commercial and model Al-Mg-Si alloys has been determined for a broad range of natural and artificial ageing times. This has demonstrated that the artificial ageing response of fast quenched samples differs greatly from the artificial ageing response of slow cooled samples. In contrast to fast cooled samples, where natural ageing has a negative effect, the artificial ageing response of slow cooled samples is less dependent on natural ageing time. As a result, hardness differences between fast and slow cooled samples is large during artificial ageing after short natural ageing times, but small after long natural ageing times, such that quench sensitivity strongly varies.

In order to explain this phenomenon, the cooling rate dependent microstructural development has been investigated using hardness measurements, electron microscopy (SEM and TEM), differential scanning calorimetry (DSC) and positron annihilation lifetime spectroscopy (PALS). From TEM investigations and theoretical considerations of the diffusion range it has been determined that solute is only lost from a limited region around the non-hardening precipitates forming during cooling on secondary dispersoids. The increased age hardening rate in fast cooled samples after short natural ageing times is therefore the result of a high vacancy supersaturation

rather than a high solute supersaturation compared to slow cooled samples. Non-equilibrium vacancies appear to act as precipitation sites for the precursor of the strengthening β''-precipitates. In slow cooled samples the formation of β''-precipitates seems to be suppressed.

In lean alloys with a low solute content, such as the investigated AA6060, the age hardening response is almost independent of the cooling rate. Small additions of Cu or changes in the Mg:Si-ratio in alloys with a combined Mg+Si-content greater than 1 wt.% have little effect on precipitation of non-hardening phases during cooling, but affect natural and artificial ageing behaviour.

The cooling rate after extrusion or solution treatment was also found to affect whether natural ageing has a negative effect or not. In fast cooled samples of Al-Mg-Si alloys with combined Mg+Si-contents greater than 1 wt.% the decrease in ageing kinetics due to the decrease of non-equilibrium vacancies with increasing natural ageing time contributes to the negative effect. In slow cooled samples the initial number of quenched-in vacancies is low, such that ageing kinetics are independent of the natural ageing time.

Publications and Presentations

Publications:

K. Strobel, L. Sweet, M.A. Easton, J.-F. Nie, M.J. Couper; Dispersoid Phases in 6xxx Series Aluminium Alloys, The 7th Pacific Rim International Conference on Advanced Materials and Processing Proceedings, Cairns, Australia, 2010.

K. Strobel, M.A. Easton, L. Sweet, M.J. Couper, J.-F. Nie; Relating Quench Sensitivity to Microstructure in 6000 Series Aluminium Alloys. Mater T, 2011 (52), pp. 914.

K. Strobel, M.A. Easton, L. Sweet, N.C. Parson; The effect of natural ageing on quench sensitivity in Al-Mg-Si alloys, 13th International Conference on Alumium Alloys Proceedings. Pittsburgh, USA, 2012.

K. Strobel, M.D.H. Lay, M.A. Easton, L. Sweet, S. Zhu, N.C. Parson, A.J. Hill; Effects of quench rate and natural ageing on age hardening behaviour of the aluminium alloy AA6060, in preparation

Presentations:

The 7th Pacific Rim International Conference on Advanced Materials and Processing
Cairns, Australia, 2nd-6th August 2010

The 12th International Conference on Aluminium Alloys
Yokohama, Japan, 5th-9th September 2010

The 13th International Conference on Aluminium Alloys
Pittsburgh, USA, 3rd-7th June 2012

Table of Contents

List of Figures

List of Tables

Chapter 1   Introduction

Aluminium is a light metal that is abundantly available, has a low density of 2.7 g/cm^3 and shows good thermal and electrical conductivity and excellent corrosion resistance in most environments. Its alloys combine a number of favourable properties such as a high strength-to-weight ratio, durability, good formability, corrosion resistance and recyclability. These characteristics and the possibility of weight reduction and hence energy savings make aluminium a popular choice for applications in road-, air- and sea-transport, construction and building, packaging and electronics.

Aluminium and its alloys have been used commercially since 1888 and production volumes have increased steadily to approximately 50 million tons of primary aluminium worldwide in 2012 [1]. As a result the aluminium industry is versatile and highly developed. The current challenges in aluminium and aluminium alloy production are to create sustainable production processes and product lifecycles and provide products that meet the needs of modern society in highly competitive fields. In order to achieve these aims, much attention has been given to the recycling of aluminium products as remelting scrap requires only about 5 % of the energy needed to produce the same weight of metal from its ore bauxite. As aluminium alloys cannot be refined, i.e. alloying elements cannot be removed [2], the increasing recycling activities also require a great understanding of the role of alloying elements.

Economic advantages and sustainability of processes and products can also be achieved by optimising processing parameters and material properties in order to save energy and resources. One very cost-, energy- and resource-effective way to produce finished and semi-finished products is extrusion. 75-80 % of aluminium is used for wrought products [2], of which approximately 30 % precent are extruded. The relatively low tooling costs and short tooling lead times as well as the possibility of high production rates make it a versatile and economically interesting process.

Amongst the extrusion alloys, 6xxx series alloys are the most commonly used and the economically most important class. Compared to other aluminium alloys, 6xxx series alloys have lower strength than typical 7xxx and 2xxx series alloys, but find wide application due to their high corrosion resistance, good formability and good machinability. 6xxx series contain Mg and Si as the major alloying elements and gain their strength though precipitation of Mg-Si-phases during age hardening.

6xxx series aluminium alloys can be divided into two groups: there are the soft alloys that are characterised by a relatively low Mg and Si of combined less than 1 wt.% and beside Fe, a transition metal content below 0.1 wt.%. The other group are medium to high strength alloys, which contain combined Mg and Si contents higher than 1 wt.% and Mn and Cr between 0.1 and 0.6 wt.%. Despite the difference in Mg and Si content that leads to a different level of precipitation strengthening secondary dispersoids that form in the presence of Mn and Cr during homogenisation add to strength by retarding recrystallisation and grain growth.

The presence of these secondary dispersoids have also long been made responsible [3, 4] for the loss of properties due to reduced quench rates after extrusion or solution treatment. This phenomenon is referred to as quench sensitivity. Processing quench sensitive alloys requires complex and expensive quenching systems to guarantee consistently high cooling rates. However, high cooling rates result in distortion and internal stresses such that the maximum cooling rate is limited. As a result, the material properties of the fabricated piece of extrusion are reduced compared to the material properties achieved in laboratory settings, i.e. the material under-performs. In order to maximise the performance of the extruded products, both the alloys and the processing can be optimised.

These two areas have to be improved simultaneously. Therefore, it is firstly important to understand the physical processes occurring in the alloys during extrusion and the subsequent ageing treatment. The role of the different alloying elements is thereby of great interest. Secondly, the influence of processing parameters, the cooling rate, but

also the ageing treatment, consisting of natural and artificial ageing, where the final properties are developed have to be understood.

The aim of this work is therefore to

- determine which material characteristics contribute to quench sensitivity

- investigate the mechanisms that lead to the cooling rate related loss of strength and hardness in slow cooled materials

- derive a general concept of how the different factors contributing to quench sensitivity and offers a basis for physical models

In this thesis a review of the current literature is presented in **Chapter 2**. Firstly, the characteristics or Al-Mg-Si alloys and their commercial versions, the 6xxx series alloys, as well as the typical processing route the produce extrusions of these alloys are discussed. Subsequently, history and current state of studying quench sensitivity in age hardenable aluminium alloys is presented. This includes the physical mechanisms that have been made responsible for quench sensitivity in literature, in particular sloute loss to secondary dispersoids. As it is proposed that this is not the only mechanism affecting quench sensitivity, the current literature on precipitation of strengthening phases, with particular focus on the role of non-equilibrium vacancies, is discussed in detail.

In **Chapter 3** the material, techniques and methodologies applied are explained in detail. Hardness measurements during artificial ageing after various natural ageing times are applied to map the influence of cooling rate on mechanical properties. To investigate the microstructure, electron microscopy (SEM and TEM) as well as positron annihilation lifetime spectroscopy (PALS) is employed. Thermal properties are determined by differential scanning calorimetry (DSC).

A preliminary investigation of commercial 6xxx series alloys is presented in **Chapter 4**. It is shown that solute loss is responsible for quench sensitivity after prolonged natural

ageing times. Solute loss is found to be predominantly dependent on the number density of heterogeneous precipitation sites, which are mainly secondary dispersoids. However, as prolonged natural ageing is known to have a negative effect in some Al-Mg-Si alloys, quench sensitivity has to be investigated after short natural ageing times as well. Furthermore, the lean commercial alloys AA6060 shows quench sensitivity that appears to be unrelated to solute loss.

In **Chapters 5 and 6** the age hardening response is therefore investigated in samples quenched at different rates in the soft, commercial alloy AA6060 and a model alloy similar to AA6061, respectively. Through TEM and DSC investigations the contribution of solute loss can be quantified. The remaining difference in hardness is then attributed to the significant role of quenched-in vacancies in quench sensitivity and quench sensitivity changing with natural ageing time.

As both Cu-additions as well as low Mg:Si-rations are known to have an effect on age-hardening response including the formation of meta-stable phases like β' and Q', the role of alloying elements is investigated in **Chapter 7** in the same way as in Chapters 5 & 6. The changes in alloying additions are found to have a stronger effect on the artificial ageing response than on solute loss.

In **Chapter 8** the results of the previous chapters are rationalised and a general explanation of quench sensitivity is given.

Chapter 2   Literature Review

2.1 Introduction

This chapter provides an introduction to quench sensitivity in 6xxx (Al-Mg-Si) series aluminium alloys. As a number of alloy features influence quench sensitivity [3, 5, 6], the role of the single alloying elements as well as the formation of different phases throughout the production process are discussed first. After that the current knowledge about quench sensitivity is outlined and methods to investigate quench sensitivity are discussed critically. Finally, precipitation reactions occurring during cooling as well as precipitation of strengthening phases during natural and artificial ageing is reviewed in detail emphasising their importance in quench sensitivity.

2.2 6xxx series alloys

6xxx series alloys are the commercial, age hardenable medium strength aluminium alloys with Mg and Si as the major alloying elements. These alloys combine several desirable properties such as good corrosion resistance, good weldability, excellent surface properties and a relatively low cost [2]. They are mainly produced as extrusions, with sheet products being increasingly used as automotive body panels [2].

Amongst the 6xxx series alloys, there is a distinction between low-strength alloys on the one hand and medium- to high-strength alloys on the other. Low-strength alloys such as AA6060 and AA6063 contain low levels of the strengthening phase forming elements Mg and Si. Medium- to high-strength 6xxx series alloys such as AA6005, AA6061 and AA6082, contain higher amounts of Mg and Si, often in a Mg/Si-ratio significantly smaller than 1.73 (in wt%), the ratio of the equilibrium Mg_2Si phase, and relatively high amounts of the transition metals Mn and/or Cr.
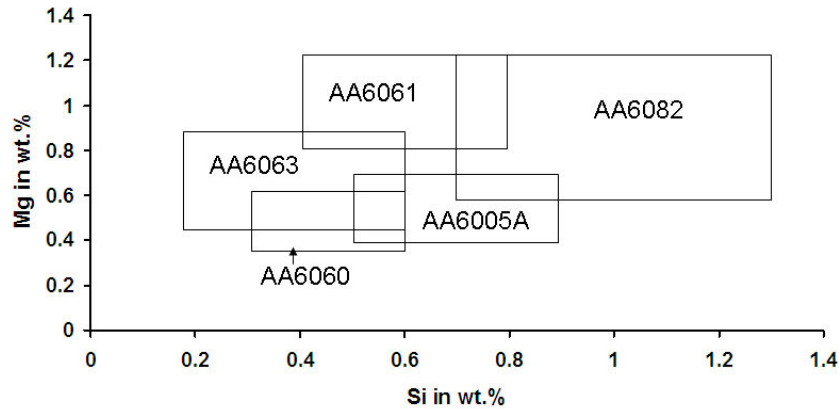
Figure 2-1 Mg and Si composition ranges of common 6xxx series extrusion alloys.

Table 2-1 gives an overview of the composition ranges of the most commonly used 6xxx series extrusion alloys. The main differences are in the content of strengthening elements (Mg, Si and Cu) as well as the content of transition metals (Fe, Mn and Cr).

Table 2-1 composition limits, minimum required and typical tensile strength for commercial 6xxx series alloys [7].

	Si	Mg	Fe	Mn	Cr	Cu	UTS$_{min}$ [MPa][8]	typical UTS [MPa]
AA6060	0.3-0.6	0.35-0.6	0.1-0.3	0.1	0.05	0.1	150 (T5)	
AA6063	0.2-0.6	0.45-0.9	0.35	0.1	0.1	0.1	205	245[2]
AA6005A	0.5-0.9	0.4-0.7	0.35	0.5	0.3	0.3	265	
AA6061	0.4-0.8	0.8-1.2	0.7	0.15	0.04-0.35	0.15-0.4	260	310[8]
AA6082	0.7-1.3	0.6-1.2	0.5	0.4-1.0	0.25	0.1	295	

2.2.1 Role of alloying elements

Alloying elements in 6xxx series alloys can generally be divided into strengthening phase forming elements and elements that form intermetallic phases.

- <u>Magnesium</u> has a relatively high solubility in Al and contributes considerably to solid solution strengthening. Therefore, high levels of Mg in solution require

increased extrusion pressures. Its main purpose is to form strengthening precipitates.

- Silicon is involved in both the formation of Fe-containing intermetallics and strengthening precipitates. As the composition of the strengthening β''-precipitates was found to be close to 1:1 in at.% [9-11] as opposed to the composition of the equilibrium β-Mg_2Si-phase higher Si contents are used in modern alloys [12]. Additions of Si in excess of the Si required to form Mg_2Si are here referred to as "excess Si". However, high amounts of Si can lead to precipitation of (Si) on grain boundaries and cause embrittlement.

- Iron is found as an impurity in primary aluminium and accumulates in recycled material. It has a very low solubility in solid aluminium and is therefore found in primary intermetallics and secondary dispersoids.

- Manganese is added in relatively low amounts in the order of 0.05 wt.% to enhance the formation of desirable α-Al(FeMn)Si intermetallics [13-15]. If added in higher amounts (about 0.3-0.7 wt.%) its presence leads to the formation of a significant number of secondary α-$Al_{15}(MnFe)_3Si_2$ dispersoids during homogenisation, which affect recrystallisation after extrusion, toughness and quench sensitivity.

- The presence of low amounts of chromium leads, similarly to Mn, to the formation of secondary dispersoids. However, much lower additions of Cr are sufficient to achieve similar dispersoid densities compared to Mn. Furthermore, additions of Cr are necessary in Cu containing alloys to improve corrosion.

- Copper was found to improve the strengthening response, but has a negative effect on corrosion [4]. In 6xxx series extrusion alloys it is only added in small amounts (≤ 0.4 wt.%).

2.2.2 Low strength 6xxx series alloys

Low strength alloys, e.g. AA6060 and AA6063, are the most widely used aluminium extrusion alloys. They contain a combined Mg and Si amount between 0.8 and 1.2 wt.% balanced to the equilibrium Mg_2Si-phase. Mn is added in very small amounts (about 0.05 wt.%) to promote the precipitation of the Chinese-script like α-Al_{12}(FeMn)$_3$Si intermetallic over the facetted β-Al_5FeSi [13-15]. Due to the low transition metal content, low strength 6xxx series alloys contain only a very small amount of secondary dispersoids. As a result, they show a fully recrystallised microstructure after extrusion and little quench sensitivity.

These alloys show good extrudability, allowing high extrusion speeds and low cooling rates after extrusion. It is also well known that room temperature storage has a positive effect on the artificial ageing response of alloys with a low Mg- and Si-content. They find wide use in architectural and decorative applications such as windows, doors and interior fittings. Due to their relatively low strength they are not used for structural applications.

2.2.3 Medium to high strength 6xxx series alloys

Medium to high strength alloys contain combined Mg and Si amounts in excess of 1.4 wt%. The improved mechanical properties compared to lower strength alloys allow a wide range of applications in transport-, nautical- and aerospace engineering. To achieve higher strength either Si- contents are chosen in excess of the balanced Mg_2Si-ratio or up to 0.4 wt.% Cu are added. These alloys also contain relatively high amounts of Mn and Cr, which improve corrosion resistance in Cu containing alloys (Cr) and form secondary dispersoids. Secondary dispersoids reduce embrittlement by retarding recrystallisation hence guaranteeing a small grain size and promoting intra-granular precipitation of Si. However, secondary dispersoids also promote the precipitation of Mg-Si-phases during cooling and hence lead to quench sensitivity.

High amounts of alloying additions not only lead to higher flow stress, but also reduce the temperature window between Mg_2Si solvus and solidus. Therefore, the

extrudability of medium to high strength alloys is reduced compared to low strength 6xxx series alloys.

2.3 Production process

In this section, the microstructural evolution from the liquid melt to the precipitation hardened product is presented along with the production process of common 6xxx series extrusions. A schematic of the production process and microstructural development for a dispersoid-containing medium to high strength 6xxx series alloy is shown in Figure 2-2.
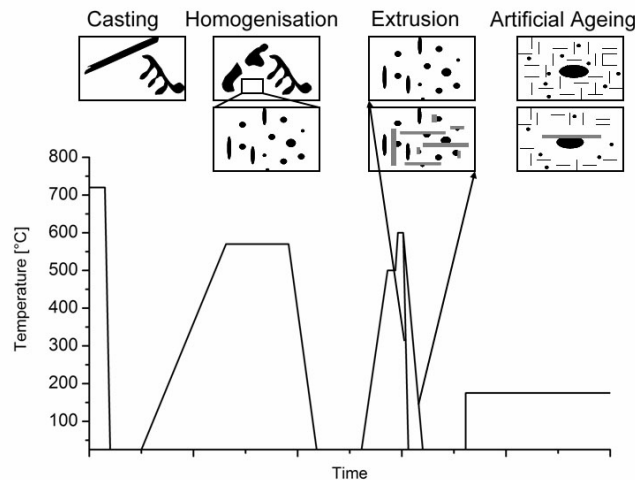
Figure 2-2 Schematic of the production process and microstructural development on a medium to high strength 6xxx series alloy.

2.3.1 Casting

Round billets are typically direct chill (DC) cast and generally show a dendritic, equiaxed structure. High cooling rates between 1 – 5 K/s lead to non-equilibrium cooling, such that billets show extensive macro and microsegregation. Macrosegregation is mainly found at a surface segregation zone, which is about 300 µm and is characterised by coarse constituent particles of about 100 µm in size [16, 17], as well as the centreline of the billet [18], where large floating grains

accumulate leading to inverse segregation in the centre (depletion in eutectic elements and enrichment in peritectic elements).

Microsegregation occurs in interdendritic regions when coarse intermetallic phases form in eutectic reactions from the last liquid to solidify at temperatures as low as 500ºC [16]. Depending on the alloy composition these intermetallic phases are α-$Al_{12}Fe_3Si$ or α-$Al_{19}Fe_4MnSi_2$, α_h-Al_8Fe_2Si, β-Al_5FeSi, Mg_2Si and π-$Al_8FeMg_3Si_6$ [19]. Their average size ranges between 1-100 μm. Further microsegregation is found in the distribution of alloying elements in solid solution. While the eutectic elements such as Mg, Cu and Si tend to segregate towards the dendrite boundaries, the peritectic elements such as Cr segregate towards the centre [16].

2.3.2 Homogenisation

Casting is followed by the homogenisation heat treatment process. The overall aim is to remove the undesirable features of the as-cast microstructure and prepare it for extrusion. The aims of the homogenisation process are:

- Dissolution of low melting eutectics

- Spherodisation of intermetallics

- Removing concentration gradients within grains

- Transformation of β-AlFeSi into α-AlFeSi

- Precipitation of secondary dispersoids

The process parameters, i.e. heating and cooling rate as well as homogenisation time and temperature have to be chosen to cater for all the above mentioned aims. A typical homogenisation heat treatment therefore consists of slow heating (at about 3ºC/min) to homogenisation temperatures around 570ºC. The alloys are commonly held (soaked) for about 2 h at the homogenisation temperature.

Particular care has to be applied during cooling after homogenisation as Mg-Si-containing phases precipitate at temperatures below the Mg_2Si solvus. On the one hand, the cooling rate has to be high enough to avoid precipitation of coarse β-Mg_2Si in favour of finer, lath-shaped β'-Mg-Si-phases, which dissolve much more readily during billet pre-heating before extrusion. On the other hand, if all Mg and Si are kept in solid solution, due to high cooling rates, flow stresses during extrusion are significantly increased [20]. A typical cooling rate for this processing step is $3 - 10$ºC/min [16]. Precipitation occurring during cooling after homogenisation is similar to precipitation occurring during quenching after extrusion (although cooling rates are different), so that work published on this processing step is of relevance to quench sensitivity.

2.3.3 Extrusion

Extrusion is successful when required mechanical properties, good surface quality, good anodising response and dimensional tolerances are achieved at high speeds in an economically viable process [16]. The main variable is the required flow stress which depends on alloy composition and microstructure of the ingot. After the extrusion process it is important to have the maximum possible amount of Mg and Si in solid solution available for the precipitation of strengthening phases. The extrusion process can be divided into three major steps: billet pre-heating, deformation and quenching.

- Billet pre-heating is done to lower the flow stress for the deformation process. Billets can be pre-heated to temperatures above the solvus temperature, so that Mg-Si-phases are dissolved before deformation. Alternatively, they are pre-heated below the solvus temperature and solution of undesirable Mg-Si-phases occurs once the temperature increases above the solvus during deformation heating [4].

- Easy deformation of the pre-heated billets requires low flow stresses, which are present when Mg levels are low and temperatures high. High extrusion speeds are economically desirable and lead to deformation heating. However, in alloys

where solvus and solidus temperatures are close together, low extrusion speeds have to be chosen to avoid deformation heating and prevent incipient melting. Too much deformation heating could result in surface liquidation and hence poor surface finish.

- Depending on the alloy composition, <u>quenching</u> after extrusion is performed to avoid precipitation of Mg-Si-containing phases, which would lead to a reduced ageing response (quench sensitivity). However, the maximum cooling rate is somewhat limited as distortion of the extruded section, which is likely to occur at high cooling rates, has to be avoided.

2.3.4 Age hardening

Age hardening after extrusion is typically conducted in two steps: natural ageing, that occurs during room temperature storage and artificial ageing at elevated temperatures. In contrast to 6xxx series alloys that are used in automotive body sheet applications and therefore experience natural ageing for several weeks, most extruded products are artificially aged within a few hours after extrusion. While natural ageing is known to have a negative effect at least on alloys containing Mg+Si > 1wt.%, the process set up - artificial ageing is mostly conducted in batches of several extrusions - dictates natural ageing times between 30 min and 4 h. During the subsequent artificial ageing process the aim is to precipitate a high number of fine β''-precipitates. Artificial ageing temperatures are chosen between 150 – 200ºC. Higher temperatures result in a fast hardness increase but lower peak hardness compared to lower temperatures, which lead to higher peak hardness values after longer artificial ageing times.

2.4 Quench Sensitivity

Quench sensitivity is loosely defined as the dependence of material properties after age-hardening on quench rates after extrusion or solution treatment. It can affect mechanical properties such as strength, hardness and fracture toughness as well as the electro chemical properties corrosion and anodising response. Quench sensitivity is

attributed to precipitation of the strengthening phase forming elements during cooling at reduced rates and the reduced concentration of mobile, non-equilibrium vacancies ("quenched-in vacancies") as a result of slow cooling [3, 5, 6, 21, 22]. Quench sensitivity is therefore explained by the age-hardenable nature of the affected alloys and depends on the stability of the supersaturated solid solution below solution treatment or extrusion exit temperature [23].

2.4.1 Definition of quench sensitivity

The most general definition of quench sensitivity is the loss of mechanical properties after artificial ageing due to reduced cooling rates after extrusion or solution treatment [23].

However, in contrast to mechanical properties like strength, hardness or impact toughness, where an absolute value can be determined using standardised methods, quench sensitivity is always relative and generally depends on a large number of variables, relating to alloy composition, processing parameters and the treatment after quenching. It is therefore of great importance to define adequate measures that reduce the number of variables, are generally applicable and can be determined using simple experiments.

Quench sensitivity has been defined as the absolute loss in property as a function of reducing quench rate or logarithm of quench rate [24, 25] or as a relative loss of properties by normalising with the maximum loss for very slow quench rates [26].

A more practical measure is the critical cooling rate, which is defined as the cooling rate necessary to achieve 95 % of the properties of the water quenched material [8, 23]. Analogously, critical cooling times, defined as the maximum time a sample can spend between two chosen temperatures, e.g. 400 and 300ºC [23], to reach 95 % of the properties of a water quenched sample are used to compare different alloys and investigate the influence of alloy composition.

In order to discuss quench sensitivity the underlying physical process will be discussed first. Subsequently, qualitative studies investigating the effects of alloy characteristics on quench sensitivity are discussed. In order to avoid quench sensitivity a large number of studies have been conducted to quantify quench sensitivity and offer solutions to improve industrial practice. The value of these studies is discussed to finalise this section.

2.4.2 Physical processes behind quench sensitivity

Quench sensitivity originates in the age hardenable nature of 6xxx series alloys. In order to successfully form strengthening precipitates during age hardening it is required for the material to have a large amount of solute temporarily in the matrix forming a supersaturated solid solution before the start of age hardening. The instability of the supersaturated solid solution not only allows precipitation hardening, but also makes the alloy susceptible to precipitation of coarser Mg- and Si-containing phases during cooling after solution treatment or extrusion. The following paragraphs outline fundamental processes that are the basis for quench sensitivity.

Precipitation of a second phase consists of two processes: nucleation and growth. The formation of a nucleus involves the creation of a matrix/nucleus interface which leads to an activation energy barrier. The free energy change associated with homogeneous nucleation has the following three contributors: the reduction of the volume free energy ($V\Delta G_V$) - ΔG_V representing the chemical driving force - due to the creation of a volume V of the nucleating phase, the increase of free energy due to the formation of an interface of the area A ($A\gamma$) and the increase of free energy due to the misfit strain energy (ΔG_S) per unit volume of the nucleating phase. The total free energy change is given by

$$\Delta G = -V\Delta G_V + A\gamma + V\Delta G_S \qquad \text{2-1}$$

The volume free energy ΔG_V is a measure for the stability of the supersaturated solid solution and depends on the amount and solubility of solute in the supersaturated solid solution. Figure 2-3 illustrates the effect of alloy composition on the nucleation

rate, which in itself is the product of the rate at which a nucleus can be made supercritical and the concentration of a critical-sized nucleus. It should be noticed that the nucleation rate for an alloy with a low solute concentration is always less than for an alloy with a high concentration of solute. Therefore, the relatively high Mg and Si content in medium to high strength 6xxx series alloys promotes nucleation during cooling by increasing the driving force for nucleation. A high driving force additionally enhances the growth of precipitates as, for a given time, the growth rate is proportional to the supersaturation.
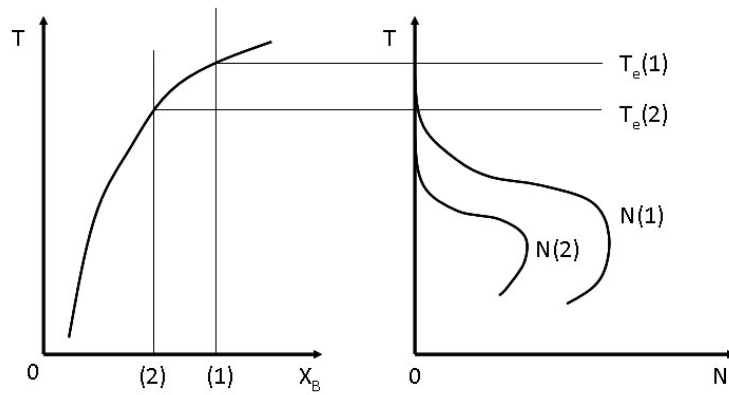
Figure 2-3 Effect of alloy composition on the nucleation rate during homogeneous nucleation. The nucleation rate in alloy 2 is always less than in alloy 1 [27].

Precipitation in commercial alloys is almost always heterogeneous. The activation energy barrier for heterogeneous nucleation is lowered by some free energy (ΔG_d), which is released when nucleation results in the destruction of a non-equilibrium defect.

$$\Delta G_{het} = -V(\Delta G_V - \Delta G_S) + A\gamma - \Delta G_d \qquad 2\text{-}2$$

In commercial 6xxx series alloys during cooling, such defects acting as heterogeneous nucleation sites can be (in order of increasing ΔG_d) excess vacancies, dislocations, stacking faults and grain boundaries and interphase boundaries, in particular the matrix/dispersoid interface [27]. While the number density of incoherent Mn- and Cr-containing dispersoids is low in low strength 6xxx series alloys, these dispersoids cause

significant precipitation in medium to high strength 6xxx series alloys. Their formation and structure are outlined in section 2.4.3.2.

The effect of both solute content and number of nucleation sites is summarised schematically in time-temperature-property (TTP) curves in Figure 2-4. The characteristic C-shape is typical for diffusion controlled precipitation processes, where nucleation rates are low at high temperatures due to the high solubility and low as well at low temperatures due to the reduced diffusivity. The curves represent the critical time spent at a given temperature to achieve certain properties, e.g. T6 strength, corrosion or fracture toughness. In 6xxx series aluminium alloys an increase in nucleation sites, i.e. dispersoids or grain boundary area, the original curve (solid line) is shifted to shorter times (dashed line). A reduction in solute content results in a shift to lower temperatures and longer times (dotted line).
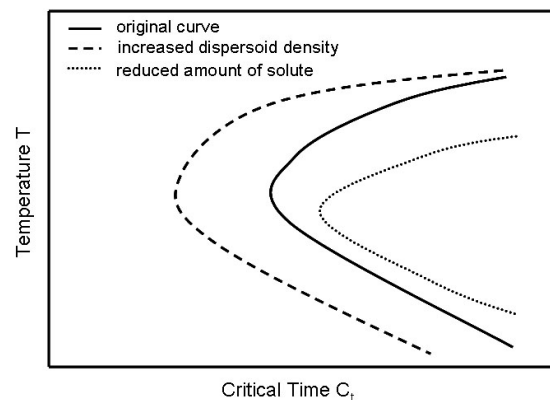
Figure 2-4 Schematic time temperature property (TTP) C-curves highlighting the influence of heterogeneous nucleation sites and amount of solute.

As 6xxx series aluminium alloys gain their strength mainly from precipitates formed during artificial ageing, section 2.5 discusses the fundamentals of this process as well as areas affected by reduced quench rates.

2.4.3 Qualitative studies on quench sensitivity

Amongst 6xxx series extrusion alloys medium- to high strength alloys are known to be significantly more susceptible to quench sensitivity than low strength alloys. The two major differences affecting this susceptibility are increased Mg and Si levels [5], which

affects the driving force for precipitate nucleation and growth, as well as additions of the transition metals Mn and Cr [3, 28], which form dispersoids that act as heterogeneous nucleation sites [3, 29]. Especially in early studies quench sensitivity has further been attributed to varying concentrations of "quenched-in", non-equilibrium vacancies, which leads to differences in diffusion during natural and artificial ageing. The state of the current knowledge of these three factors will be discussed in the following sections.

2.4.3.1 Influence of solute content

There are only a limited number of studies investigating the influence of Mg and Si on quench sensitivity. Zoller and Ried [4] compared the quench sensitivity of a range of alloys and found that an increase in the combined Mg+Si content increases quench sensitivity while the Mg/Si-ratio seems to have no effect. From theoretical considerations they concluded that the solubility of Mg and Si drops sharply with temperature at increasing Mg content leading to a significant increase in quench sensitivity. Although an increase in Si content also leads higher quench sensitivity, it is somewhat compensated by the increased strength level.

These findings are supported by Bratland et al.'s [26] model predictions. They compared three AA6082-type alloys that varied in Si content and therefore in Mg/Si ratio. For the alloy with a medium Si content their model predicted an unexpectedly high dispersoid number density. Independent of that, the alloy with the lowest Si-content showed the lowest quench sensitivity, i.e. loss of properties, whereas the alloy with the highest Si-content was predicted to show the highest yield strength over the range of cooling rates (Figure 2-7).

2.4.3.2 Influence of secondary dispersoids

It has been known for a long time that Al-Mg-Si alloys containing transition metals are more susceptible to quench sensitivity [4]. This is largely attributed to the formation of secondary dispersoids during heating to homogenisation temperature.

- • Dispersoid formation

In the presence of Si, Fe as an impurity and other transition metals - in the investigated alloys Mn and Cr - secondary dispersoid phases precipitate during the heating phase of homogenisation treatment [30-32]. Lodgaard and Ryum investigated the formation of dispersoids in the presence of Mn, Mn and Cr and Cr [31, 33-35]. By combining up-quenching experiments with microstructural investigations and phase identifications they were able to establish a precipitation sequence for dispersoids (Figure 2-5). Metastable β'-Mg-Si-phases form homogeneously at temperatures between 100-350ºC. An intermediate phase, the hexagonal "u-phase" with a = b = 6.70 Å and c = 8.08 Å, forms on the dissolving β'-Mg-Si-phase at temperatures above 350ºC. At increasing temperatures β'-Mg-Si has dissolved completely and the dispersoid precipitates homogeneously on the matrix/"u-phase" interface. Eventually the dispersoids consume the "u-phase" completely.
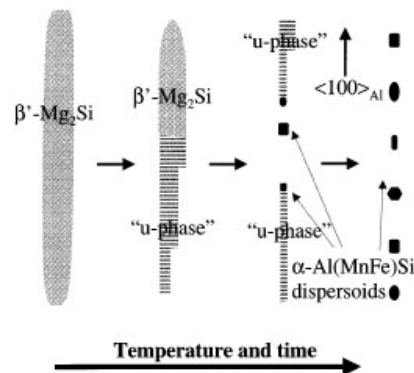
Figure 2-5 Model for precipitation of secondary dispersoids according to Lodgaard and Ryum [31].

As the precipitation of dispersoids occurs in a complex sequence, heating to homogenisation temperature has to be performed at relatively low heating rates at a maximum of 3 K/min in order to achieve a homogeneous dispersoid distribution [30, 33, 34].

The composition, crystal structure and number density of dispersoids strongly depend on the alloy composition (Table 2-2). While there are dispersoids forming in Fe-free alloys Mn-containing Al-Mg-Si alloys, there are no dispersoids in Fe-free Cr-containing

Al-Mg-Si alloys [32]. This might be due to all dispersoid phases being related to the simple cubic $Al_{15}Mn_3Si_2$-phase with a = 12.6 Å [23, 29].

Table 2-2 Mn- and Cr-containing dispersoids forming in Al-Mg-Si and related alloys.

Alloy Type	Proposed Dispersoid Phases	Crystal Structure	Source
Al + Mg + Si + Fe + Mn	α-$Al_{12}(MnFe)_3Si$ when Mn:Fe <1.6 at.%	bcc, a=1.26 nm	[31, 36]
	α-$Al_{15}(MnFe)_3Si_2$	sc, a=1.26 nm	
Al + Mg + Si + Fe + Mn + Cr	α-Al(MnCrFe)Si	cubic, a=1.26 nm	[31]
Al + Mg + Si + Fe + Cr	α-Al(CrFe)Si	bcc/sc, a=1.26 nm	[34]
	α'-AlCrSi for Cr > 0.3wt.%	fcc, a=1.09 nm	

When the Fe content exceeds a certain limit (Mn/Fe<1.6 [29]) the body-centred cubic α-$Al_{12}Fe_3Si$-phase precipitates [29] and Fe, Cr and Mn have a certain solubility in the respective other phase. All these dispersoid phases, however, have the same lattice parameter (a = 12.6 Å) so that all phases have the same mismatch with the matrix. Only at Cr-contents greater than 0.3 wt% does this change with the α'-$Al_{13}Cr_4Si_4$ phase forming which has a smaller lattice spacing of 10.9 Å [34].

- Effect on quench sensitivity

As the dispersoid/matrix interface is very similar in common 6xxx series alloys at practical homogenisation treatments, the number density is the quench sensitivity determining dispersoid characteristic. It is determined by homogenisation time and temperature as well as Mn and Cr content [3, 28]. Significant coarsening of dispersoids occurs during the homogenisation soak, such that a high number density of small dispersoids is found after homogenisation at low temperatures (e.g. 4 h at 520ºC) compared to at higher temperatures (e.g. 3 h at 580ºC), resulting in a dispersoid density of $24 \pm 4 \, 10^9/mm^3$ and $7 \pm 3 \, 10^9/mm^3$ respectively for an alloy containing about 1 wt% Si, 0.6 wt% Mg, 0.2 wt% Fe and 0.56 wt% Mn [3]. Model predictions confirmed the increase in quench sensitivity due to a higher dispersoid number density

[26]. The number density of dispersoids is also increased by an increase in the amount of transition metal [23], leading to an increase in quench sensitivity.

Mn-containing dispersoids appear to be more prone to coarsening than Cr-containing dispersoids [3]. This might be one of the reasons why Cr is about three times as potent in forming dispersoids as Mn. Another reason is that Cr as opposed to Mn is not involved in the formation of primary intermetallics.

2.4.3.3 Role of quenched-in vacancies

Early studies on quench sensitivity and also on natural ageing considered the effect of quenched-in vacancies on quench sensitivity [21-23]. While studying parameters affecting the natural and artificial ageing behaviour Pashley et al. [22] were well aware of the enhancing effect of quenched-in vacancies on natural ageing kinetics. Therefore, they reduced the quench rate after solution treatment in order to reduce vacancy concentration and hence a quench-rate and natural ageing time dependency of clustering kinetics. It was not until the 2000s that further detailed investigations on the role of quenched-in vacancies in precipitation followed [37-39].

In this context, it has to be clarified that the vacancies of interest are mobile, non-equilibrium vacancies, also referred to as "quenched-in vacancies" (as their presence is the result of cooling above the equilibrium cooling rate) or "excess vacancies" (as their concentration is in excess of the equilibrium vacancy concentration). The equilibrium vacancy concentration of aluminium alloys at 25ºC is in the order of magnitude of 10^{-11}-10^{-12} per atom [39, 40].

In recent years various studies have focused on the temperature- and cooling-rate-dependence of vacancy concentration [37, 39, 41] and the role of vacancies in the decomposition of the solid solution in aluminium alloys [42-44]. Based on the model derived by Fischer et al. [41], which describes annihilation of excess vacancies on different types of sinks, Lang et al. [39] and Falahati et al. [37] determined the effect of cooling rate on excess vacancy concentration in an experimental alloy containing a very high Si-content [39] and the commercial Al-Mg-Si alloy AA6016 [37], respectively.

It becomes obvious from their calculations that the vacancy site fraction after quenching from solution treatment at 550ºC varies between 5×10^{-5} for a very fast quench rate of 10.000ºC/s and 2×10^{-9} for the very slow quench rate of 0.1ºC/s [37], and consequently varies by several orders of magnitude for industrial quench rates.

Mobile, non-equilibrium vacancies increase the diffusivity for self-diffusion of substitutional atoms by many orders of magnitude [27]. As the vacancy-solute binding energies of most solute atoms in aluminium are positive so that the solute atoms attract vacancies [45] the vacancy solute pair can diffuse through the lattice together. It should be noted that there are contradictory reports about whether the Mg-vacancy binding energy is positive or negative [40, 45].

The increased diffusivity of solute atoms due to the high number of mobile, non-equilibrium vacancies leads to a faster formation of a higher number density of precipitates [39, 46, 47]. As a result, fast cooled samples have a faster ageing response during natural ageing and depending on the natural ageing time also during subsequent artificial ageing. Vacancy annihilation and vacancy trapping result in a reduction of the concentration of mobile vacancies down to the equilibrium vacancy concentration over the course of about 100 h irrespective of the cooling rate [37, 39, 44, 48].

While studying the effect of cooling rate on subsequent precipitation in an Al-Zn-Mg alloy, Deschamps et al. [38] did not find a major influence of cooling rates between 5-200ºC/min on the precipitation kinetics. It should be noted, however, that their samples were naturally aged for 7 days, so that it has to be expected that most of the excess vacancies that would affect the precipitation kinetics had annihilated already during natural ageing. This highlights that the effect of quenched-in vacancies is dynamic and may change rapidly during room temperature storage.

The inclusion of the role of non-equilibrium vacancies in the discussion of quench sensitivity might be controversial as they do not affect mechanical properties during or immediately after cooling. However, as the quench-rate dependent concentration of

non-equilibrium vacancies affects the subsequent natural and artificial ageing responses in complex ways, it has to be considered when studying quench sensitivity.

2.4.3.4 Determining factors for quench sensitivity

Although there is a general agreement that both the number density of dispersoids as well as the amounts of the solute elements Mg and Si affect quench sensitivity, it remains difficult to separate and quantify the contribution of either effect. Figure 2-6 compares the Mg_2Si content and the transition metal content of a number of commercial 6xxx series alloys investigated by Milkereit [49] and Sweet et al. [8] and it can be seen that the transition metal content increases linearly with increasing Mg and Si contents. It has been taken into account that Cr was found to be three times as potent in forming dispersoids as Mn [3]. Therefore, only limited conclusions of the effect of either dispersoids or Mg and Si content on quench sensitivity can be drawn from these studies.
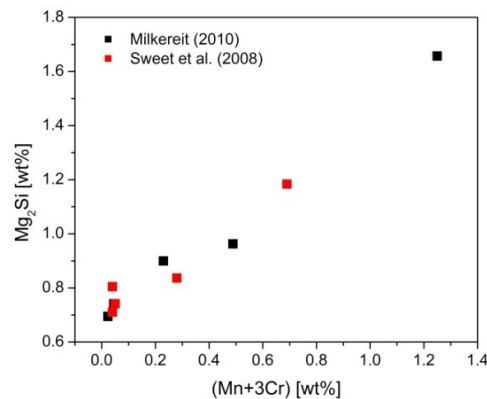
Figure 2-6 Relationship between content of strengthening precipitate forming elements and transition metals in various commercial 6xxx series alloys.

In order to evaluate single influencing factors it is, however, crucial to reduce the number of variables, i.e. conduct investigations using model alloys that only vary in the investigated variable. Furthermore, thought has to be given to the heat treatments homogenisation and ageing, as an alloys response to these treatments also depends on its composition.

A comprehensive comparison is given by Bratland et al. [26], who compared AA6082-type alloys with varying Si-contents of 0.92 wt.% Si (Alloy A), 1.32 wt.% Si (Alloy B) and 0.69 wt.% Si (Alloy C), and different homogenisation treatments by modelling their quench sensitivity. The alloys were homogenised at 580ºC and a second set of samples of Alloy A was homogenised at 530ºC (Alloy A2). Figure 2-7 shows a summary of Bratland et al.'s results, with Figure 2-7a showing a dimensionless strength ratio of the S/S_{max} which included the maximum strength after extrusion and age-hardening. It becomes clear that quench sensitivity is greatest in the alloy with the highest dispersoid number density (Alloy A2) caused by homogenisation treatment at lower temperatures (here 530ºC). This shows that the influence of the number density of dispersoids is more pronounced than the influence of varying Si contents, at least in the range of commercial practice.
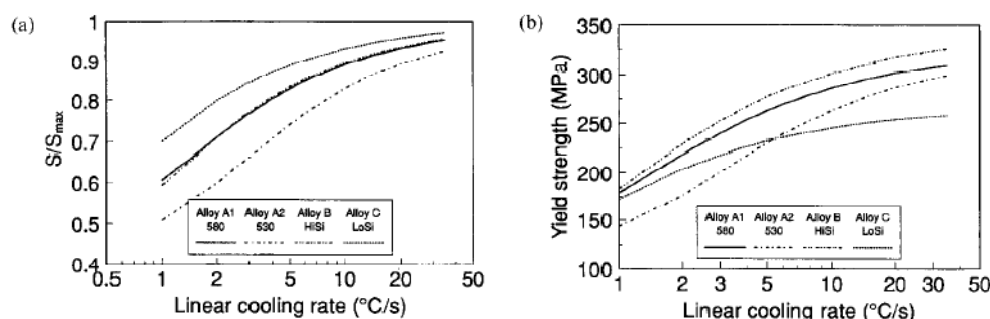
Figure 2-7 Summary of the results of Bratland et al. [26]. (a) Dimensionless yield strength ratio S/S$_{max}$ vs. cooling rate and (b) absolute yield strength vs. cooling rate.

Little remains known about the influence of the quench-rate dependent vacancy concentration on age hardening response. The considerations of Pashley et al. [22], demonstrating that the amount of vacancy supersaturation depends on the cooling rate and decreases during natural ageing, seem very reasonable. As a consequence, natural and artificial ageing kinetics are expected to vary greatly depending on cooling rate and room temperature storage time.

2.4.4 Methods to study quench sensitivity

From an industrial point of view determining the minimum cooling rate necessary to achieve the required properties is of great interest. Therefore, a number of different

approaches have been taken to determine cooling conditions required for certain alloys [5, 8, 50] with some studies including product shapes in their analysis [4]. The following section compares experimental to computational methods to determine minimum cooling rates including Jominy-type methods [8, 51, 52], determination of time-temperature-property (TTP-) diagrams [5, 49, 50, 53], and quench factor analysis [21, 51, 54-56].

2.4.4.1 Jominy-type methods

Based on the standard test method for determining hardenability of steel [57], commonly referred to as the Jominy Test, a number of quantitative end-quench tests have been developed to determine the dependence of hardening response on cooling rate from solution treatment temperature in aluminium alloys [8, 23, 58]. In the standardised Jominy Test [57] a cylindrical test piece with a diameter of 1 in (25.4 mm) and length of 4 in (101.6 mm) is quenched on one end by a vertical stream of water. For the standardised test piece quenched from 538ºC quench rates between 480ºC and 280ºC were determined to be between 4800ºC/min at the quenched end and 150ºC 63.5 mm from the quenched end [51, 59]. In order to guarantee the range of cooling rates equivalent to cooling rates encountered during commercial processing (about 15000ºC/min for WQ and 30ºC/min for air cooled samples [24]), the standardised Jominy Test has to be modified for aluminium alloys. In order to accommodate for the different heat transfer characteristics between steels and aluminium alloys longer bars are used [8, 58] and the end is quenched in different media or under reduced flow rates [8, 52]. Bomas [23] used a stack of 10 mm thick, test sample shaped, heat resistant steel pieces with Al-test samples sandwiched between them so that the Al samples were quenched at significantly different rates.

The results of a Jominy Test, typically T6 hardness as a function of distance from the quenched end or of cooling rate, can be used to determine the minimum quench rated required for certain properties [8] or as input data for quench factor analysis [51].

2.4.4.2 Time temperature precipitation curves

Time-temperature-precipitation (TTP) curves for age-hardenable aluminium alloys are similar to isothermal time-temperature-transformation (TTT) curves for steels. They are often referred to as C-curves because of their characteristic shape. TTP C-curves are constructed by quenching to a given temperature followed by isothermal holding. The amount precipitated for certain holding times are determined and plotted as a function of holding time and temperature. However, as the amount precipitated is often difficult to quantify, properties like corrosion, hardness or strength are usually determined. Depending on the purpose of the diagram, these properties are either determined immediately after quenching or after a subsequent ageing treatment [55].

Industrial cooling, however, occurs continuously, so that the application of isothermally recorded TTP C-curves is of limited use. Continuous-cooling-precipitation (CCP) curves, which are obtained from continuously cooled samples, e.g. from Jominy-end quench tests by a combination of metallographic and dilatometric methods. Differential scanning calorimetry (DSC) offers a fast way to obtain these diagrams [53, 60], especially because cooling rates can be chosen and information about the onset of phase transformations are readily available. In conjunction with microstructural analysis a holistic picture of precipitation during cooling can be generated.

The advantage of CCP diagrams is that key information for industrial processing, like minimum cooling rate to avoid precipitation as well as temperature ranges of precipitation are readily available. However, CCP diagrams only represent one specific alloy after specific homogenisation and deformation conditions and cannot be easily transferred. This applies especially in 6xxx series alloys, where small changes in alloy composition and processing conditions might have large affects on precipitation during cooling. It turn, its sensitivity to these parameters makes it a very useful tool to compare the effect of changes in composition of processing parameters on precipitation during cooling.

2.4.4.3 Quench factor analysis

Quench factor analysis (QFA), first developed by Evancho and Staley [21, 55], uses non-isothermal cooling curves and TTP C-curves to predict properties after continuous cooling depending on the quench rate. It can be used to predict various properties such as corrosion, toughness and strength and also design and optimise quench practice. The bases for the model are, on the one hand, the dependence of properties on transformation or precipitation reactions occurring during time spent at higher temperatures. On the other hand it is assumed that once phases have precipitated heterogeneously further phase transformations occur isokinetically, so that they can be treated as being additive [61].

During isothermal holding, growth kinetics can be described by an Avrami-type equation. The general form for diffusion controlled growth is

$$X = 1 - \exp[-(kt)^n] \qquad \text{2-3}$$

where k is a temperature dependent term, t the time at temperature and X the volume fraction transformed.

When transformation reactions occur isokinetically the amount transformed during continuous cooling τ can therefore be described by the integral

$$\tau = \int_{t_0}^{t_f} \frac{1}{C_t} dt \qquad \text{2-4}$$

where C_t is the critical time from a TTT C-curve, t a time from the cooling curve, t_0 the time at start of quench and t_f the time at finish of quench. For quench factor analysis it is assumed that the transformed fraction at any isothermal hold time is a fraction of the critical amount (X_c) and is equal to the quotient of the time spent at temperature (t) and the critical time at that temperature given by the C-curve.

$$\tau = \frac{X}{X_C} = \frac{t}{C_t} \qquad \text{2-5}$$

The integral in equation 2-4 can be evaluated by the method shown in Figure 2-8 and the fraction transformed τ is determined that way.
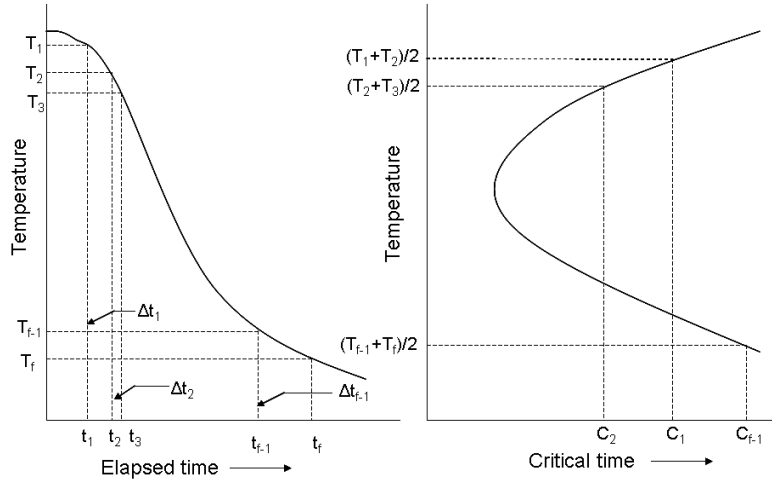
Figure 2-8 Method of determining the quench factor Q using a continuous cooling curve and a TTP C-curve according to [21, 55].

The fraction transformed is referred to as the quench factor Q and given by the following equation using the nomenclature specified in Figure 2-8.

$$Q = \Delta t_1 \frac{\Delta t_2}{C_2} + ... + \frac{\Delta t_{f-1}}{C_{f-1}} \qquad \text{2-6}$$

Although the originally proposed QFA was able to predict the development of strength after continuous quenching and could be used to design quenching systems [21, 55], it included a number of assumptions that were later found to be inconsistent with experimental and theoretical findings [54, 56].

Based on the theories of quench factor analysis an analytical description for TTP C-curves has been formulated

$$C_t = -k_1 k_2 \exp \frac{k_3 k_4^2}{RT(k_4 - T)^2} \exp \frac{k_5}{RT} \qquad \text{2-7}$$

where k_1 is the ln(fraction untransformed); k_2 is a constant related to the reciprocal of the number of nucleation sites; k_3 is a constant related to the energy required to form a nucleus; k_4 is a constant related to the solvus temperature; k_5 is a constant related to the activation energy for diffusion; R is the universal gas constant and T is the temperature.

While the constants k_4 and k_5 are related to physical data, k_1-k_3 have to be determined by fitting experimental data from interrupted quench and isothermal holding experiments which can be supplemented by continuous cooling experiments [62]. In response to the original QFA a number of authors proposed improvements [54, 56, 62]. Suggestions were made to either overcome mathematical pitfalls during the fitting of constants [62] or to describe the physical processes more realistically [54, 56].

QFA is a useful tool to determine post-quench properties or to optimise quenching procedures. Another of its advantages is that the quench factor Q gives a quantitative measure for quench sensitivity and allows comparisons on a quantitative basis. However, it requires a significant amount of experimental and theoretical work to determine the respective C-curves. The number of experiments can be reduced by performing continuous cooling experiments in DSC or especially in Jominy-type tests, rather than isothermal holding experiments [63]. Similarly to the purely experimentally determined TTP- or CCP-curves the simulated C-curves are also dependent on the processing parameters and alloy composition and not easily transferable.

2.4.4.4 Alternative measures

Aside from the major methods to study quench sensitivity presented above, a small number of other methods have been proposed to quantify quench sensitivity. The following methods aimed to characterise quench sensitivity with one value.

In 1971 Zoller and Ried [4] presented a guide for the development of Al-Mg-Si alloys with reduced quench sensitivity. As a measure for quench sensitivity they defined a critical half-life time τ_{crit} (which is needed to obtain minimum properties). Cooling of a profile with good thermal conductivity follows an exponential law:

$$T = T_K + (T_0 - T_K)\exp\left(-\frac{\ln 2}{\tau}t\right)$$
2-8

where T is the profile temperature at the time t, T_0 is the temperature when leaving the die, T_K is the temperature of the cooling medium and $\tau_{1/2}$ is the half-life time, i.e. the time it takes for the profile temperature to decrease from T_0 to half of T_0 and T_K. The half-life time is related to the heat transfer coefficient as follows:

$$\tau_{1/2} = c \cdot \frac{d}{\alpha}$$
2-9

(d is the wall thickness and c a form factor) Depending on the cross-section of the profile the form factor c is between 0.246 and 0.492 [4].
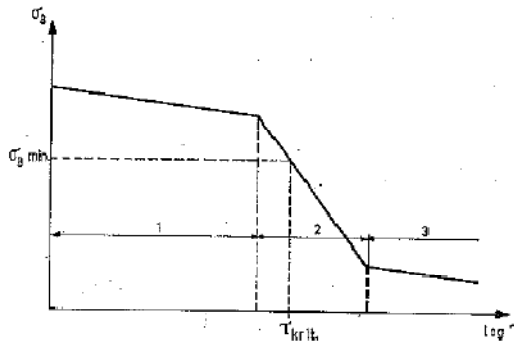
Figure 2-9 Schematic of the dependence of strength on the half-life time during cooling [4]. Strength decreases slowly in section 1 due to clustering at temperatures below 250ºC, strong decrease in strength during section 2 due to precipitation of Mg-Si phase and complete decomposition in section 3.

By including a form factor, this method is useful for industrial processing where cooling rates are very much influenced by the shape of the extrusion.

Zhang and Zheng [24] studied the cast-alloy A356 (Al-7%Si-0.4%Mg) by quenching samples in water at different temperatures and in still air and measuring the age hardening response and tensile properties. They found a logarithmic relationship between UTS (or σ_y) in T6 condition and the quench rate R.

$$UTS = A \log R + B \qquad \text{2-10}$$

Values of A and B were calculated using least-square regression method. The term A is a measure for quench sensitivity with the units MPa/log(ºC/s). A high value for A means a high quench sensitivity. The major advantage of this measure is that it is very easy to determine. However, a comparison of their own results to results from a previous study [64] gave very different results. This shows that the method is very sensitive to processing conditions and is therefore mainly useful to compare alloys after the same process conditions.

2.4.4.5 Summary

The above mentioned methods offer a number of ways to study quench sensitivity. There are generally two methods: those that offer one quantitative measure and those that map properties or precipitation reactions. The presented quantitative measures are the quench factor Q determined by QFA [21, 55], the half-life time τ [4] and the gradient A of the logarithmic relationship between UTS or σ_y and quench rate [24]. Temperature-time maps for precipitation reactions and properties, such as TTP and CCP curves, also offer valuable qualitative information about the processes occurring. The nose temperature of the C-curve, e.g., is related to the number of precipitation sites, while the equilibrium temperature is related to the amount of solute and hence the driving force for precipitation. Quench factor analysis has been the most popular method to study quench sensitivity, due to the broad information that can be gathered [21, 54-56, 63].

The general problem with studying quench sensitivity is the number of variables that have a direct influence. While the discussed methods are valuable in describing quench sensitivity at a certain state, they fail to offer a universal description which includes the

influences of processing parameters (homogenisation time and temperature, degree of deformation during extrusion, natural ageing time, artificial ageing time and temperature) and alloy composition.

2.5 Precipitation in age-hardenable alloys

In age-hardenable Al-alloys, such as Al-Cu-Mg (2xxx series), Al-Zn-Mg (7xxx series) and the alloys investigated in this work Al-Mg-Si (6xxx series), a number of different, consecutive precipitation reactions determine microstructure and hence properties. Precipitation reactions are governed by the fundamental processes of nucleation and growth, which often leads to transformation of the precipitate phase and is driven by diffusion.

2.5.1 The precipitation sequence in Al-Mg-Si alloys

Al-Mg-Si-alloys gain their strength mainly from Mg-Si-containing clusters and precipitates that form at room and elevated temperatures. The precipitation sequence for alloys with a Mg/Si ratio close to 2 (at.%) is widely accepted to be:

$$\text{SSSS} \rightarrow \text{clusters/co-clusters} \rightarrow \text{GP-zones} \rightarrow \beta'' \rightarrow \beta' \rightarrow \beta\text{-Mg}_2\text{Si}$$

As the Mg/Si-ratio in the major strengthening phase β'' was found to be approximately 1.5 to 2 at.% [9-11]   alloys with higher relative Si contents have been designed to improve hardness and strength. The resulting lower Mg/Si-ratio leads to the precipitation of additional phases:

$$\text{SSSS} \rightarrow \text{clusters/co-clusters} \rightarrow \text{GP-zones} \rightarrow \beta'' \rightarrow \text{Type A, Type B, } \beta', \text{ B}' \rightarrow$$
$$\beta\text{-Mg}_2\text{Si, (Si)}$$
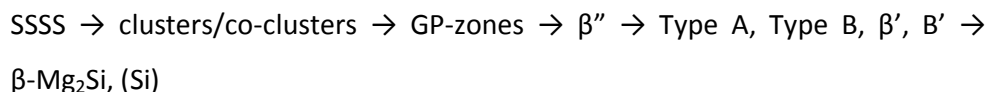
Similarly, additions of Cu increase strength and hardness. In alloys containing a Mg/Si-ratio close to 2 at.% and Cu-additions of commonly about 0.3-0.5 wt.% the precipitation sequence is described as [65-68]:

$$\text{SSSS} \rightarrow \text{clusters/co-clusters} \rightarrow \text{GP-zones} \rightarrow \beta'' \rightarrow \beta', Q' \rightarrow \beta\text{-Mg}_2\text{Si}, Q$$

The crystal structures of the precipitating phases is summarised in Table 2-3. While the crystal structure of GP-zones, the strengthening β"-phase and the equilibrium β-Mg$_2$Si are generally accepted, various crystal structures of the metastable β'-phase have been reported.

Table 2-3 Mg-Si-containing phases in Al-Mg-Si alloys [69].

Phase	Crystal structure	Mg/Si (wt.%)	Source
cluster	undefined	depending on alloy composition	
GP-zone	fcc based base-centred monoclinic, a = 14.78 Å, b = 4.05 Å, c = 6.74 Å, β= 106.8º, (Al+Mg)$_5$Si$_6$	0.72	[70]
β"	base centred momoclinic (C2/m), a = 15.16 Å, b = 4.05 Å, c = 6.74 Å, β = 105.3 Å, Mg$_5$Si$_6$	0.72	[9, 10]
β'	hexagonal, a = 4.07 Å, c = 4.05 Å	1.73	[71]
β'	hexagonal, a = 7.05 Å, c = 4.05 Å	1.73	[72, 73]
β'	hexagonal (P6$_3$/m), a = 7.15 Å, c = 12.15 Å, Mg$_9$Si$_5$	1.56	[74, 75]
Type A	hexagonal (P-62m), a = 4.05 Å, c = 6.70 Å, Al:Mg:Si = 4:1:5	0.27	[76]
U1	trigonal (P-3m1), a = b = 4.05 Å, c = 6.74 Å, MgAl$_2$Si$_2$	0.58	[77]
Type B	orthorhombic, a = 6.83 Å, b = 4.05 Å, c = 7.94 Å, Al:Mg:Si = 4:2:5	0.35	[76]
U2	orthorombic (Pnma), a = 6.74 Å, b = 4.05 Å, c = 7.94 Å, Al:Mg:Si = 4:4:4	0.87	[74]
Type C or B'	hexagonal, a = 10.4 Å, c = 4.05 Å	0.71	[76, 78]
β	cubic, a = 6.40 Å, Mg$_2$Si	1.73	[72]
Q'	hexagonal (P6$_3$),a = 10.32 Å, c = 4.05 Å	0.72	[65, 66]
Q	hexagonal (P-6), a = b = 10.39 Å, c = 4.02 Å, Al$_4$Cu$_2$Mg$_4$Si$_7$	0.99	[69, 79]

2.5.2 Clustering

The formation of clusters during room temperature storage has been of great scientific interest since it not only causes hardening but also affects subsequent ageing treatments.

Clusters can be defined as solute-rich groupings of atoms with undefined shape, chemistry and crystal structure [80]. They are part of the solid solution and may be present in between supersaturated matrix and equilibrium state [80]. In a more practical approach they are considered as particle too small to provide contrast in a (conventional) TEM image [81].

Wilm [82] discovered a hardness-increase during room temperature storage as early as 1911. It is therefore commonly referred to as natural ageing. It was only in the 1930's that Gunier and Preston were able to explain the hardness-increase with the formation of small, non-observable phases [83, 84]. A negative effect of clustering and hence room temperature storage on artificial ageing kinetics has been known since the 1960's [22, 85, 86] and was attributed to solute being lost to clusters resulting in less solute being available for the subsequent artificial ageing treatment. Bichsel and Ried [87] and Royset et al. [88] later linked the effect of natural ageing on artificial ageing to the Mg- and Si- content, such that a negative effect of natural ageing was only observed in alloys containing high Mg- and Si-contents and a positive effect is observed for alloys with low Mg- and Si-contents (Figure 2-10).
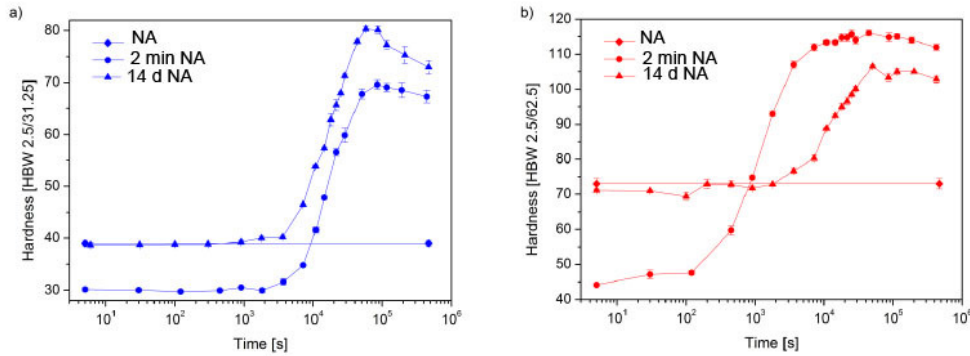
Figure 2-10 Hardness after long-term natural ageing (NA) and during artificial ageing at 170ºC after 2 min natural ageing and 14 d natural ageing in a) AA6060 and b) AA6061 [89].

In recent years the vast improvements in analysis techniques such as high resolution transmission electron microscopy (HRTEM) and three-dimensional (3-D) atom probe (3DAP) and positron annihilation lifetime spectroscopy (PALS) allowed detailed studies on formation, composition and effects of nano-sized clusters consisting of as little as 10 atoms or less.

2.5.2.1 Clustering in alloys with high Mg- and Si-contents (>1 wt.% Mg+Si)

From one- and three-dimensional atom probe data it has been suggested that several clusters form in the very early stages of natural ageing [11, 81]. These clusters are proposed to be separate clusters of Si atoms and clusters of Mg atoms [11, 81] that form possibly as early as during quenching. Chang and Banhart [90] observed three different clusters using low temperature differential scanning calorimetry DSC; the earliest cluster, referred to as C0, showing a very small peak at a temperature below 30ºC could correlate to these early clusters.

Co-clusters were found to form immediately after quenching at room temperatures [11, 81, 90, 91], possibly due to dissolution of Mg-clusters and diffusion of Mg into Si-clusters [11]. Chang and Banhart [90] established that the formation of these early co-clusters is completed in as little as 1 h in an Al - 0.59 wt.% Mg - 0.82 wt.% Si alloy, as no clustering peak was detected in samples naturally aged for more than 1 h. However, the expected negative effect was fully established after 10 - 18 min when only 60 to 80% of early co-clusters had formed. A second type of co-cluster forms at higher temperatures during DSC scans or longer natural ageing times depending on the

experimental set up. These later forming co-clusters also have a negative effect on artificial ageing by not acting as nucleation sites for the strengthening β" [90]. The volume fraction of clusters increases for up to about 5 - 10 days of natural ageing and remains stable for longer natural ageing times [89, 92, 93]. Their composition, as well as the composition of earlier co-clusters was found to be linked closely to the Mg/Si-ratio of the alloy, such that alloys with a low Mg/Si-ratio contain clusters with a Mg/Si-ratio close to 1 and alloys with high Mg/Si-ratios contain clusters with a Mg/Si-ratio close to 2 [81, 92].

The clustering kinetics were found to follow a n~ln(t) relationship rather than a n~√t relationship as seen in most diffusion controlled processes [44, 94]. This is attributed to the influence of vacancies on cluster formation and growth. As the vacancy concentration is significantly lower than the solute and the cluster concentration it is suggested that each vacancy is involved in the formation of several clusters transporting in excess of 1000 solute atoms [44, 90]. Due to solute vacancy interactions, vacancies get trapped in clusters [43, 44] and their release from clusters is the rate-limiting step for clustering. This might explain the observation of several stages during age hardening which can be distinguished by their hardening rate [95]. A first stage of fast hardening, where the hardening rate is determined by vacancy driven diffusion, is followed by a stage with a reduced hardening rate, which is dependent on the release of trapped vacancies from clusters.

The negative effect of natural ageing on the artificial ageing response, which is characterised by a reduced maximum hardness as well as a slower hardness increase, is explained by two concurrent effects. Firstly, solute is lost to clusters that are stable at the common artificial ageing temperatures between 150ºC and 200ºC [43], which also do not act as nucleation sites for the strengthening β" precipitates [22, 81, 85]. Secondly, vacancy trapping in clusters as described by Zurob and Seyedrezai [44, 46] not only limits the clustering rate, but more importantly reduces, together with vacancy annihilation, the number of vacancies available to transport solute during artificial ageing [43, 89].

2.5.2.2 Clustering in alloys with low Mg- and Si-contents (<1 wt.% Mg+Si)

Natural ageing and the thereby occurring cluster formation has been investigated less in alloys containing a low Mg- and Si-content. Information about the very early stages of clustering in alloys with low Mg+Si content can be drawn from PALS measurements [95-97]. Banhart et al. [95-97] found very similar positron lifetime developments for an alloy with a low Mg+Si content compared to an alloy with a high Mg+Si content. This was despite other measures like electrical resistivity, hardness and artificial ageing response showing significant differences. It remains therefore unclear whether the early stages of clustering occur in the same way as in alloys with a higher Mg+Si content or whether it is significantly different.

In contrast to alloys containing a higher Mg- and Si-content, alloys containing a low Mg- and Si-content, typically below 1 wt.% (Mg+Si), natural ageing affects the artificial ageing response positively (Figure 2-10) [89, 98]. To this day, it remains controversial as to the reason for the positive effect. After comparing a high Mg+Si AA6061 to a low Mg+Si AA6060 alloy, Pogatscher et al. [89] concluded that, as diffusion in the low Mg+Si alloy is always thermally activated, independent of its thermal history, clusters that dissolve slowly during artificial ageing are responsible for the increased hardness. However, as the overall amount of solute present during artificial ageing does not increase due to the dissolution of clusters, this explanation does not seem likely. Chang et al. [98] observed the formation of finer and more densely distributed β''-precipitates during artificial ageing after prolonged natural ageing by TEM and 3DAP. In addition fine precipitates were found to be richer in Mg compared to coarse, Si-rich β''-precipitates that formed in as-quenched and artificially aged samples. It is suggested that at least part of the clusters formed during natural ageing act as nucleation sites for β''-precipitation [98].

2.5.2.3 Influence of excess Si and Cu

As excess Si and Cu have been found to affect the precipitation sequence and increase strength and hardness, their influence on clustering has been investigated as well. Their influence on clustering, however, was found to be significantly different. While

excess Si was found to enhance the negative effect of natural ageing in alloys with a high Mg+Si content by increasing the number of clusters [99], additions of Cu seem to reduce the negative effect [85, 100].

The effect of Cu has been explained by Cu increasing the driving force for clustering [101] or by Cu affinity to forming Cu-vacancy clusters [85], which in both cases then leads to increased clustering kinetics at early stages of clustering. As this also leads to vacancies being trapped more quickly, and the second clustering reaction is slowed down. Therefore, less solute is lost and the negative effect of natural ageing on artificial ageing is reduced.

2.5.3 Precipitation of strengthening precipitates

In Al-Mg-Si alloys a high number density of fine β"-precipitates produces the highest hardness. These precipitates evolve from GP-zones, which form when clusters exceed a critical nucleus size. The strengthening potential of the precipitates strongly depends on their size and distribution. These are in turn dependent on alloy composition and processing parameters. Although low artificial ageing temperatures lead to higher strength [102], higher temperatures are preferred in industrial processing to minimise ageing times.

The alloy composition has a strong effect on the precipitation of strengthening precipitates. This extends not only for the strengthening phase forming elements Mg and Si but also to the contents of Cu, the transition metals Mn and Cr and Fe [103]. The latter form primary and secondary Si-containing phases and therefore reduce the amount of Si available to form strengthening precipitates.

The amount of Si, in particularly in relation to the Mg content is crucial for improved strength and hardness. For a long time the composition of β"-precipitates was assumed to be Mg_2Si, the same composition as the equilibrium phase. However, more recent studies have found the Mg/Si-ratio to be close to one and the composition has been reported as Mg_5Si_6 [9-11]. Their typical size was found to be $4 \times 4 \times 50$ nm^3 and their crystal structure has been determined to be monoclinic with the lattice

parameter a = 15.16 Å, b = 4.05 Å, c = 6.74 Å and β = 105.3º [9-11]. As a result modern alloys contain higher Si contents in relation to Mg to improve strengthening response [104]. The addition of excess Si also reduces the time to initiate strengthening in both the T4 and artificially aged temper, but lowers the stability of peak strength [105].

It is widely accepted that Cu improves the strengthening response of Al-Mg-Si alloys [2, 68, 103, 106]. The effect of Cu might be two-fold: although β" is the main hardening phase in Cu-containing Al-Mg-Si alloys [11], Cu has been found to be incorporated in the β"-precipitates [65, 107]. Furthermore, Cu-additions lead to a finer distribution of β"- precipitates after artificial ageing resulting in higher strength [65, 85, 106]. In contrast to the overaged stage discussed below, however, there were no additional strengthening phases found to precipitate in the presence of Cu at peak hardness.

2.5.4 Precipitates in the overaged stage

A lot of attention has been given to meta-stable phases forming in an overaged state. This is partly driven by completing the understanding of the precipitation sequence and partly by the characteristics of these phases. The crystal structure and composition, in particular the Mg/Si-ratio is strongly dependent on the alloy composition. In alloys with an Mg/Si-ratio balanced to the composition of the equilibrium Mg_2Si phase, β' is found. Although reports about the crystal structure of the β' phase agree on a hexagonal structure, the reported lattice parameters differ greatly. However, in recent years a ≈ 7.05 – 7.1 Å has been confirmed by different authors [10, 68, 72, 76]. In alloys with Si in excess of an Mg/Si-ratio of 1.73 by weight, additional phases referred to as Type A (U1), Type B (U2) and Type C (B') have been reported by Matsuda et al. [76] and Andersen, Marioara and co-workers (their designation in brackets) [66, 74, 75, 77]. The crystal structures and Mg/Si ratios are given in Table 2-3. Similarly, the addition of Cu affects the formation of meta-stable phases. Beside β' the Cu-containing Q' phase is found [65, 66].

Despite having different crystal structures these phases also differ in their Si and Mg content. Unsurprisingly, the β' phase shows a Mg/Si-ratio close to 1.73 in wt%,

whereas the meta-stable phases occurring in "Si-rich" alloys show much lower Mg/Si-ratios between 0.23 and 0.87 in wt%.

2.5.5 Microstructure after slow cooling

As mentioned previously, a significant amount of solute precipitates during slow cooling after extrusion. This leads to considerable changes in the microstructure. The following sections will outline which precipitation reactions occur during cooling and how this precipitation affects the microstructure of subsequent precipitation of strengthening phases.

2.5.5.1 Precipitation during cooling

There are at least two different precipitation reactions that occur depending on the cooling rate from solution treatment temperature [5, 49, 50, 108]. The first reaction occurs at higher temperatures (500-300ºC for AA6005A at a cooling rate close to equilibrium [49]) predominantly at slow cooling rates. With increasing cooling rates the reaction shifts to lower temperatures and its magnitude decreases. The critical cooling rate for this high temperature reaction is significantly lower than for the second reaction. The second reaction occurs between 300-200ºC at cooling rates close to equilibrium and between 360-260ºC at cooling rates above 10º/min in AA6005A [49]. The magnitude of this reaction increases with increasing cooling rates up to about 10ºC/min (for AA6005A) and then continually decreases until the critical cooling rate is reached. The temperature ranges and cooling rates at which the two reactions occur are strongly dependent on the alloy composition.

In alloys with moderate Mg and Si levels (AA6063 and AA6005A) the phase that precipitates during the high temperature reaction has been identified as the equilibrium β-Mg_2Si phase using EBSD and XRD [49, 108]. Precipitation occurs both on grain boundaries and within grains. Milkereit suggests primary intermetallics act as precipitation sites in both cases [49]. However, as the study was mainly carried out using SEM and optical microscopy, it is possible that the role of secondary dispersoids was overlooked. It is also noted that in alloys with higher Si-content a second phase,

most likely (Si), precipitates during the high temperature reaction in addition to β-Mg$_2$Si [49].

The low temperature reaction which is the predominant reaction at industrial cooling rates has been attributed to the precipitation of meta-stable, lath-shaped β'- or B'-Mg-Si phases on secondary dispersoids [5, 16, 23, 108]. Bomas et al. [23] analysed the lath-shaped particles in an alloy containing 1 wt% Si and 0.8 wt% Mg using TEM, SAD and EDX and found them to have a hexagonal crystal structure with a = b = 0.705 ± 0.005 nm and suggested c to be either c = 0.405 ± 0.001 nm [72] or c = 1.215 nm [109]. Their size depends strongly on the cooling rate and possibly on the alloy composition. Typical sizes for the lath-shaped precipitate have been reported to be 30 × 100 × 1000 nm^3 [23] and length decreasing from 600 nm to 300 nm with increasing cooling rates [49].

To this stage it remains unclear, whether there is a correlation between meta-stable phases forming in the overaged stage during age hardening and phases that form during cooling after solution treatment or extrusion. As the composition of meta-stable precipitates is strongly dependent on the alloy composition, the dependence of non-hardening precipitates on the alloy composition could have an effect on the remaining supersaturated solid solution.

2.5.5.2 Formation of precipitate-free-zones

To this point, there is little known about whether slow cooling affects the precipitation sequence of strengthening precipitates, but is it obvious that it affects their distribution. After natural and artificial ageing grain boundaries as well as the lath-shaped β'- or B'-precipitates are surrounded by a precipitate free zone (PFZ). PFZs can be the result of either solute loss or vacancy loss in the affected volume [27, 38]. However, since their size is the same on grain boundaries and around coarse intra-granular precipitates, where no vacancy annihilation occurs, it is more likely that solute loss is the main reason for their existence [38]. Deschamps et al. further concluded that the solute that forms the non-hardening precipitates comes from the immediate surrounding and the remaining material is unaffected [38].

As a result the mechanical properties strength and hardness should be able to be described by the composite effect of the material's microstructure consisting of strengthened, precipitate-containing matrix and soft PFZs using a composite model to [38]. Other material properties such as fracture toughness and corrosion are more sensitive to heterogeneities in the microstructure and therefore might not follow a simple composite rule [110].

2.6 Summary

The review of the literature focused on quench sensitivity and age-hardening in 6xxx series aluminium alloys and three key factors have been identified which provide the directions of the research undertaken in this thesis.

1. Quench sensitivity has mostly been attributed to solute loss on heterogeneous precipitation sites during cooling after extrusion or solution treatment at reduced rates. Despite the cooling rate, the following critical parameters have been identified: number density of dispersoids, which is determined by the transition metal content and homogenisation treatment, and the amount of Si and Mg.

2. The effect of the strengthening phase forming elements is less understood. It is quite possible that Mg, Si and Cu affect either the formation of the non-hardening precipitate or the age-hardening behaviour or both. The non-hardening precipitate has been related to the meta-stable phase forming during over-ageing, which is strongly dependent on the Mg/Si ratio and the presence of Cu. This might mean that compositional changes of the solid solution during cooling occur depending on the alloy composition and the precipitating phase. Furthermore, the Mg, Si and Cu content influences age-hardening in particular the early stages of natural ageing. As these early stages are also strongly influenced by the quench-rate dependent amount of mobile vacancies, it is to expect that there is a relation between quench rate, Mg, Si and Cu content and hardening behaviour.

3. Recent research into both natural and artificial ageing also highlights the role of mobile, non-equilibrium vacancies. Their concentration is undoubtedly dependent on the cooling rate and decreases during room temperature storage. It is therefore of great importance to link solute loss and vacancy concentration determined by the cooling rate to subsequent age-hardening.

Chapter 3   Experimental methods

3.1 Introduction

This chapter presents the materials and experimental techniques used in this study. Preliminary investigations to explain phenomenological findings by Sweet et al. [8] and to frame areas of future research were carried out on four widely used commercial 6xxx series extrusion alloys. The identified gaps were then investigated using the commercial alloy AA6060, as well as three laboratory alloys that varied in the content of the strengthening phase forming elements Mg, Si and Cu.

Quench sensitivity was quantified by measuring the difference in hardness of water quenched and air cooled samples of a fixed size. In an additional approach to quantify quench sensitivity, in particular solute loss, differential scanning calorimetry (DSC) was conducted. DSC was also employed to explore the role of quench rate on artificial ageing kinetics, by determining the activation energy of β"- and β'-precipitation of samples quenched at different rates. Microstructural information was gathered using scanning and transition electron microscopy. Positron annihilation lifetime spectroscopy (PALS) was carried out to obtain in-situ information about the evolution of quenched-in vacancies and the formation of clusters during natural ageing.

3.2 Alloys

Two groups of Al-Mg-Si alloys were investigated in this study: the four widely used commercial alloys AA6060, AA6005A, AA6061 and AA6082 as well as three model alloys with varying Mg and Si contents and Cu-addition within the alloy specification of AA6061 and additions of 0.35 wt.% Mn and 0.25 wt.% Fe in order to be able to investigate the influence of strengthening phase forming elements, whilst still being comparable to commercial alloys in terms of their content of primary intermetallics and secondary dispersoids.

3.2.1 Commercial alloys

The four commercial alloys AA6060, AA6005A, AA6061 and AA6082 (Table 3-1) had been direct chill (DC) cast into round billets homogenised for 2 h at 570ºC after heating

in a commercial muffle furnace that provided a heating rate below 200 K/h, the minimum heating rate identified to provide a homogeneous dispersoid distribution [31, 33]. Extrusion was carried out in an 880 ton direct extrusion press with a die temperature of approximately 450ºC, a billet temperature of 480 – 500ºC and an extrusion speed of 20 m/min to produce 6 mm × 40 mm solid sections (extrusion ratio 1:56) [8]. The extrusions were quenched in water and stretched with a strain of 0.5%.

Table 3-1 Composition of the commercial alloys used for preliminary investigations measured by inductively coupled plasma atomic emission spectroscopy (ICP-AES) by Spectrometer Services Ltd.

	Si	Fe	Cu	Mg	Mn	Cr
AA6060	0.43	0.18	-	0.45	0.04	-
AA6005A	0.73	0.18	0.12	0.53	0.10	0.06
AA6061	0.62	0.21	0.25	0.87	0.13	0.10
AA6082	1.05	0.15	0.05	0.75	0.60	0.08

A modified Jominy-type end quench test had been designed by Sweet et al. [8] to investigate the cooling rate dependent hardening response of extrusions (Figure 3-1). Details about the process can be found in [8]. The length of the extruded bars in the modified Jominy-type end quench test was chosen to be 600 mm in order to guarantee a broad range of cooling rates as well as to ensure that the sample holder did not influence the cooling rate at the end farthest from the quench. In preparation for the quench test AA6060 samples were solution treated for 1 h at 520ºC, whilst the medium to high strength alloys AA6005A, AA6061 and AA6082 were solution treated for 1 h at 550ºC. Then samples were fixed to a holder on one end while the other end was swung into a tank filled with water at room temperature. The temperature during cooling was measured by thermocouples embedded along the length of the bar. The cooling rate or average quench rate was determined by linear approximation of the slope between solution treatment temperature and 250ºC. The range was seen as the most critical temperature range for precipitation to occur.

Figure 3-1 Sample with embedded thermocouples in the quench rig designed by Sweet et al. [8].

3.2.2 Laboratory alloys

In order to investigate the effect of Mg, Si and Cu on quench sensitivity independent of dispersoid density, three model alloys were produced. Their respective composition is given in Table 3-2.

Table 3-2 Composition (in wt.%) of the model alloys investigated in Chapters 6&7 measured by inductively coupled plasma atomic emission spectroscopy (ICP-AES) by Spectrometer Services Ltd.

	Si	Mg	Mn	Fe	Cu	Al
Base Alloy (BA)	0.67	0.84	0.35	0.25	-	bal.
High Si (HS)	0.85	0.59	0.39	0.25	-	bal.
Base Alloy + Cu (BA+Cu)	0.69	0.82	0.34	0.29	0.22	bal.

In all three alloys the transition metal content was aimed to be constant at 0.25 wt.% Fe and 0.35 wt.% Mn. To accommodate for the Si that is tied up in intermetallic phases 0.022 wt.% Si is added for every 0.1 wt.% transition metal (Fe and Mn) in addition to Si added to form strengthening precipitates. The Base Alloy (BA) was designed with a Mg:Si-ratio of 1.73 (in wt.%) balanced to the equilibrium Mg_2Si-phase. The high Si alloy

HS contained the same overall amount of Mg and Si as alloy BA, but the Mg:Si-ratio was changed to 0.86 (in wt.%) or 1 (in at.%). The alloy BA + Cu was designed to have the same amount of alloying elements as alloy BA with an additional 0.22 wt.% Cu by reducing the Al-content.

Casting was conducted at the facilities of CSIRO Process Science and Engineering in Clayton, Australia. Ingots of the alloys were cast from commercially pure elements (Al, Mg and Si) or master alloys (Mn and Fe) with the addition of 0.005 wt.% TiB_2 from a Al-5Ti-B master alloy into pre-heated permanent steel moulds. The melt temperature was approximately 700ºC and the mould temperature 350ºC. In order to transform any unwanted primary β-AlFeSi intermetallics, dissolve primary β-Mg_2Si and precipitate a homogeneous distribution of secondary dispersoids samples were heated at 200 K/h to a homogenisation temperature of 570ºC and then held for 2 h in a muffle furnace.

3.3 Experimental Methods

There are two different studies presented in this work which had different intensions. In the initial study (Chapter 4) microstructural investigations using scanning and transmission electron microscopy (SEM and TEM), as well as thermal analysis of precipitation reactions using differential scanning calorimetry (DSC) were carried out in order to explain Sweet et al.'s [8] phenomenological findings of quench sensitivity in commercial alloys. This study revealed the need for investigations into the role of the cooling rate dependent kinetics of natural and artificial ageing.

In the second study (Chapters 5 – 7) the main focus is therefore on investigating the cooling rate dependent natural and artificial ageing response. Phenomenological results of the influence of cooling rate on age-hardening response during natural and artificial ageing are gained by measuring the hardness evolution during isothermal heat treatments. These results were then explained by microstructural investigations that allow deducting the influence of the microstructural features such as dispersoid density and thermal analysis using DSC, which in turn also allowed conclusions on the

ageing kinetics. In order to be able to obtain a measure for the concentration of vacancies, which is dependent on the cooling rate [37, 39, 48] and was found to have a major influence on ageing kinetics [22, 43], positron annihilation lifetime spectroscopy (PALS) is carried out in-situ during natural ageing using.

3.3.1 Heat treatment and hardness testing

In order to evaluate the effect of cooling rate on natural and artificial ageing response, homogenised samples of the model alloys and samples of AA6060 from the initial investigation of quench sensitivity in commercial alloys were solution treated, cooled at different rates and naturally and artificially aged for various times. The cooling rate and natural ageing time dependent hardness evolution offers one part of the explanation for different mechanisms contributing to quench sensitivity.

Samples for cooling rate dependent hardness measurements were approximately $6 \times 20 \times 20$ mm^3 for the commercial alloy AA6060 and $8 \times 20 \times 20$ mm^3 for the model alloys. Solution treatment was carried out in a salt bath for 1 h at 550ºC. The samples were hung from a steel wire and had a K-type thermo couple embedded close to the centre of the sample. The temperature during cooling was read with a data logger (data translation temperature and voltage USB DAQ module DT9805). Figure 3-2 shows a schematic of the samples with a central hole for embedding the thermo couple and a hole in the corner to attach a steel wire.
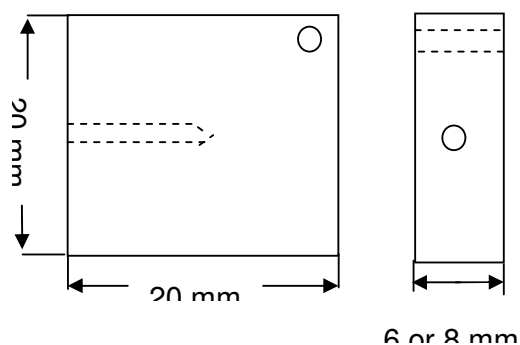
Figure 3-2 Schematic of the geometry of samples for hardening response measurements.

In order to investigate the effect of reduced cooling rate on age-hardening behaviour, water quenched, oil quenched and air cooled samples were compared in regards to

their hardening response during natural and artificial ageing. The cooling medium and the achieved cooling rate are summarised in Table 3-3.

Table 3-3 Cooling media and respective achieved rates for the three different cooling conditions.

Cooling method	Medium	Cooling rate
Water quenched	Water at room temperature (23ºC)	≈ 18,000 ± 500 K/min
Oil quenched	Silicon oil (Fuchs Australia, "Alloy Quench") at room temperature	≈ 2000 ± 150 K/min
Air cooled	on alumina bed in still air at room temperature	≈ 50 ± 5 K/min

Figure 3-3 shows typical cooling curves recorded during the cooling of the model alloys. The heating rate (Table 3-3) was determined by linearly approximating the measured decrease in temperature between the solution treatment temperature and 250ºC. It is in this temperature range that precipitation during cooling in known to be most prominent [e.g. 9-11].
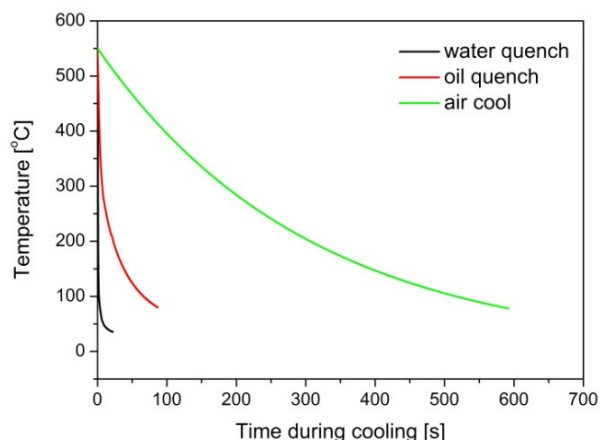
Figure 3-3 Representative cooling curves for water quenched, oil quenched and air cooled samples.

The subsequent artificial ageing was conducted after 2 min, 30 min and 24 h natural ageing. Two minutes was chosen because it was the minimum time it took to clean and dry air cooled and oil quenched samples after solution treatment. Thirty minutes represents the minimum natural ageing time during industrial processing and 24 h is an overly long natural ageing time in an industrial context but was one that was used in the initial experiments on commercial alloys.

Artificial ageing was carried out in a silicon oil bath at 190ºC for AA6060 and at 175ºC for the model alloys. These temperatures were chosen according to typical age-hardening treatments in industry where soft alloys (like AA6060) are treated at higher temperatures for shorter times compared to medium to hard alloys, which the model alloys are similar to in composition. Vickers hardness was measured using a load of 0.3 kg for naturally aged samples and 0.5 kg for artificially aged samples.

3.3.2 Determining quench sensitivity

In contrast to previous studies in the literature that aimed to identify minimum cooling rates to avoid solute loss [49] or the loss of properties [8, 21, 55, 58] or characterise an alloy by determining its quench sensitivity [24], the aim of this study is to investigate the different physical processes that describe quench sensitivity. The chosen experimental set up therefore does not aim to develop or use a measure for quench sensitivity that allows a single straight-forward description or characterisation of an

alloy like a quench factor [55, 63] or half-life time $\tau_{1/2}$ [4]. In order to be able to differentiate and compare the physical processes that cause quench sensitivity, the difference in hardness between an air cooled (AC) (50 K/min) and a water quenched (WQ) (18,000 K/min) sample after the same natural and artificial ageing time is used as the measure for quench sensitivity.

$$QS = HV_{WQ} - HV_{AC} \qquad \text{3-1}$$

The monitoring of the cooling rate dependent absolute hardness values for various natural and artificial ageing times allows conclusions on the different physical processes and their magnitude occurring as a result of the cooling rate. The comparison of air cooled samples against water quenched samples allows separating the effects of solute loss and vacancy concentration.

$$QS = f(solute\ loss) + f(vacancy\ concentration) \qquad \text{3-2}$$

3.3.3 Differential scanning calorimetry

Differential scanning calorimetry (DSC) has been used extensively in literature to analyse aluminium alloys mainly for quantitative analysis of precipitation, dissolution and recrystallisation reactions and their kinetics [111-114]. In the present study, DSC has been employed to characterise precipitation reactions at two different stages of the process. Firstly, precipitation reactions during cooling after solution treatment were investigated after a simulated solution treatment cycle and secondly, precipitation reactions during artificial ageing after cooling at different rates (water quench vs. air cooled) and different natural ageing times (30 min or 24 h) were investigated during linear heating experiments. This allowed gathering quantitative information on the amount of precipitates forming, as well as determining the precipitation kinetics.

3.3.3.1 Experimental method

Samples for DSC investigations were 2 mm thick discs with a diameter of 5 mm. They were cut rods that had been homogenised (model alloys) or completely processed and peak aged (commercial alloys).

All DSC runs were conducted in a PerkinElmer DSC 7. The equipment was calibrated using In and Zn standards. The baseline was measured before the first run of each testing condition and then after every third run. Therefore, the heat release between to empty Al-pans was measured during the same thermal cycle as the samples. The baseline measured in this way is subtracted automatically during data acquisition by the software to minimise external influences and baseline drift. Analysis and fitting of the resulted curves was done using PeakFit software. Overlaying peaks were fitted and separated using Gaussian shaped peaks.

3.3.3.2 Determining the magnitude of precipitation reactions

For determining the magnitude of precipitation reactions during cooling, samples underwent a simulated solution treatment cycle consisting of heating to 550ºC, holding for 1 h and cooling at a specified rate. Cooling rates between 5 K/min and 150 K/min were investigated. This not only allowed estimating minimum cooling rates necessary to avoid precipitation, but also allowed determining the cooling rate dependent magnitude of the precipitation reactions during cooling. Assuming the same phase (β') precipitates in all alloys, the peak area is proportional to the amount of β'-phase forming during cooling. Integrating over the peak gives the enthalpy for the formation of β'-phases (ΔH). This can be used to compare solute loss in the different alloys and for changing cooling rates. These results were compared to hardness response measurements and microstructure. In order to determine the effect of solute loss on loss of properties, hardness values were measured for the investigated cooling rates after 24 h natural ageing and 8 h artificial ageing at 175ºC (6 h at 190ºC for AA6060).

Apart from precipitation reactions during cooling after solution treatment, the formation of clusters and the precipitation of strengthening phases were investigated during continuous heating experiments. Therefore, water quenched and air cooled samples were naturally aged at room temperature for either 30 min or 24 h and heated at 10 K/min, 20 K/min, 30 K/min and 50 K/min. From these measurements qualitative information about suppressed reactions could be gained. The magnitude of

the reactions, characterised by the formation enthalpy ΔH, was compared for the various cooling and natural ageing conditions and related to hardness measurements.

3.3.3.3 Determining precipitation kinetics using DSC

The influence of cooling rate and natural ageing time on the artificial ageing response is further characterised by precipitation kinetics. The activation energies of water quenched and air cooled samples of alloy BA are therefore determined from linear heating experiments at 10 K/min, 20 K/min, 30 K/min and 50 K/min. The Type B-1.95 Peak method described by Starink [115] was used as it allows the use of the peak temperatures (T_p) instead of the temperature at which a fixed amount is transformed, which is difficult to determine in the present set up due to overlapping peaks (Figure 3-4). It still offers high accuracy compared to isoconversion methods.
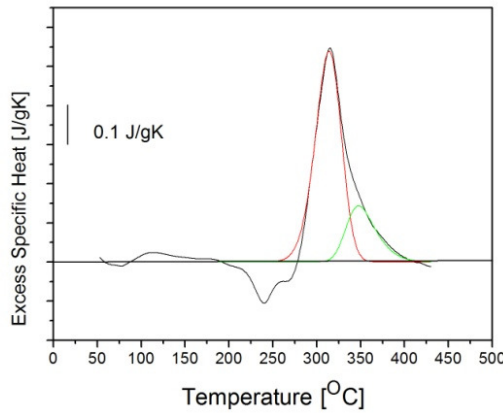
Figure 3-4 Example of a DSC curve of a WQ sample after 24 h natural ageing during heating at 20 K/min. The peaks for β''-precipitation (red) and for the β''- to β'-transformation are overlapping.

The activation energy (E_a) is determined from the following relationship:

$$\ln\left(\frac{\beta}{T_p^{1.95}}\right) = -\frac{E_a}{RT_p} + C \qquad\qquad 3\text{-}3$$

T_p is the peak temperature, β is the heating rate, R the gas constant (8.314 JK^{-1}mol^{-1}). The determined activation energy allows for conclusions on the dominant precipitation mechanism. If the determined activation is close to the activation energy for diffusion

at equilibrium vacancy concentration of the rate determining precipitating element Mg, Si or Cu (120-135 kJ/mol) the precipitation reactions are thermally activated. If the determined activation energy is significantly lower (55-70 kJ/mol) the diffusion of vacancies determines precipitation kinetics [112].

3.3.4 Microscopy

3.3.4.1 Scanning electron microscopy

Scanning electron microscopy was employed to investigate the microstructure, in particular the distribution of secondary dispersoids after homogenisation. Samples for scanning electron microscopy were ground and polished using 500, 1200 and 2400 grit SiC-paper and a colloidal silica suspension, respectively. Investigations were carried out using a JEOL JSM-7001F field emission scanning electron microscope (FEG-SEM) equipped with a retractable back scattered electron (BSE) detector and a Bruker EDX system.

The distribution of secondary dispersoids was determined from at least ten BSE micrographs per sample acquired at 10000 times magnification and using a high contrast setting at random locations. From each original SEM BSE image (Figure 3-5a) the bar with image information was removed and the imaged subsequently inverted and a threshold was applied (Figure 3-5b). As the contrast and brightness of each SEM image varied the threshold was chosen to minimise noise and maximise information from the sample. The number and size of the dispersoids was determined from modified images (e.g. Figure 3-5b) using Adobe Photoshop Extended CS4 Win EULA software.
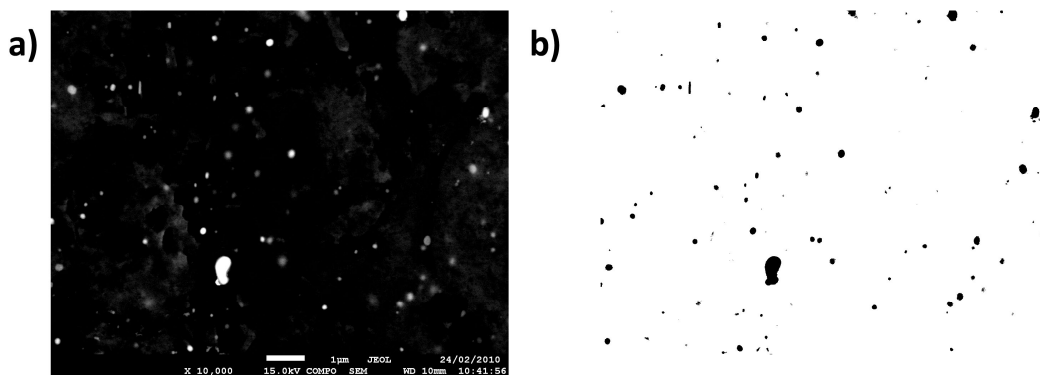
Figure 3-5 Examples of a) an original back scattered electron image taken using the JEOL JSM-7001F with high contrast and b) the modified version of the same image from which the dispersoid density was determined.

3.3.4.2 Transmission electron microscopy

Transmission electron microscopy was employed to investigate the size and crystal structure of non-hardening precipitates as well as the size of the precipitate free zone surrounding the non-hardening precipitates. Furthermore, the size and number density of strengthening precipitates were compared using TEM micrographs. Standard bright field imaging, chemical analyses and selected area diffraction (SAD) were performed on the conventional PHILIPS CM20 TEM operating at 200kV and equipped with an Oxford Systems EDX detector. High resolution images were obtained from a FEI TECHNAI F20 FEG-TEM. Fast Fourier transforms (FFTs) of the high resolution images were used to determine the lattice spacing of the non-hardening precipitates since diffraction patterns were too difficult to obtain from the cross-section of the non-hardening precipitates.

The TEM foils were prepared by punching discs with a diameter of 3 mm from a 500 μm thick slice of the heat treated and aged material. These discs were ground on 2400 grit SiC-paper to a thickness of approximately 100 μm. Alloys that had been deformed previously, i.e. the commercial alloys were thinned by jet electro polishing at -30ºC and with an applied voltage of 13 V using a 67 % methanol, 33% nitric acid electrolyte. Due to preferential etching of coarse primary AlFeMnSi-intermatallics, specimens of the model alloys were thinned by ion milling using a Gatan 691 Precicion Ion Polishing System (PIPS).

In order to analyse the acquired selected area diffraction patterns (SADs) and fast Fourier transformations (FFT) diffraction patterns were simulated using the web-based software package WebEMAPS [116].

3.3.5 Positron annihilation lifetime spectroscopy (PALS)

PALS is well suited for the investigation of open-volume defects, such as vacancies [96, 117-120]. The average positron lifetime measured during PALS is sensitive to open volume defects as the time to annihilation is dependent on the electron density [121]. A low electron density results in a longer positron lifetime. Therefore the positron lifetime in a mono-vacancy in aluminium (240-250 ps [96, 118]) is higher than in defect-free homogeneous (bulk) aluminium (162 - 168 ps). The electron density in the proximity of solute atoms is also different from the electron density of bulk aluminium. Table 3-4 summarises the average positron lifetimes in the bulk, defect free metals, in monovacancies in the respective metals and the changes in the average lifetime relative to the average lifetime of a vacancy pair with an Al atom in an Al matrix (τ_{VAl}) when a vacancy is paired with a solute atom. The lower electron density of Mg and Si results in clusters having a higher lifetime than bulk aluminium so that clustering reactions can be detected [118]. Therefore, PALS is ideal to study the natural ageing behaviour as measurements can be made in-situ [42, 118, 122]. Detailed information on PALS and its application in light metals research is given in [118, 121, 123].

Table 3-4 Summary of average positron lifetimes in bulk material and vacancies in different configurations.

	Bulk	Mono-vacancy in metal	Solute-vacancy pair in Al-matrix
Aluminium	162 - 168 ps [121, 124]	240 - 250 ps [96, 118]	-
Magnesium	220 ps [118]	244 - 250 ps [118, 125]	τVAl + 1 ps to τVAl + 3 ps [96]
Silicon	222 ps [118]	~ 255 ps [126]	τVAl - 1 ps to τVAl - 2 ps [96]

Positrons generated by a β⁺-decay of a radioactive Na-22 source under the emission of 1280 keV, migrate through the lattice over a mean distance of 100 nm and annihilate with an electron under the emission of two 511 keV γ-rays. The time differences between the emission of the 1280 keV γ-ray and the 511 keV γ-ray are measured from the positron lifetime spectrum.
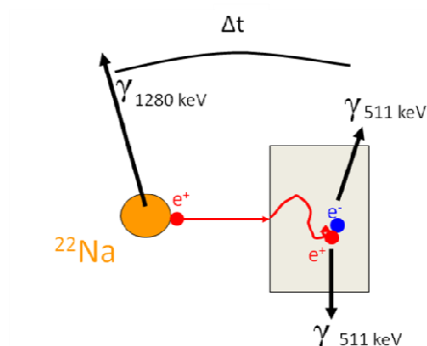
Figure 3-6 Schematic according to Dlubek [118] showing the positron generation in a β+-decay of 22Na under emission of a 1280 keV γ-ray and positron annihilation in sample material under the emission of two 511 keV γ-rays. The time difference between the emission of 1280 keV γ-ray and a 511 γ-ray is recorded and the average positron lifetime τ_{AV}.

Thin plates (13 × 13 × 1 mm^3) were used for PALS investigation. The samples were solution treated in pairs in a ceramic crucible in a vertical tube furnace under 50 l/h Ar flow at 550 ºC for 1 h and quenched either in iced water, silicone oil or in still air on an alumina bed. This produced similar cooling rates to those experienced by samples used for hardness measurements.

An ORTEC fast-fast coincidence system was used to measure positron lifetimes. Samples typically took 1 minute to stabilize at the set temperature of 20 ±1ºC after insertion into the system and this temperature was maintained for all measurements. Plastic scintillators were used and an average prompt function full width at half maximum (FWHM) of 244 ps was obtained from a time per channel of 50.2 ps. A Na-22 (≈60 µCi) positron source sandwiched within 2.5 µm thick Ti foil was used for measurements. The source-sandwich configuration allowed spectra to be obtained every 2 min with at least 6×10^4 total counts. Such a small time window was not required at later ageing times, up to 1×10^7 counts were summed for better statistics for later data points and corrected for channel drift by shifting peaks to a default

channel. Source correction was determined using a well-annealed slow-cooled pure Al sample (99.999 %); a 2.4 % source contribution of 529 ps was accounted for in the analysis. Lifetime spectra were analysed using the program *LT* [127] and they were found to fit for a single positron lifetime component reported as the mean lifetime, τ_{AV}. Consistent two lifetime fits could not be obtained suggesting either a single dominant lifetime, multiple lifetimes too close to be reliably distinguished, or a combination of both.

3.4 Summary

Table 3-5 summarises the techniques used in the respective Chapters of the present work.

Table 3-5 Summary of the used techniques and their application in the results chapters (Chapter 4 to 7).

	Chapter 4	Chapter 5	Chapter 6	Chapter 7
Hardness measurements	determining quench rate dependent hardness determining quench sensitivity	hardening response after various cooling rates and natural ageing times determining quench sensitivity	hardening response after various cooling rates and natural ageing times determining quench sensitivity	hardening response after various cooling rates and natural ageing times determining quench sensitivity
Differential scanning calorimetric (DSC)	quantifying solute loss during cooling from solution treatment	monitoring precipitation reactions of strengthening phases	quantifying cooling rate dependent solute loss during cooling from solution treatment monitoring precipitation reactions of strengthening phases determining activation energies for precipitation reactions	quantifying solute loss during cooling from solution treatment
Scanning electron microscope (SEM)	determining dispersoid density and size distribution	imaging of homogenised microstructure	determining dispersoid density imaging of homogenised microstructure	determining dispersoid density
Transmission electron microscope (TEM)	determining crystal structures of dispersoids and non-hardening precipitates, imaging	imaging precipitate distributions	imaging precipitate distributions determining the crystal structure of non-hardening precipitates	determining the crystal structure of non-hardening precipitates
Positron annihilation lifetime spectroscopy (PALS)		average lifetime evolution during natural ageing in pure Al and AA6060	average lifetime evolution during natural ageing of the model alloy BA	

Chapter 4   Quench Sensitivity in Commercial Alloys

4.1 Introduction

In this chapter quench sensitivity in four commercial 6xxx series alloys, namely AA6060, AA6005A, AA6061 and AA6082 is investigated. This follows work by Sweet et al. [8] which has mapped the effect of varying cooling rates on the hardening response of these commercial 6xxx series extrusion alloys. The focus here is on identifying the influence of the two processing steps homogenisation and cooling after solution treatment on the microstructure of the material using electron microscopy and differential scanning calorimetry. The influence of alloy composition on dispersoid density and quench sensitivity is investigated by comparing AA6060, AA6005A, AA6061 and AA6082. These alloys have distinctly different contents of the dispersoid forming elements Mn and Cr as well as the strengthening phase forming elements Mg, Si and Cu. The influence of homogenisation time and temperature on dispersoid density and quench sensitivity in the medium to high strength alloy AA6082 is also investigated. Although neither the influence of dispersoids nor of the Mg, Si and Cu content can be fully understood from this investigation, the results highlight gaps in the current knowledge and provide the foundation for the research in the following chapters.

4.2 Investigation of commercial alloys

The results of the modified Jominy-type end quench test conducted by Sweet et al. [8] are explained by microstructural observations, in particular the number density of dispersoids and thermal analysis of precipitation reactions during cooling after solution treatment using DSC.

4.2.1 Hardening Response

The cooling rate dependent age-hardening response after 24 h natural ageing and 8 h artificial ageing was measured for the commercial alloys AA6060, AA6005A, AA6061 and AA6082. Their composition is listed in Table 1 in Chapter 3.A modified Jominy-type end quench test was conducted, which consisted of 6 mm × 40 mm × 600 mm extruded bars quenched at one end by being swung into a tank filled with cold water

(Section 3.2.1.) [8]. The hardness measured along the extruded and aged bars is related to the quench rate in Figure 4-1[8]. After fast quenching(~600 K/min) the difference between the soft alloy AA6060 and the medium to high strength alloys is significant, whereas in the slow cooled end (~50 K/min) this difference is reduced up to the point that AA6082 shows lower hardness than the alloy AA6060. The hardness of AA6060 is almost independent of the cooling rate while the hardness of the other investigated alloys, especially AA6082, is highly dependent on the cooling rate.
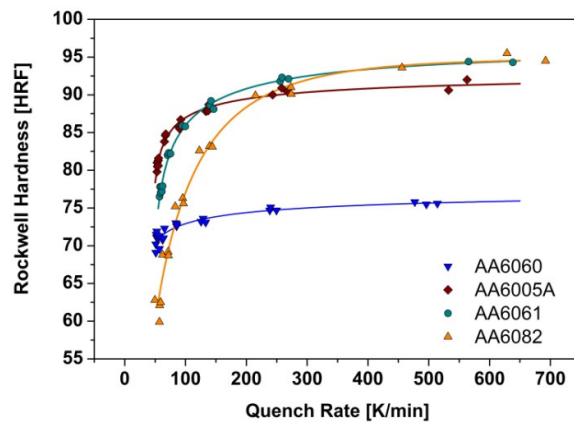
Figure 4-1 Hardness versus quench rate of the investigated 6xxx series alloys after quenching in a modified Jominy-type quench rig [8].

In order to be able to compare the quench sensitivity with other alloy features, quench sensitivity is defined as the difference in the measured hardness between water quenched (here maximum cooling rate is approximately 700 K/min) and air cooled samples (here minimum cooling rate is approximately 50 K/min).

4.2.2 Thermal analysis

Differential scanning calorimetry was used to simulate a solution treatment cycle with a cooling rate of 50 K/min, which is close to the minimum cooling rate in the above described modified Jominy-type quench end test and a typical cooling rate achieved by a forced air quench during industrial processing. This allowed investigating the alloy composition dependent amount of solute lost during cooling, which is, assuming the same phase (β') is precipitating in all investigated alloys, proportional to the peak area, i.e. the formation enthalpy ΔH.

Figure 4-2 shows that no peak was observed in AA6060, whereas alloys AA6005A, AA6061 and AA6082 had significant peaks indicating precipitation of the non-hardening Mg-Si phases. The size of the peaks, reflected in the enthalpy of precipitation (Table 4-1), indicates more precipitation occurring in AA6082 than in AA6061 and AA6005A. While the peak of AA6005A is uniform, both AA6061 and AA6082 show a shoulder during the early stages of precipitation.
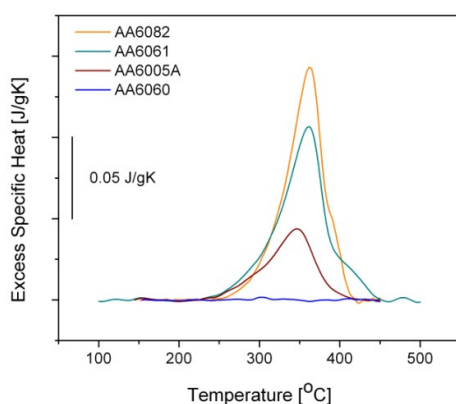
Figure 4-2 DSC scans, taken at a scan rate of 50 K/min during cooling after an imitated solution treatment.

Table 4-1 Quench sensitivity and enthalpy of precipitation of the investigated alloys.

Alloy	Quench Sensitivity [HRF]	Enthalpy of β'-Precipitation [J/g]	Enthalpy of β-Precipitation [J/g]
AA6060	6.7	0	0
AA6005A	12.2	2.6 ± 0.4	0.16 ± 0.01
AA6061	17.8	6.8 ± 0.4	1.5 ± 0.1
AA6082	32.7	7.8 ± 0.2	1.3 ± 0.1

4.2.3 Microstructure characterisation

The dispersoid density was determined from back scattered SEM micrographs (Figure 4-3). As dispersoid phases contain significantly heavier elements than the aluminium matrix, they give a bright contrast in the back-scattered electron mode. The microstructure, in particular the dispersoid density, of the four investigated

commercial alloys, AA6060, AA6005A, AA6061 and AA6082 differs considerably with AA6082 showing a considerably higher dispersoid density than AA6005A and AA6061.

Figure 4-3 shows bright, dispersoid phases in the different commercial alloys. It can be seen, that after the same homogenisation treatment 2 h at 570ºC dispersoids in all four alloys are very similar in size, approximately 150 nm ± 100 nm. The varying Mn- and/or Cr-content mainly affect the number density of dispersoids (Figure 4-4).
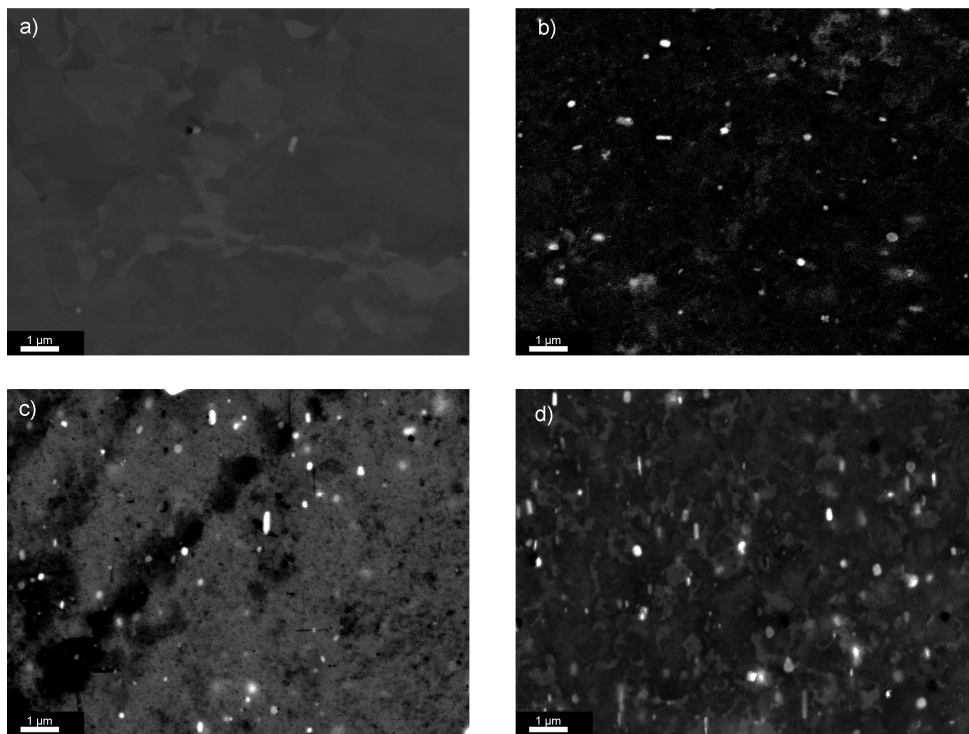
Figure 4-3 Dispersoid distribution after homogenisation for 2 h at 570ºC and extrusion in a) AA6060, b) AA6005A, c) AA6061 and d) AA6082.
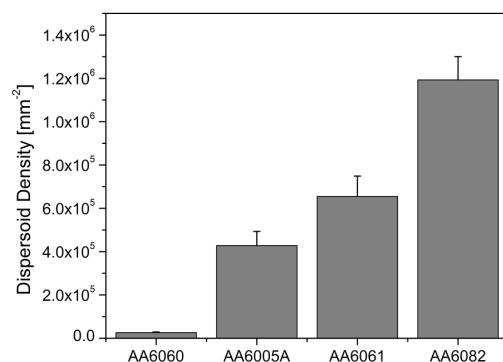
Figure 4-4 Number density of dispersoids in the investigated, commercial 6xxx series alloys. The dispersoid number density in AA6060 is negligible compared to the other alloys.

4.2.4 Discussion

The relationship between quench sensitivity and dispersoid density is shown in Figure 4-5. It has been determined experimentally by measuring some of the samples using both HRF- and HV-methods. In order to compare these results to the following hardness results, HRF-values were converted to HV using:

$$HV = 0.76HRF + 41 \qquad 4\text{-}1$$

There is a relationship between dispersoid density and quench sensitivity suggesting that dispersoid density has the dominant effect on quench sensitivity in this range of alloys.

The relationship between quench sensitivity and dispersoid density suggests that there remains a certain quench sensitivity even if the material was free of secondary dispersoids. Solute loss to grain boundaries [6] or differences in precipitation kinetics as a result of a higher concentration of non-equilibrium vacancies driving clustering and/or precipitation in water quenched samples.
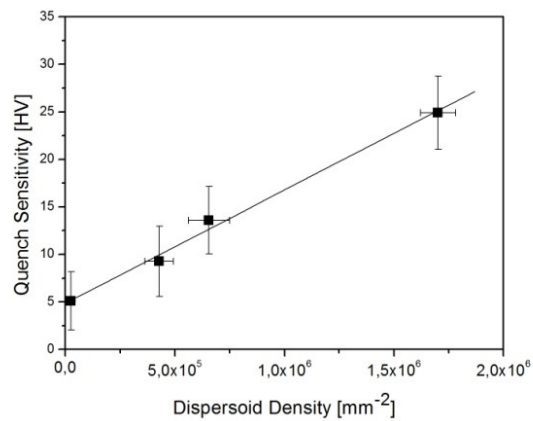
Figure 4-5 Relationship between quench sensitivity and dispersoid density in commercial alloys after 24 h natural ageing and 6 h artificial ageing at 190ºC for AA6060 and 8 h artificial ageing at 175ºC for AA6005A, AA6061 and AA6082.

The results for alloy AA6060 support the hypothesis of the influence of difference in precipitation kinetics on quench sensitivity. Although it appears to be following the linear relationship between quench sensitivity and dispersoid density, there was no precipitation recorded during cooling using DSC (Figure 4-2). Therefore it should be investigated whether clustering and precipitation kinetics are being influenced and whether there is a difference in hardness evolution depending on the cooling rate.

At this stage it should be remembered that medium to high strength 6xxx series alloys not only experience loss of properties due to solute loss during slow cooling after solution treatment, but also as a result of natural ageing (Section 2.5.2.1). The negative effect has been predominantly attributed to the loss of solute to stable clusters that do not act as precipitation sites for strengthening precipitates [90, 128, 129] and the difference in vacancy supersaturation between immediately after quenching and prolonged natural ageing [43, 85].In the present experimental set-up samples experienced 24 h natural ageing, such that the influence of the difference in the concentration of quenched-in vacancies as a result of cooling rate is strongly reduced [37]. Although there are potential differences in the clustering rate such that the negative effect of natural ageing is quench rate dependent, the quench sensitivity measured here is predominantly the result of solute loss.

Under the condition that the same phases precipitate during cooling and driving force and precipitation kinetics for strengthening phases are independent of cooling rate and alloy composition, the formation enthalpy ΔH of the phase transformation provides an alternative measure for quench sensitivity.

Figure 4-6 compares the formation enthalpy ΔH determined from DSC scans to quench sensitivity in AA6005A, AA6061 and AA6082. The results are plotted in a way such that quench sensitivity relates to the enthalpy of the formation of non-hardening precipitates in AA6005A and AA6082. However, AA6061 seems to diverge from this trend, showing a higher enthalpy of precipitation relative to AA6082 and AA6005A for its quench sensitivity.
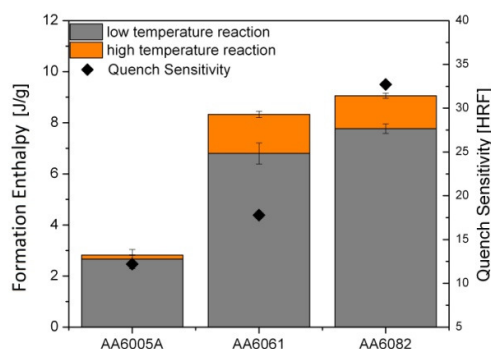
Figure 4-6 Quench Sensitivity in relation to specific precipitation heat during cooling at 50 K/min shows comparably high formation enthalpy in AA6061.

The DSC measurements, including the determination of the baseline, which was carried out using empty pans, have been conducted in the same manner for all samples. As a consequence, the high heat release during cooling in relation the quench sensitivity in AA6061 suggests that either or both of the assumptions – that the precipitating phases have the same composition and crystal structure in all alloys and that solute loss affects subsequent age hardening in the same way in all alloys – are not fulfilled.

Figure 4-7a shows a micrograph of an air-cooled AA6061 sample. Lath-shaped, non-hardening precipitates have formed on dispersoids and are surrounded by a

precipitate-free zone. Finely distributed strengthening precipitates are found in the matrix between the PFZs. The EDX spectrum of the non-hardening precipitate in AA6061 (Figure 4-7c) indicates that it contains Cu in addition to Mg, Si and Al, which are present in the non-hardening precipitate in AA6082[23]. According to Ravi and Wolverton [69] the formation enthalpies for the Cu-containing Q-phase is generally higher than the for Cu-free β'- or B'-phases. This might explain the relatively high formation enthalpy ΔH measured for AA6061 compared to the Cu-free alloys AA6005A and AA6082.
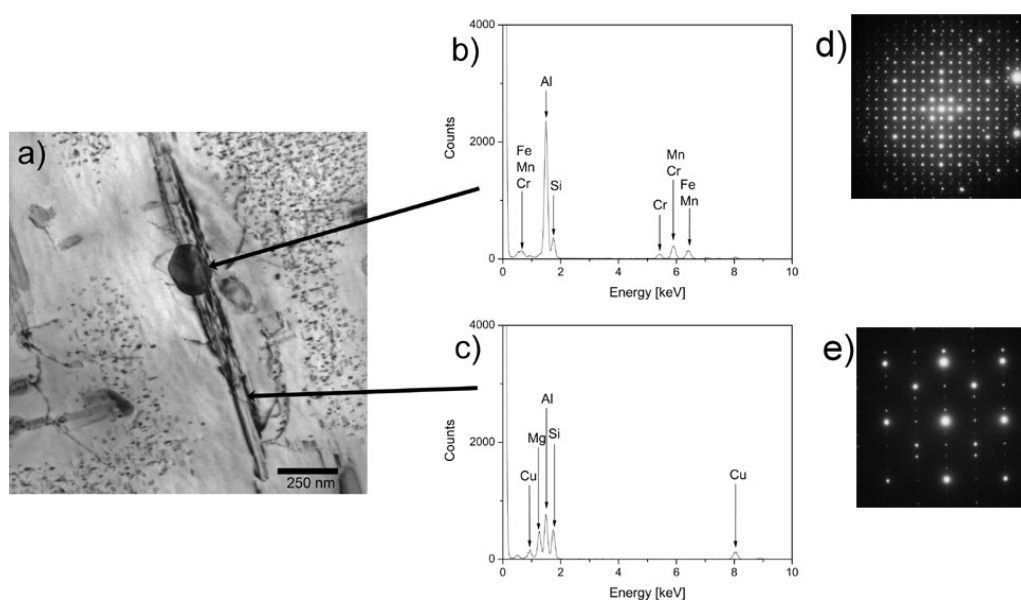
Figure 4-7 (a) TEM micrograph (along [001]$_{Al}$) showing dispersoids with an attached, lath-shaped non-hardening precipitated in AA6061 after cooling in still air at about 50 K/min. EDX spectra indicate the composition of the dispersoid (b) and the non-hardening precipitate (c). The SAD pattern of the dispersoids indicates its simple cubic structure (d). A SAD pattern of the matrix and the non-hardening precipitate along [010]$_{ppt}$//[001]$_{Al}$ (e).

The current results also fail to clarify the influence of a changing solute concentration. As described in Chapter 2 Figure 6, in a typical 6xxx series alloys the amount of the strengthening phase forming elements Mg and Si increases with the amount of dispersoid forming elements Mn and Cr. Therefore section 4.3 discusses the influence of dispersoid density with nearly constant solute content. As the same alloy is investigated after three different homogenisation treatments, differences in the solute

content arise only from differences in the solute tied up in intermetallics and dispersoids.

4.3 Quench sensitivity in AA6082 with different dispersoid densities

4.3.1 Hardness measurements

The hardness of a AA6082-type alloy was measured after samples had been homogenised for 2 h at 510ºC, for 2 h at 570ºC and for 12 h at 570ºC, solution-treated at 550ºC for 1 h and water quenched or air cooled. Figure 4-8 shows the hardness values of water quenched and air cooled samples depending on the homogenisation condition after 24 h natural ageing and 8 h artificial ageing at 175ºC. Slight differences in the hardness of the water quenched samples might be the result of different amounts of strengthening phase forming elements – in particular Si – tied up in primary intermetallics and secondary dispersoids. However, it becomes obvious that increasing homogenisation time and temperature leads to decreasing differences in the hardness between water quenched and air cooled samples.
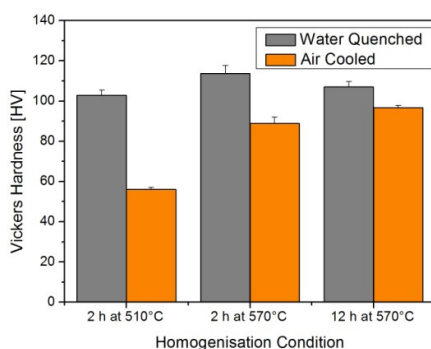
Figure 4-8 Hardness measurements after solution-treatment and water quench or air cooling show that quench sensitivity, i.e. the difference in hardness is greatest in samples homogenised for short times at low temperatures.

4.3.2 Microstructure characterisation

These findings can be explained by the decrease in dispersoid density with increasing homogenisation time and temperature.

Increasing the homogenisation temperature and time leads to a reduction in the dispersoid number density and an increase in dispersoid size (Figure 4-10). For the alloy homogenised at the lowest temperature and shortest time (510°C and 2 hours), most of the dispersoids are smaller than 100 nm (Figure 4-10 a). Increasing the temperature to 570°C and the time to 12 hours leads to a decrease in the number of small dispersoids (< 100 nm) with most dispersoids being in the size range 200 to 400 nm.
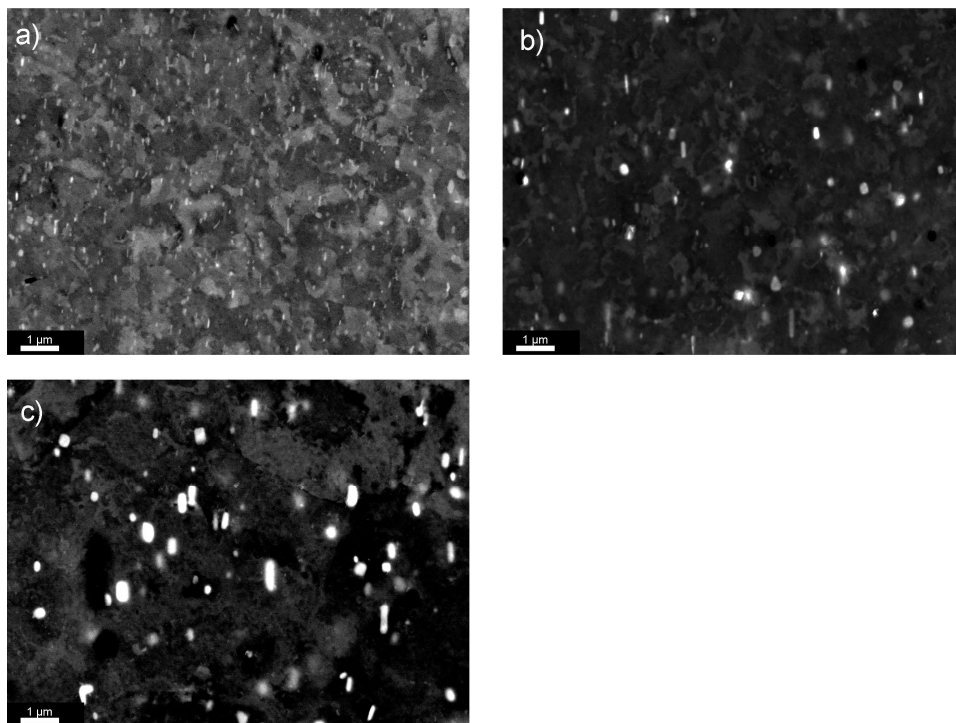
Figure 4-9: High contrast back scattered electron micrographs of different dispersoid sizes and densities in AA6082 after changed homogenisation conditions; (a) 2 h at 510ºC, (b) 2 h at 570ºC and (c) 12h at 570ºC.
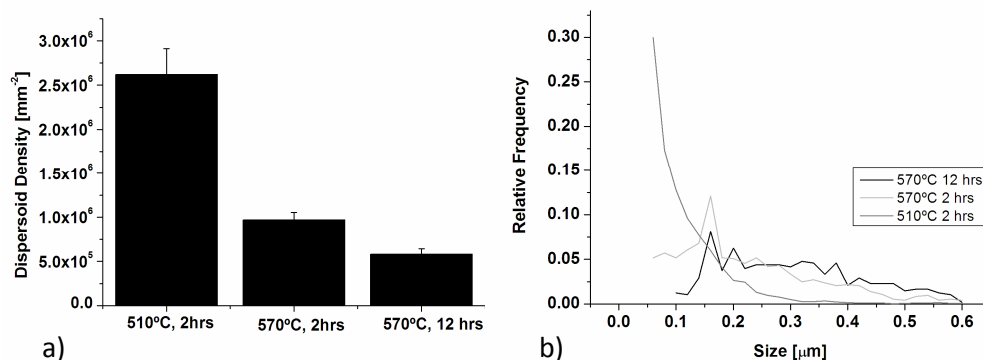
Figure 4-10: Dispersoid density (a) and size distribution (b) in AA6082 after different homogenisation treatment.

From the results (Figure 4-10) it can be seen that homogenisation time and temperature determine dispersoid size and number density. However, it should be kept in mind that during industrial processing these parameters are chosen to guarantee transformation and/or dissolution of primary intermetallics rather than optimising dispersoid distribution.

Figure 4-11 shows a TEM micrograph of AA6082, homogenised for 2hrs at 570ºC. Dispersoids of different crystal structures and sizes are present in this sample. These particles appear to be the same as those reported by Yoo et al [7]. The first selected area diffraction (SAD) pattern (Figure 4-11b) shows the body centred cubic (bcc) structure of a large particle and hence indicates its composition to be $Al_{12}(MnFe)_3Si$ and the EDS spectrum (Figure 4-11d) indicates the Mn:Fe-ratio is about 1. The second SAD pattern (Figure 4-11c) shows the simple cubic (sc) structure of dispersoids of about 200 nm and indicates that it is $Al_{15}(MnFe)_3Si_2$ based on the α-$Al_{15}Mn_3Si_2$ phase. The EDS spectrum of this dispersoid (Figure 4-11e) shows a pronounced Mn K_α peak at 5.9 keV next to a small Fe K_α peak at 6.4 keV and a much greater Mn:Fe ratio when compared to the large particle, with an average of 7.9 over 5 particles.

Although there appears to be a phase transition from the simple cubic α-$Al_{15}Mn_3Si_2$-type phase to the body-centred cubic α-$Al_{12}Fe_3Si$-type phase, the lattice spacing $a = 1.26$ nm is the same for both phases. Hence, the effect of these phases as precipitation sites is very similar.
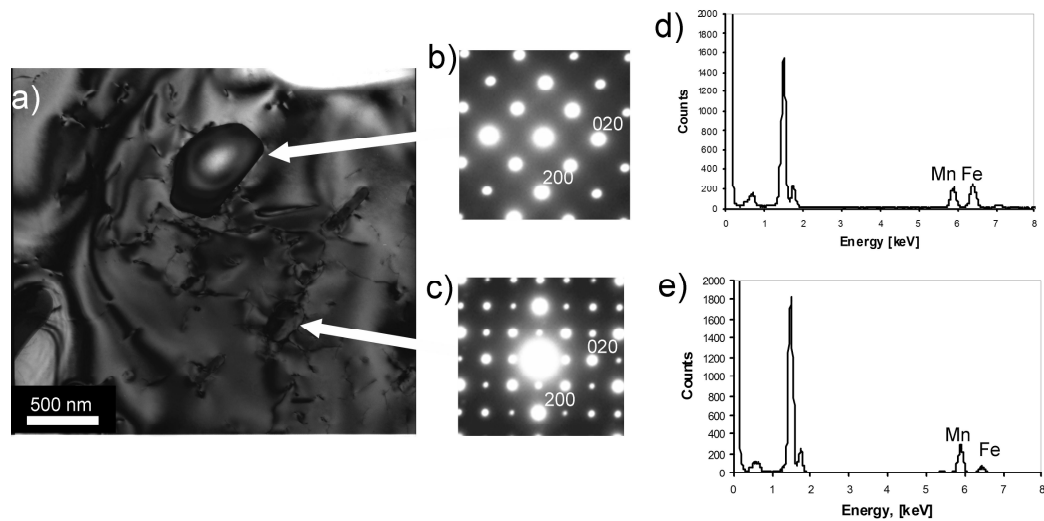
Figure 4-11 TEM image of dispersoid phases in AA6082 homogenised for 2 h at 570ºC (a): large dispersoids (≥ 300 nm) have body-centred cubic crystal structure (b) and a low Mn:Fe-ratio (d), while small dispersoids (approximately 100 – 300 nm) have a simple cubic structure (c) and a high Mn:Fe-ratio (e).

4.3.3 Relating quench sensitivity to dispersoid density

Figure 4-12 shows quench sensitivity versus dispersoid number density in different commercial 6xxx series alloys (Figure 4-12a), where differences in dispersoid density are the result of the differences in alloy compositions, and in a AA6082-type alloy, where the differences in alloy composition are the result of different homogenisation treatments. In both cases quench sensitivity is determined from hardness measurements as the difference in hardness of samples quenched in water and samples cooled at still air after 24 h natural ageing and 8 h artificial ageing.
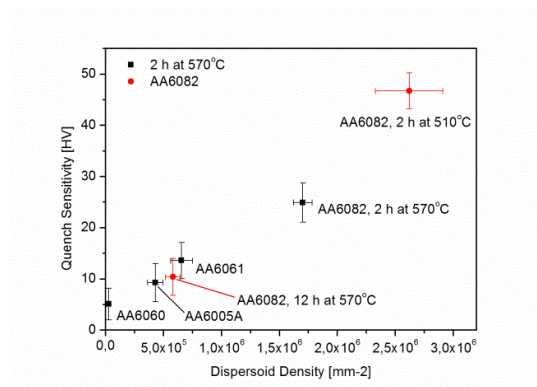
Figure 4-12 Relationship between dispersoid density and quench sensitivity in (a) the investigated 6xxx series alloys and (b) various AA6082 samples homogenised under different conditions.

The linear relationship between quench sensitivity and dispersoid density highlights that dispersoid density is much more important than the alloy composition variation. Commercial alloys also vary in Mg and Si content, which affects the driving force for precipitation. In the different AA6082 samples, however, variations in Mg and Si content at a certain distance from the precipitation site are expected to be small, such that the driving force for the precipitation of strengthening phases is hardly affected. It can therefore be concluded that the difference in quench sensitivity is caused by the difference in dispersoid number density.

4.4 Discussion

This work indicates that the dispersoid density is a key factor that affects the quench sensitivity of an alloy and that there is a directly proportional relationship between the two (Figure 4-12); at least in the 6xxx series processed under equivalent conditions. While the data shows such a strong relationship, it is important to consider whether this should be the case or not, and moreover whether this can be expected to universally be the case.

At industrially relevant cooling rates dispersoids act as precipitation sites for non-hardening Mg-Si-containing phases and hence promote solute loss. This precipitation can also take place at other precipitation sites such as grain boundaries and/or

dislocation lines. Although, due to their lower distribution, nucleation on these sites is less common.

6xxx series extrusion alloys all contain dispersoids that are very similar in their size and composition (Table 2-2).The size, composition and crystal structure of dispersoids are determined by the homogenisation treatment and the alloy composition, in particular the transition metal content. For transition metal contents typical in the alloys investigated (Mn < 0.6wt.%, Cr < 0.3wt.%) all dispersoid phases are based on the primary intermetallic phases $Al_{12}Fe_3Si$ or $Al_{15}Mn_3Si_2$[29, 130].This means that all dispersoids have a cubic unit cell with the cell parameter a=1.26nm (e.g. Figure 4-7d), so that the interfacial energy is expected to be very similar. The potential of each single dispersoid to act as a nucleation site is hence the same, particularly since the size of the dispersoids are very similar after 2 h homogenisation at 570ºC independent of the alloy composition. Consequently it can be assumed that the nucleation kinetics would be the same in each of the alloys.

By investigating quench sensitivity after different homogenisation treatments, the dispersoid size was found to have little effect. Despite significant difference in dispersoid size distribution in samples of AA6082 (Figure 4-10b), the quench sensitivity was again linearly related to the dispersoid density (Figure 4-12b). Hence, at least for this alloy it appears that dispersoid size in the observed range of 50 to 500nm has little effect on the quench sensitivity and consequently it appears that dispersoid size has little effect on the nucleation kinetics. One of the important clues is that although the crystal structure of the dispersoids varies slightly, all show a cubic structure with the same unit cell parameter (Figure 4-11). Therefore it is expected that all dispersoids present under the conditions described above have the same potential as nucleation sites for Mg-Si phases.

However, the initial research also shows the need for further investigations. In order to be able to fully describe quench sensitivity, the role of alloy composition, in particular Mg-, Si- and Cu-content as well as the origin of quench sensitivity in AA6060 has to be explained. In addition, the present investigations were conducted with a natural ageing

time of 24 h. This is an overly long natural ageing time for industrial extrusion processing, where natural ageing times are typically between 30 min and 4 h. As natural ageing has a significant effect on the artificial ageing response (2.5.2), it is important to investigate quench sensitivity without natural ageing and with industrially relevant natural ageing times.

The difference between the Cu-free and Cu-containing alloys is most likely due to differences in precipitation during cooling from extrusion temperature and/or age hardening. Although Cu is found in the non-hardening precipitate and therefore partly removed from the solid solution during slow cooling, it is expected that the remaining Cu in solid solution affects clustering during natural ageing as well as precipitation of strengthening phases during artificial ageing. These findings suggest that quench sensitivity is not only dependent on precipitation and the related solute loss during cooling, but also depends on the alloy's natural and artificial ageing response, which in turn may be influenced by the cooling rate.

The other interesting result is that in alloy AA6060, which contains only 0.04Mn and where only a small number of dispersoids is observed, it appears that quench sensitivity cannot be related to dispersoid density. One explanation for its quench sensitivity can be drawn using Shuey's et al. findings [6], which describe solute loss not only to precipitation on dispersoids but also to precipitation on grain boundaries. This leads to the conclusion that in cases where dispersoids are present, the precipitation of non-hardening phases occurs on the dispersoids with their density being the dominant factor, and in the case where no dispersoids are present, precipitation could occur on other heterogeneous nucleation sites. The DSC results, however, indicate that no precipitation occurs during the cooling of AA6060 (Figure 4-2). Therefore, other factors are likely to be responsible for the loss in hardness. A possible explanation lies in the reduced amount of vacancies due to slower cooling rates. Vacancies are involved in early clustering during ageing [131] and a lower vacancy concentration will reduce the ageing response of an alloy.

These two observations suggest that quench sensitivity, i.e. the dependence of properties after age-hardening on the quench rate after extrusion, not only depends on solute loss during cooling after extrusion. Although vacancy loss occurs during cooling, its effect becomes obvious only during and after age-hardening. Therefore, an investigation of the natural and artificial ageing response is required in order to be able to determine the contributions of vacancy loss and the amount and ratio of the strengthening-phase-forming alloying additions Mg, Si and Cu.

4.5 Conclusions

The initial research shows that dispersoids, in particular the number density of dispersoids, play a significant role in quench sensitivity. This is mainly due to dispersoids acting as precipitation sites for the non-hardening Mg-Si-phase, leading to solute loss and a reduced amount of Mg and Si available for subsequent precipitation hardening. These results confirm the general knowledge about quench sensitivity.

However, the concept of solute loss during slow cooling fails to offer a sufficient description of quench sensitivity. Quench Sensitivity in an alloy with a very low dispersoid density together with the discrepancy between formation-enthalpy of precipitates during cooling and quench sensitivity in the Cu-containing alloy AA6061 strongly suggest that natural and artificial ageing kinetics also contribute to quench sensitivity. The age-hardening response after quenching at different rates is expected to give valuable information on the role of quenched-in vacancies and content of Mg, Si and Cu and will be investigated in the subsequent chapters.

Chapter 5 Quench Sensitivity in a soft Al-Mg-Si alloy

5.1 Introduction

It was found in Chapter 4 that the soft commercial alloy AA6060 shows significant quench sensitivity despite the number density of secondary dispersoids in this alloy being small and no precipitation being detected at the respective cooling rates using DSC. This suggests that there are more factors contributing to quench sensitivity besides the presence of secondary dispersoids. Recent work by Pogatscher et al. [43] strongly suggests that the number of mobile, non-equilibrium vacancies determines the artificial ageing response. The concentration of mobile, non-equilibrium vacancies in turn is strongly dependent on the quench rate from extrusion temperature. This chapter, therefore investigates quench sensitivity in the soft commercial alloy AA6060, where the role of quenched-in vacancies can be studied largely independent from solute loss to Mg-Si-containing precipitates on dispersoids.

5.2 Results

This study focuses on the three stages of the production process that are crucial for quench sensitivity i.e. the microstructure after homogenisation, solute and vacancy supersaturation and subsequent loss during cooling from solution treatment temperature and age hardening. The investigation is conducted for three conditions: the quench-rate dependent age hardening response at 190ºC is investigated after 2 min, 30 min and 24 h of natural ageing. Differences in the age hardening response depending on quench rate and natural ageing time are evidence for the role of vacancies in quench sensitivity. Electron microscopy is used to investigate the microstructure, in particular microstructural differences as a result of varying quench rates. Positron annihilation lifetime spectroscopy (PALS) is used to monitor in-situ quench-rate dependent differences in the formation of clusters and annihilation of vacancies at room temperature.

5.2.1 Hardening Response

Figure 5-1 shows the hardening response of water quenched (WQ), oil quenched (OQ) and air cooled (AC) samples during natural ageing. In general the hardness is relatively low and the hardness increase during natural ageing is small in the soft alloy AA6060. The hardness is greatest for the water quenched samples, both directly after quenching and during room temperature ageing. The development in hardness of the oil quenched sample and the air cooled sample are effectively indistinguishable throughout natural ageing, and the differences in hardness between these three samples are small after a prolonged natural ageing time of 6×10^4 min (1000 h).
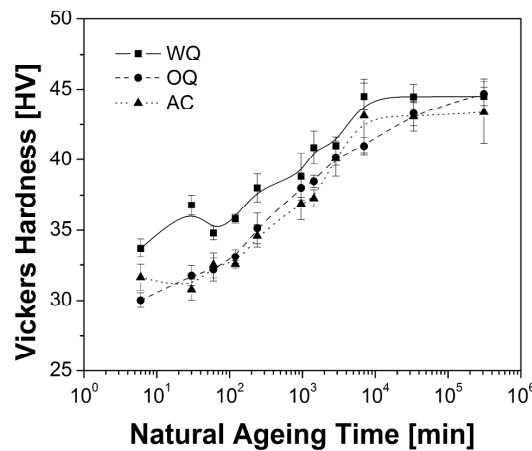
Figure 5-1 Hardness evolution during natural ageing of alloy AA6060 after three different quench rates: water quenched (WQ), oil quenched (OQ) and air cooled (AC).

Figure 5-2 shows the artificial ageing response of AA6060 at 190ºC after 2 min, 30 min and 24 h natural ageing. Two minute natural ageing was chosen as it is the minimum time needed to quench and transfer samples. The air cooled sample was left on an alumina bed to cool to about 80ºC and cleaned in cold water before it was transferred to the oil bath for artificial ageing. 30 minutes natural ageing represents a typical minimum floor time during an industrial extrusion process. 24 h represents an overly long natural ageing time for industrial practice, as used in previous studies [8, 132] and Chapter 4.

Immediately after quenching the hardness was determined to be 34 ± 1 HV for the water quenched samples, 30 ± 1 HV for the oil quenched samples and 32 ± 1 for the air cooled sample.

After 2 min natural ageing, the air cooled samples reach higher peak hardness values than the water quenched and oil quenched samples (Figure 5-2a). This order is unexpected as it does not correlate with cooling rates but is reproducible.
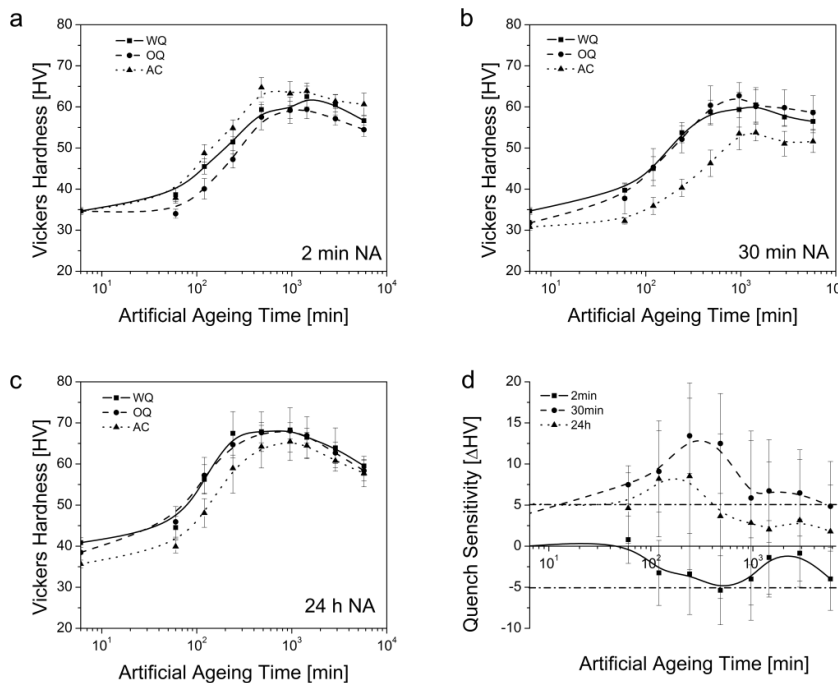
Figure 5-2 Artificial ageing response of AA6060 at 190ºC after cooling from solution treatment temperature to room temperature at different quench rates and natural ageing for (a) 2 min, (b) 30 min and (c) 24 h. The difference between the hardness of water quenched and air cooled samples (quench sensitivity) during artificial ageing is show in (d).

After 30 min natural ageing, the hardness response upon artificial ageing of the water quenched and oil quenched samples is similar. Both reach peak hardness values of approximately 60 HV (Figure 5-2b). The hardness response of the air cooled sample is slower than the other two samples especially in the first hour of artificial ageing, which together with the lower initial hardness for the air cooled samples, results in significantly lower peak hardness.

Immediately after 24 h natural ageing, the hardness of both the water and oil quenched samples is slightly higher than that of the air cooled sample (Figure 5-2c). During artificial ageing, all samples reach higher hardness values than after 2 min and 30 min natural ageing, therefore showing a positive response to prolonged natural ageing. Both the water quenched and air cooled samples reach similar hardness values of approximately 68 HV, while the air cooled sample reaches a slightly lower peak hardness of 65 HV. Whilst the peak hardness for all three cooling conditions is similar, the hardness of air cooled samples is lower during the earlier stages of artificial ageing compared to water and oil quenched samples.

The difference in hardness between water quenched and air cooled samples (quench sensitivity) are shown in Figure 5-2d. It is apparent that quench sensitivity is not uniform and varies with natural and artificial ageing time. It ranges from negative values i.e. a positive effect of slow cooling for 2 min natural ageing, to high positive values for 30 min natural ageing with long natural ageing times (here 24 h) showing very little quench sensitivity. To compensate for experimental uncertainty, a difference of greater than ±5 HV was used to indicate significant quench sensitivity. The greatest differences (10-15 HV) are reached after 30 min natural ageing and for 120 – 480 min artificial ageing. For both very short and longer natural ageing times, quench sensitivity is not significant.

The peak hardness values and the artificial ageing time to peak hardness are summarised in Table 5-1. With the exception of the air cooled samples after 2 min natural ageing, the peak hardness increases with increasing natural ageing time, showing that prolonged natural ageing has a positive effect on the achievable hardness. Although the peak hardness varies between 54 HV and 68 HV (25%) depending on the cooling conditions and natural ageing time, the time to peak hardness (~1000 min) is nearly independent of both the cooling rate and natural ageing time.

Table 5-1 Summary of peak hardness [HV] and time to peak hardness (in bracket) during artificial ageing at 190°C after different natural ageing times.

Natural Ageing Time	Cooling method		
	Water quenched	Oil quenched	Air cooled
2 min	62 ±3 HV (24 h)	59 ± 3 HV (16-24 h)	64 ± 3 HV (8-16 h)
30 min	60 ± 4 HV(24 h)	63 ± 3 HV (16 h)	54 ± 4 HV (16-24 h)
24 h	68 ± 5 HV (16 h)	68 ± 2 HV (16 h)	65 ± 5 HV (16 h)

5.2.2 Thermal Analysis

Figure 5-3 shows DSC curves during heating at 10 K/min of water quenched AA6060 samples. The curves after short natural ageing times (2 min and 30 min) show very small, exothermic peaks at around 70-90ºC, which can be related to early clustering reactions and a large, exothermic peak at around 250-300ºC. The small peak, marked as peak A, is related to cluster formation. The large peak, marked as peak D, is related to the precipitation of strengthening β"-precipitates. After 24 h natural ageing the DSC curve does not show an initial exothermic clustering peak, but rather what appears to be two endothermic peaks at 125ºC (B) and 225ºC (C) [90]. The peak for the formation of strengthening precipitates (D) is significantly larger in the sample naturally aged for 24 h than in the samples naturally aged for 2 min and 30 min.
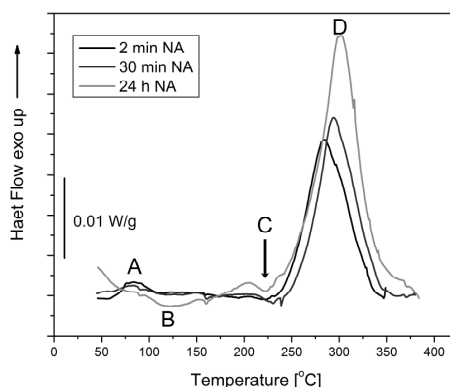
Figure 5-3 DSC curves of water quenched AA6060 samples after 2min, 30 min and 24 h natural ageing.

These results demonstrate that clustering occurs during storage at room temperature and starts immediately after quenching, since there is an observable decrease in peak A between 2 min and 30 min natural ageing. In the sample naturally aged for 24 h clusters formed during natural ageing lead to a higher peak D, i.e. the formation of a greater amount of strengthening β"-precipitates.

5.2.3 Microstructure Characterisation

The microstructure was investigated at three stages during the production process. After homogenisation (before solution treatment), the number density of dispersoids, which potentially act as precipitation sites, is determined. After cooling from solution treatment temperature, the effect of cooling rate on the precipitation of non-hardening precipitates is investigated. The distribution of strengthening precipitates during age-hardening contributes to an explanation of both the effect of solute loss and quenched-in vacancies on quench sensitivity.

5.2.3.1 Microstructure after homogenisation

As a result of homogenisation heat treatment and extrusion, the microstructure of the investigated AA6060 shows very fine secondary dispersoids, indicated by the black arrow, and broken up primary intermetallics, indicated by the white arrow (Figure 5-4).
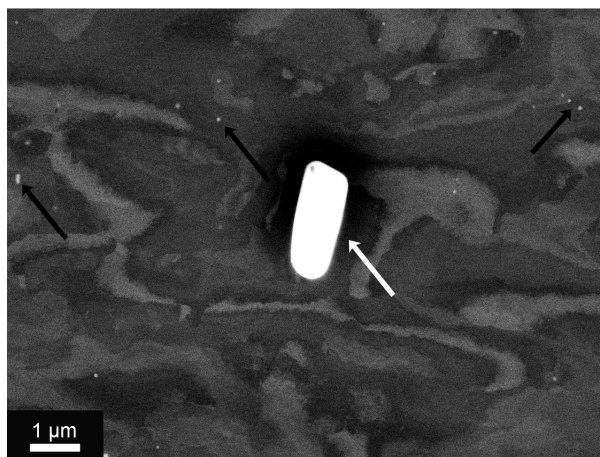
Figure 5-4 Back scattered electron micrograph showing the microstructure of AA6060 after homogenisation and extrusion showing relatively coarse, broken up primary intermetallics (white arrow) and very fine secondary dispersoids (black arrow).

The dispersoid number density in AA6060 was found to be very low ($2.6 \times 10^4 \pm 1 \times 10^4$ /mm^2) and inhomogeneous. Compared to the harder alloys with higher Mn- and Cr-contents, dispersoids in AA6060 are small with an average equivalent diameter of about 150 nm (± 70 nm).

5.2.3.2 Precipitation during cooling

Figure 5-5 shows Mn- and Fe-containing dispersoids, most likely α-Al$_{15}$(MnFe)$_3$Si$_2$ [130], in an air cooled and a water quenched sample. In the air cooled sample (Figure 5-5a), a Mg-and Si-containing phase has precipitated on the dispersoid during slow cooling resulting in a small precipitate free zone (~300 nm in diameter) around the dispersoid.
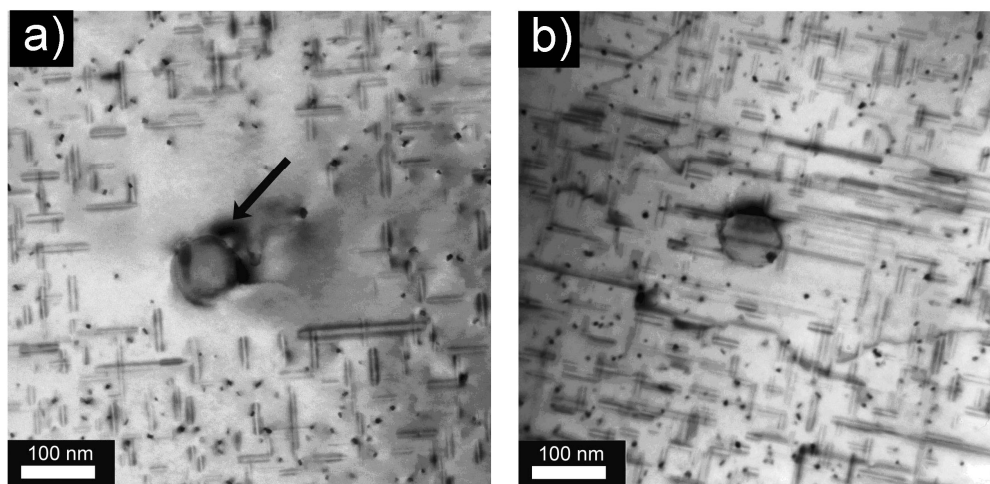
Figure 5-5 TEM micrographs showing Mn- and Fe-containing dispersoids surrounded by strengthening precipitates in (a) the air-cooled and (b) water-quenched AA6060 after 2 min natural ageing and 1440 min artificial ageing. In (a), precipitation of a non-hardening Mg-and Si-containing phase (indicated by arrow) on a dispersoid during air cooling resulted in a PFZ around the dispersoid. In (b), the precipitation of non-hardening phases did not occur on the dispersoid and hence there was no associated PFZ.

The microstructure in this sample, consisting of hard precipitate containing areas and soft precipitate free zones, can be described as a composite structure [38]. As the dispersoid density is very small and TEM micrographs therefore do not offer reliable statistics, the fraction of the soft precipitate free zone was estimated using measurements of the PFZ-fraction of the alloy BA (6.2.3.5). TEM images have shown that each single PFZ is approximately the same size in air cooled samples of alloy AA6060 and in air cooled alloys of alloy BA. The fraction of PFZ is therefore assumed to be only dependent on the number density of dispersoids and is estimated to be about 1%. The effect of the PFZ on the bulk hardness is expected to be negligible. In the water quenched sample (Figure 5-5b) with a similarly low number density of dispersoids, the strengthening precipitates are evenly distributed throughout the matrix, including within the proximity of the dispersoids.

5.2.3.3 Microstructure during Age-Hardening

The precipitate size and distribution during artificial ageing is investigated in order to relate it to the measured hardness (Figure 5-2). For all investigated natural ageing times (2 min, 30 min and 24 h) precipitates are observed after 2 h of artificial ageing at 175ºC. The precipitate size and distribution after a fixed artificial ageing treatment

indicates the maturity of the microstructure and allow conclusions on the precipitation kinetics.

The thickness of the TEM foils has neither been measured by electron energy loss spectroscopy (EELS) nor using convergent beam electron diffraction (CBED) patterns. Therefore, the precipitate density cannot be measured quantitatively. However, as overview images of the precipitate distribution were taken from thin sections that could be illuminated evenly, semi-quantitative comparisons between the different natural and artificial ageing conditions can be drawn.

Microstructural observations (Figure 5-6 & Figure 5-7) indicate that the air cooled sample contains fewer finer precipitates than the water quenched sample. After short artificial ageing times (here 2 h, see Figure 5-6), only a few, very small precipitates are visible in the air cooled sample, whereas precipitates in the water quenched sample are significantly coarser and more widely distributed. The relatively high hardness in the air cooled sample at this stage suggests that the sample also contains clusters and GP-zones that are not visible under conventional TEM.
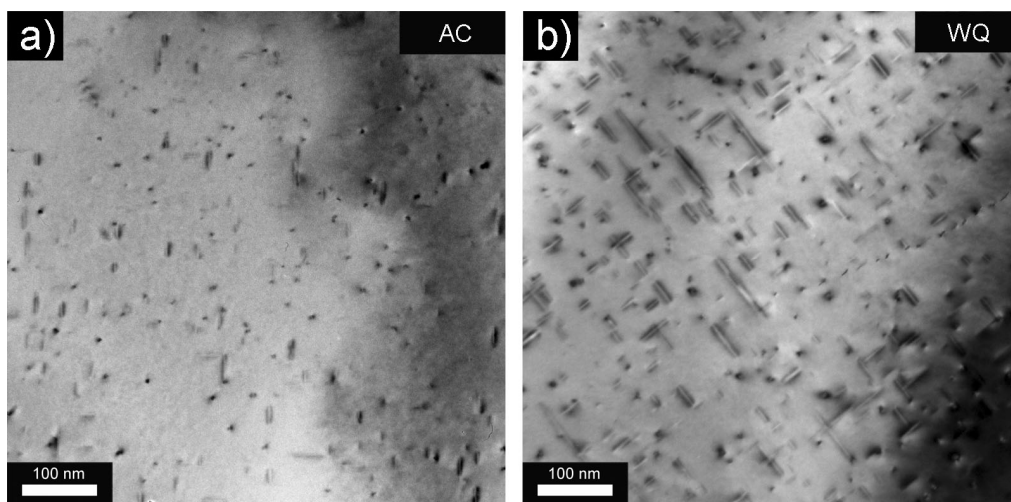
Figure 5-6 Distribution of strengthening precipitates in AA6060 after 2 min natural ageing and 2 h artificial ageing in an air cooled sample (a) and a water quenched sample (b).

After long artificial ageing times (here 24 h, Figure 5-7), the difference in the distribution of strengthening precipitates is much smaller between the air cooled and water quenched samples. Both samples show mainly rod-shaped β"-precipitates. The

air cooled sample however, contains a higher concentration of smaller precipitates compared to the water quenched sample. This might be the result of clusters and/or GP-zones that precipitated during slow cooling acting as nucleation sites for β"-precipitates during artificial ageing.
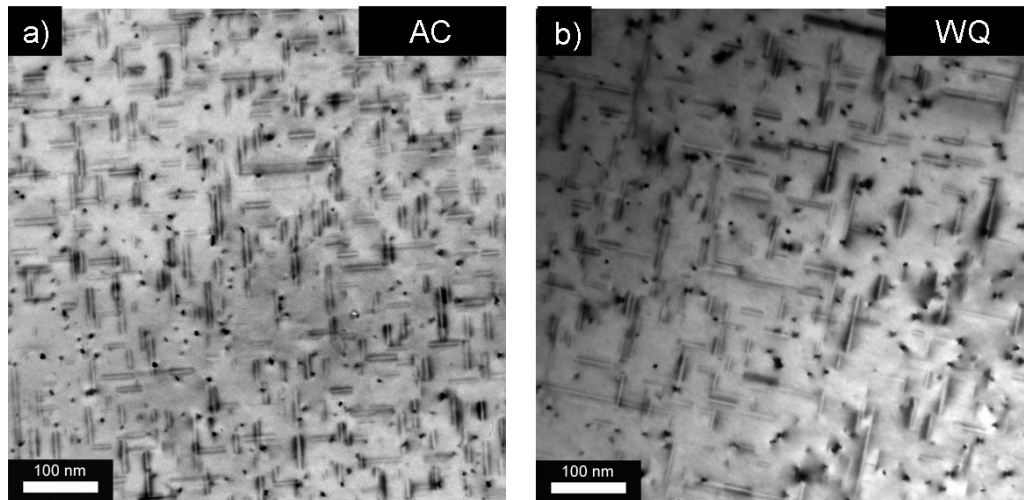
Figure 5-7 Distribution of strengthening precipitates in AA6060 after 24 h natural ageing and 24 h artificial ageing in an air cooled sample (a) and a water quenched sample (b).

The precipitate distribution after 30 min natural ageing and 2 h artificial ageing (Figure 5-8) shows a similar number density in both the air cooled and water quenched samples. Compared to the microstructure after 2 min natural ageing (Figure 5-6), a denser distribution of larger precipitates is found in samples naturally aged for 30 min. The precipitates appear to be larger and hence more mature in the water quenched sample. This reflects the significantly higher hardness achieved in the water quenched sample.
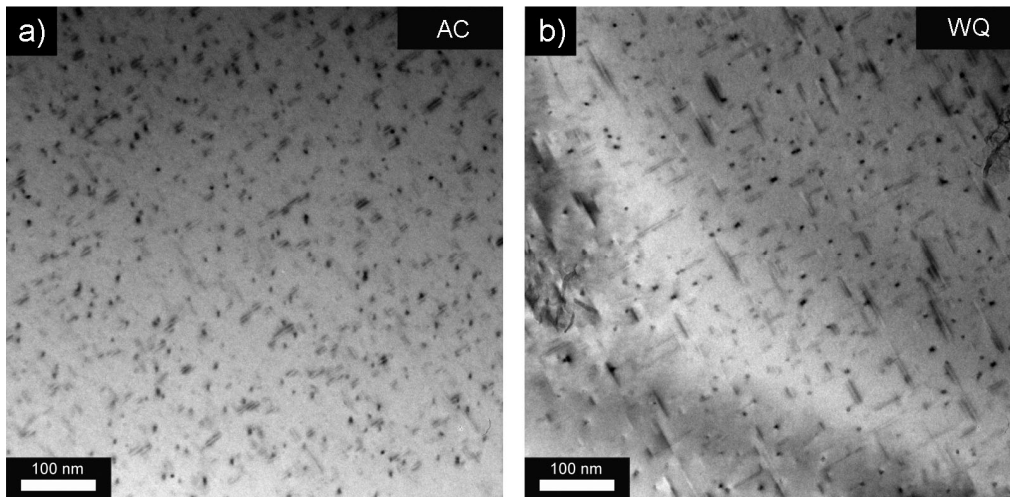
Figure 5-8 Distribution of strengthening precipitates in AA6060 after 30 min natural ageing and 2 h artificial ageing in an air cooled sample (a) and a water quenched sample (b).

The precipitate distribution after 24 h natural ageing and 2 h artificial ageing (Figure 5-9) is more mature than after shorter natural ageing times and 2 h artificial ageing (Figure 5-6 & Figure 5-7). In Figure 5-9 it appears that the air cooled sample contains a much higher number density of strengthening precipitates than the water quenched sample implying lower strength and hardness in the water quenched sample. However, it has to be considered that the foil thickness has not been measured. The difference in precipitate density can be exaggerated by a difference in foil thickness.
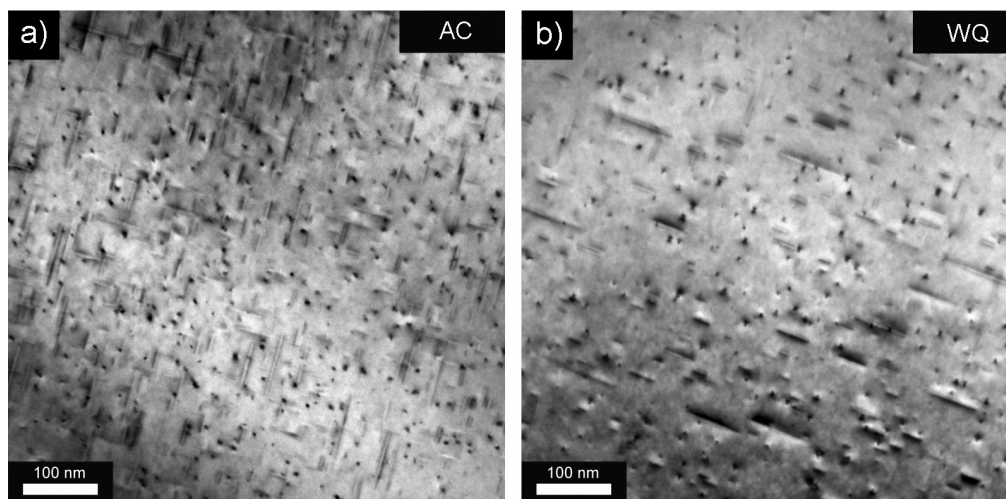
Figure 5-9 Distribution of strengthening precipitates in AA6060 after 24 h natural ageing and 2 h artificial ageing for an air cooled sample (a) and a water quenched sample (b).

5.2.4 Vacancies and Clustering

To investigate the effect of quench rate on vacancy concentration, mean positron lifetime values were measured for pure Al (99.99 %) (Figure 5-10). Positrons are sensitive to ~1 ppm vacancy concentration [118], and below this concentration the average positron lifetime is identical to that measured for well-annealed slow-cooled pure Al (162-168 ps) [121, 124, 126]. Although there can be monovacancy and extended lattice defects present at concentrations less than 1 ppm in the sample, the sensitivity of the average positron lifetime to these concentrations is negligible. This band of lifetime values between 162-168 ps is marked in Figure 5-10, and values of τ_{AV} in this band can be considered indicative of an equilibrium monovacancy concentration less than 1 ppm in well-annealed slow-cooled pure Al as measured by PALS.
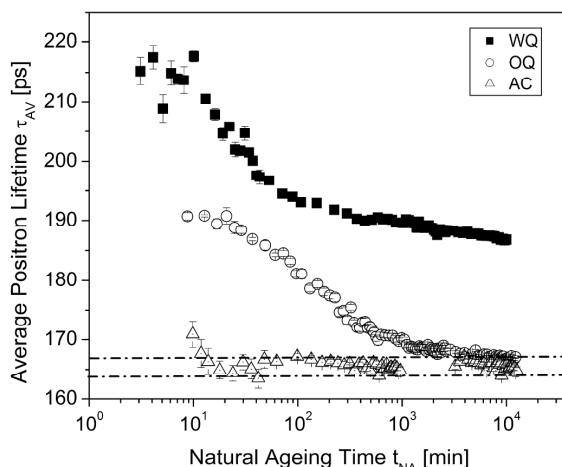
Figure 5-10 Average positron lifetime in samples of pure Al (99.99 %) during natural ageing after solution treatment at 550°C and quenching at different rates. The decrease in average positron lifetime indicates the annihilation of excess vacancies at room temperature directly after cooling. Horizontal lines indicate the average positron lifetime in well-annealed slow-cooled equilibrium aluminium [118, 133, 134].

The initial lifetime values after quenching of pure Al using three standard quench rates (water quenched, oil quenched, and air cooled) are indicative of an initial population of supersaturated vacancies that decays with time following the quench. The decrease in lifetime over time indicates the annihilation of vacancies at sinks such as grain boundaries. In the air cooled sample a vacancy concentration higher than 1 ppm is only measurable for a short time ($\approx$10 min). The oil quenched sample shows a steady decrease of τ_{AV} over a period of $\approx$10^3 min from 190 ps to approximately 168 ps. The average positron lifetime of the water quenched sample shows a steady decrease of τ_{AV} from 215 ps to 187 ps over a period of $\approx$10^4 min and does not reach 168 ps during the measurement period. This has been previously explained to be a result of quenched-in vacancies forming clusters that collapse and survive as Frank loops [41, 121].

The average positron lifetimes of AA6060 measured *in-situ* during natural ageing following different quenching conditions are presented in Figure 5-11. It can be seen that the effect of quenching on initial average positron lifetimes is similar to that observed in pure Al, with slower quenching rates resulting in lower initial lifetimes. The values of the initial positron lifetime in the quenched AA6060 samples are $\approx$5-10 %

higher than those in pure Al. These slightly higher values are likely to be due to solute-vacancy interactions [135].
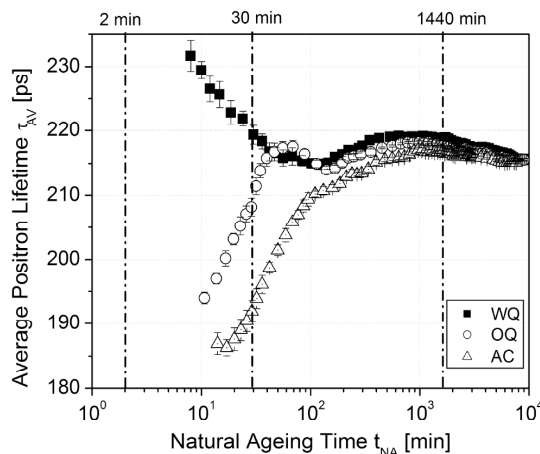
Figure 5-11 Evolution of average positron lifetime during natural ageing of alloy AA6060; vertical lines indicate the natural ageing times after which artificial ageing treatments were conducted.

The average positron lifetime data indicate that the dynamic processes in the alloy (vacancy diffusion and solute cluster growth) are active during natural ageing times up to 10^4 min (Figure 5-11). The alloys are initially at various stages of dynamic evolution due to the difference in quench rate. The artificial ageing experiment therefore begins at different stages of the dynamic natural ageing process for each of the quench rates, except for the prolonged natural ageing time of 24 h at which point the positron data indicate that all of the samples are at a similar stage of vacancy decay and solute cluster growth.

The water quenched sample shows an initial decrease in average positron lifetime to 215 ps during the first 120 min of natural ageing, then an increase to about 220 ps before a final decrease in lifetime to 215 ps for one week of natural ageing. This result is consistent with the change in average positron lifetime in previously published PALS results for natural ageing of water quenched 6xxx alloys [95, 96, 135]. These three stages of lifetime evolution have been attributed to the relative dominance over time of dynamic processes affecting the average positron lifetime: the initial decrease in the first 120 min is attributed to vacancy diffusion and annihilation to a τ_{AV} related to the formation of vacancy free clusters [97], the subsequent increase is attributed to

vacancy escape from growing solute clusters, and the final decrease is attributed to vacancy diffusion or coarsening of clusters [135].

Both the oil quenched and the air cooled samples experience an initial increase in average positron lifetime. The oil quenched sample shows a peak at 218 ps after 30-50 min natural ageing before subsequently reducing slightly after 120-180 min natural ageing and then recovering to a second peak in lifetime (216-220 ps) at about 1000 min natural ageing. This total time to reach the second peak is consistent with previously published results (900 ± 60 min) from a laboratory grade pure ternary alloy with similar concentrations of Mg and Si [96]. The air cooled AA6060 sample does not show a peak within the first hour of natural ageing, but shows a late peak after about 1000 min. The positron lifetime after prolonged natural ageing (~215 ps) is similar for the three cooling conditions and also much higher than that measured for water quenched pure Al after prolonged natural ageing (~185 ps). For natural ageing times up to 1000 min, decreases in τ_{AV} can therefore be attributed to vacancy annihilation and increases in τ_{AV} to solute vacancy clustering.

5.3 Discussion

In the following sections quench sensitivity is quantified first. While relations to well established measures such as dispersoid density are made, the key observation is that quench sensitivity is not only dependant on cooling rate but also on natural and artificial ageing time. The second part of this discussion gives possible explanations for these observations.

5.3.1 Quantification of Quench Sensitivity

In the following section the effect of solute loss is quantified. In addition the quench rate dependent differences in age-hardening response are compared to the effect of natural ageing on artificial ageing response and the two effects are rationalised.

5.3.1.1 The Role of Solute loss

The TEM results (Figure 5-5) show that solute loss to heterogeneous interfaces during cooling does occur in AA6060. The number density of dispersoids in the lean AA6060 alloy used in this work was estimated from SEM images to be $\approx 2.6 \times 10^4 \pm 1 \times 10^4$ /mm^2, which is significantly smaller than that found in medium- to high-strength alloys (between 5.4×10^5 /mm^2 for AA6005A and 1.2×10^6/mm^2 for AA6082) (Figure 4-5). Previously, a correlation was observed between number density of dispersoids and the enthalpy of the precipitation peak for non-hardening Mg-Si precipitates formed during cooling from solution treatment at 50 ºC/min in high strength alloys (Figure 4-6). However, for AA6060, no such peak was observed at 50 ºC/min, indicating that a dispersoid number density of ~2.6×10^4/mm^2 does not result in a measurable precipitation peak. Based on past work [132, 136], it is therefore assumed that for this very low dispersoid number density, there is negligible effect of solute loss on age hardening at the investigated quench rate of 50 ºC/min.

Given the negligible contribution from solute loss to dispersoids, the significant differences in hardness of 10-15 HV for commercially relevant natural and artificial ageing times between water quenched and air cooled samples observed in Figure 5-2d appear to be related to differences in vacancy concentration and mobility.

5.3.1.2 The role of natural ageing

During natural ageing there are two processes occurring simultaneously: clustering and annihilation of non-equilibrium vacancies. In soft Al-Mg-Si alloys clustering is known to lead to a hardness increase during natural ageing and also to an increased artificial ageing response [88, 98, 137]. The effect of vacancy annihilation and trapping acts in the opposite direction: vacancy annihilation during prolonged natural ageing leads to a reduced artificial ageing response.

Except for the hardness of the air cooled sample after 2 min natural ageing, the maximum hardness increases with increasing cooling rate and increasing natural ageing time. The increase of maximum hardness with natural ageing time is found to

be greater than the increase due to higher cooling rates. This means that clustering has a greater effect in this alloy than differences in vacancy concentration.

The increase in hardness due to natural ageing is not the same for all quench rates, i.e. it is greater in air cooled samples than in water and oil quenched samples. As a result, the hardness difference between air cooled and water quenched samples changes with changing natural ageing time. An explanation for this observation is given in the following sections.

5.3.2 Explanation of quench sensitivity

In the following sections, possible explanations for quench sensitivity are given based on the current investigations and published literature. Firstly, it is discussed how in particular a varying concentration of mobile, non-equilibrium vacancies affects the natural ageing response. Secondly, the effect of both clustering and vacancy loss on artificial ageing is discussed. Thirdly, the outcome of this chapter is summarised in a concept model.

5.3.2.1 Effect of natural ageing

Using the PALS results (Figure 5-10 and 11), the state of the samples immediately after cooling and the vacancy-related processes occurring during natural ageing can be discussed. In pure Al, the average positron lifetime at the beginning of the measurement, and thus the amount of quenched-in vacancies, is strongly dependent on the cooling rate [48]. The same trend is observed in the present study for AA6060, however the initial lifetimes for the three samples tend to be slightly higher (by ≈5-10%) than those measured in pure Al. These higher values can be attributed to interactions between vacancies and solute Mg and Si atoms [45, 121].

The average positron lifetime, τ_{AV}, is the weighted sum of the different positron lifetimes corresponding to annihilation at different traps within the material, τ_i:

$$\tau_{AV} = \sum \tau_i I_i \qquad\qquad 5\text{-}1$$

where I_i is the component intensity or statistical weight. More than a single lifetime could not be extracted from the PALS data suggesting either a single dominant lifetime, multiple lifetimes too close to be reliably distinguished, or a combination of both. The average positron lifetime data, however, do indicate more than a single dynamic process in the alloy. Previous work has shown that the data can be modelled using two positron traps, one associated with monovacancies diffusing to sinks and the other associated with vacancy escape from growing solute clusters [135]. The alloys are initially at various stages of dynamic evolution due to the difference in quench rate which affects the vacancy supersaturation and therefore the solute cluster reactions. Lay et al. [135] have shown that an initial exponential decay in mean lifetime (as observed in the water quenched sample) is due to processes associated with vacancy diffusion and annihilation. In contrast, according to Banhart et al. [97], the decrease in lifetime cannot be explained by an increased amount of positrons annihilating in bulk aluminium as a result of the loss of vacancies, but rather by the formation and growth of vacancy-free positron traps, most likely clusters, with a relatively low lifetime competing with vacancy related annihilation sites.

The current results are therefore interpreted in the following way: in water quenched samples the decrease of average positron lifetime in the early stages of natural ageing suggests mainly vacancy annihilation is occurring. The increase in hardness during these early stages however, shows that clustering is occurring at a significant rate. The observed average lifetime is therefore the result of a component associated with vacancy diffusion and annihilation and a component associated with clustering. Similarly, the average positron lifetime of the oil quenched and air cooled samples consist of several components, whereas, in contrast to the water quenched sample, the component associated with clustering is the dominant component.

After prolonged natural ageing times ($>10^3$ min), all samples have evolved from the initial state following quenching to reach a quasi equilibrium state with similar average positron lifetimes and similar dynamics. At the natural ageing times for which similar

positron lifetimes are observed in the present work, Lang et al. [39] observed a constant cluster site fraction independent of the cooling rate, indicating that cluster formation is completed at these natural ageing times. The mean positron lifetime dynamics for times $>10^3$ min has been attributed to vacancy diffusion to sinks, or, more likely, coarsening of clusters [96, 135]. This final stage in average positron lifetime decrease is similar for all samples: it relates to minimum quench sensitivity and has a positive impact on the achievable hardness during artificial ageing.

In summary, the average positron lifetime dynamics in AA6060 for three quench rates can be explained in terms of the dominance of the population of two trapping sites, one related to vacancies, the second to vacancy-free clusters. The changing dominance of these traps is then reflected in the material properties developed during natural ageing.

The average positron lifetime τ_{AV} (Figure 5-11) indicates that the relative intensities of solute clustering and vacancy annihilation during natural ageing differ greatly between the investigated samples depending on the cooling rate. As the hardness increase during natural ageing does not show significant differences between the water quenched sample and the air cooled or oil quenched samples (Figure 5-1, the differences in the evolution of the average positron lifetime seem to be mainly associated with differences in the concentration of mobile vacancies. The difference in the concentration of mobile, non-equilibrium vacancies however, does not appear to have a major influence on the natural ageing response.

5.3.2.2   Effect of artificial ageing

The three different natural ageing times prior to artificial ageing chosen relate to distinctly different states of the decomposing solid solution (Figure 5-2). As a result of the different initial states, the artificial ageing response shows distinct differences depending on cooling rate and natural ageing time. There were two key observations. One is the improved artificial ageing response with increasing natural ageing time. The other is very different effects that were observed with different natural ageing times

on the ageing response of the alloy when quenched at different rates, i.e. quench sensitivity.

The positive effect of prolonged natural ageing in low Mg- and Si-containing Al-Mg-Si alloys, observed in this study by increased hardness (Figure 5-2c) as well as in DSC scans which show increased β"-precipitation (Figure 5-3), is well known [87-89, 98], but only recently has work attempted to explain the microstructural processes behind this phenomenon [87, 88]. Chang et al. [98] attributed the increased maximum hardness reached during artificial ageing after prolonged natural ageing to the formation of Mg-Si co-clusters that can act as nucleation sites for precipitates which affects their composition and size. More recently, Pogatscher et al. [89] proposed that the co-clusters act as reservoirs that dissolve slowly during artificial ageing and provide previously unavailable solute Mg and Si for hardening precipitates. While the DSC results presented here highlight that a significantly higher amount of β"-precipitates forms after 24 h natural ageing, the PALS results indicate that after prolonged natural ageing times ($\approx 2 \times 10^3$ min), the driving forces behind decomposition have reached a quasi equilibrium state, independent of quench rate. These results suggest that cluster growth during natural ageing is necessary for the positive effect, but these results cannot discriminate as to whether the clusters act as nucleation sites or as solute reservoirs.

Insights into the mechanism of the effect of natural ageing of subsequent artificial ageing can be gained by considering the PALS data (Figure 5-11) in conjunction with the hardness measurements (Figure 5-2). As τ_{AV} data is available for 30 min and 24 h natural ageing, it is easier to consider their artificial ageing response before discussing the artificial ageing response after 2 min natural ageing.

The average positron lifetime τ_{AV} of the pure aluminium sample (Figure 5-2) indicates that after 30 min natural ageing there is still a significant vacancy supersaturation in the water and oil quenched samples, but not in the air cooled samples. After 24 h natural ageing, neither sample seems to have a significant supersaturation of mobile vacancies. The impact of the difference in vacancy supersaturation becomes apparent

when comparing equilibrium vacancy concentrations at different temperatures. The vacancy concentration at T = 550ºC, which is close to the vacancy concentration immediately after water quenching, can be approximated:

$$f_v \approx \exp\left(\frac{S_f}{R}\right)\exp\left(\frac{-E_f}{RT}\right)$$

5-2

$E_f \approx 67$ kJ/mol is the formation energy of a vacancy in Al, the gas constant R and the entropy $S_f \approx 0.6R$ [90]. The vacancy concentration at 550ºC is 1×10^{-5} per atom. In comparison, the equilibrium vacancy concentration at the artificial ageing temperature of 175ºC is 3×10^{-8} per atom and at room temperature (23ºC) 3×10^{-12} per atom. These approximate values correlate well with simulated values published by Falahati et al. [48], who used a model developed by Fischer et al. [41]. It can therefore be estimated that the vacancy concentration varies by several numbers of magnitude: a) between samples quenched at different rates after short natural ageing times; b) between water quenched samples naturally aged for different times.

After 30 min natural ageing the average positron lifetime τ_{AV} of the water quenched sample is still decreasing, indicating that there is still some vacancy supersaturation present at the start of artificial ageing. Although τ_{AV} of the oil quenched sample is increasing in the early stages of natural ageing, the peak at about 50 mins suggests some vacancy supersaturation being present as well. This is in contrast to the much lower τ_{AV} of the air cooled sample which indicates little vacancy supersaturation. As a result, the hardness increase occurs more rapidly in the water and oil quenched samples whereas it occurs much slower in the air cooled sample. Interestingly, the extra vacancy supersaturation in the water quenched alloy does not seem to have a significant benefit over the oil quenched sample.

At 24 h the average positron lifetime τ_{AV} of the pure Al samples has reached a steady state. This suggests that the similar τ_{AV}-values of the differently quenched samples of AA6060 are the result of a similar concentration of mobile, non-equilibrium vacancies. It remains unclear, whether and how the microstructure differs after 24 h natural

ageing depending on the cooling rate. As a result of a similar concentration of mobile, non-equilibrium vacancies, the age hardening response is very similar for all three samples (Figure 5-2c). The higher peak hardness of water and oil quenched samples after 24 h compared to the samples with shorter natural ageing times can be related to their higher hardness at the start of the artificial ageing treatment after 24 h natural ageing.

As there is no τ_{AV} data for 2 min natural ageing we attempt to approximate these values by extrapolating the existing PALS measurements (Figure 5-11). The lifetime τ_{AV} for the water quenched sample is very high, close to the lifetime of positrons in a vacancy surrounded by Al of 240 - 250 ps [96, 118], whereas τ_{AV} of the air cooled sample is low, close to the lifetime of positrons in bulk Al of ~165 ps [121, 124, 126]. Similar to the artificial ageing response after 30 min natural ageing, the water and oil quenched samples also show cooling rate dependent artificial ageing behaviour after 2 min natural ageing (Figure 5-2a). Air cooled samples however show an unexpectedly high hardening response, which may be related to clustering occurring during slow cooling at temperatures below 200ºC, whilst there may be still some vacancy supersaturation even upon slow cooling. The TEM micrographs of the sample naturally aged for 2 min (Figure 5-6 and 7) help explain this phenomenon. In air cooled samples a high distribution of fine, strengthening β"-precipitates after 24 h artificial ageing (Figure 5-7a) develops from few, very small and possibly some non-visible precipitates after 2 h artificial ageing (Figure 5-6a). In contrast to the air cooled samples, precipitates in water quenched samples are coarser and more densely distributed after 2 h artificial ageing and less densely distributed and bigger after 24 h artificial ageing. This supports that clusters are present at the start of artificial ageing, but not necessarily visible after 2 h artificial ageing and promote a high number density by acting as nucleation sites during further artificial ageing.

5.3.2.3 Concept model

The outcomes of this work are summarised in Figure 5-12. During solution treatment the majority of the strengthening phase forming elements Mg and Si are in solid

solution while the vacancy concentration is high. During quenching at high rates Mg and Si stay in solid solution and a high number of non-equilibrium (quenched-in) vacancies remain mobile at room temperature. In contrast, cooling conditions close to equilibrium, as present during air cooling, result in a low concentration of non-equilibrium vacancies. As the investigated alloy contains only a very small number of secondary dispersoids precipitation of Mg-Si-phases during cooling is not significant.
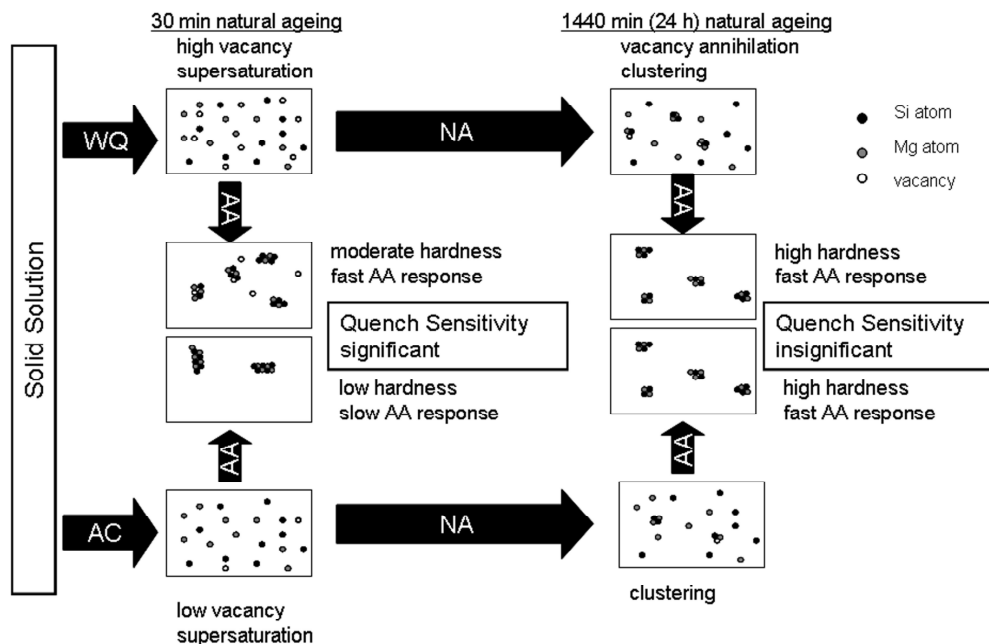
Figure 5-12 Schematic visualisation shows the effects of cooling rate and natural ageing time on age-hardening behaviour in AA6060. The artificial ageing response is compared after different quench rates (water quenched and air cooled) and for short and long natural ageing times (30 min and 24 h). The indicated microstructures are hypothetical and have not been verified experimentally.

During natural ageing two processes occur simultaneously: annihilation of vacancies and formation of Mg- and Si-containing clusters. As mobile vacancies enhance diffusion and hence solute transport, the high concentration of mobile vacancies present in fast cooled samples at shorter natural ageing times leads to faster clustering compared to slow cooled samples. As a result of these processes distinctly different states of the decomposing solid solution are found resulting in high quench sensitivity at 30 mins natural ageing. However at longer natural ageing times (24 hours), where the vacancy concentration has equilibrated, the quench sensitivity is small.

After short natural ageing times (here 30 min), water quenched samples might contain clusters as well as mobile vacancies. The presence of mobile vacancies leads to an enhanced artificial ageing response in water quenched as compared to air cooled samples, where artificial ageing is solely thermally activated and not enhanced by any quenched-in vacancies. Hence this will further enhance the quench sensitivity at shorter natural ageing times and explains why the quench sensitivity is greater at shorter artificial ageing times. After 24 h natural ageing, a significant number of clusters seem to have formed in the alloy independent of what the quench rate was. Hence the hardness response is faster during artificial ageing for long natural ageing times meaning that the ageing response is strong for the alloy despite differences in quench rate and the quench sensitivity is low (Figure 5-12).

5.4 Conclusions

It was found that loss of Mg and Si to non-hardening precipitates on dispersoids, which is generally considered the dominant mechanism, had little effect on quench sensitivity in the lean commercial Al-Mg-Si alloy AA6060. This is due to the low number density of dispersoids in this alloy. However, the combined use of positron annihilation lifetime spectroscopy and hardness measurements led to the conclusion that quench sensitivity in lean Al-Mg-Si alloys is strongly dependent on the cooling rate dependent supersaturation of vacancies. After short natural ageing times (30 min), which are typical for commercial extrusion, a rapidly declining vacancy supersaturation improves artificial ageing kinetics in fast cooled samples compared to slow cooled samples and thereby causes quench sensitivity. After longer natural ageing times, vacancy annihilation and clustering dominate the microstructure in both slow and fast cooled samples and consequently little quench sensitivity is observed. Hence the quench sensitivity measured in this AA6060 alloy is attributed predominantly to differences in vacancy concentration and mobility.

Chapter 6 Quench Sensitivity in dispersoid containing alloys

6.1 Introduction

The previous chapters have outlined the dependence of quench sensitivity on the number density of dispersoids (Chapter 4) and on cooling rate dependent artificial ageing kinetics (Chapter 5). This chapter rationalises and quantifies both of these influences in a dispersoid containing medium strength Al-Mg-Si alloy referred to as BA with the composition Al - 0.67% Si – 0.84% Mg – 0.35% Mn – 0.25% Fe in wt.%.

The focus of this chapter is to quantify and explain the influences of solute loss on dispersoids on the one hand and the quench rate dependent concentration of mobile, non-equilibrium vacancies on the other hand. The three stages of the production process most relevant to quench sensitivity, homogenisation, cooling after extrusion or solution treatment and age-hardening are therefore investigated. While the age-hardening response and thermal analysis offer quantitative information about quench sensitivity, microstructure characterisation and the monitoring of vacancies during natural ageing will help explain the observed phenomena.

6.2 Results

In this section the results of the investigation of the model alloy BA are presented. The quench rate dependent age-hardening response at 175ºC after 2 min, 30 min and 24 h of natural ageing demonstrates the magnitude of quench sensitivity. Thermal analysis of precipitation reactions occurring during cooling as well as during artificial ageing offers further quantitative and qualitative information on quench sensitivity. The characterisation of the microstructure at various stages is conducted to assist with rationalising the single effects on quench sensitivity. In order to monitor the evolution of mobile, non-equilibrium vacancies and clarify their role in quench sensitivity, positron annihilation lifetime spectroscopy (PALS) is carried out in-situ during natural ageing on samples quenched at different rates.

6.2.1 Hardness response

The hardening response is measured for samples quenched in water (~18.000 K/min), oil (~2000 K/min) and still air (~50 K/min) during both natural and artificial ageing. These results help clarifying whether quench sensitivity is solely the result of solute loss affecting small areas in the material (PFZ) or whether driving force and precipitation kinetics are also affected by slow cooling.

The hardening response during natural ageing (Figure 6-1) is dependent on the cooling rate after solution treatment. In the water and oil quenched samples the hardness increases faster and reaches higher values than in the air cooled samples. It should be noted that even after 10^5 min (70 days) natural ageing the hardness has not reached a constant value and hardness might therefore increase further.
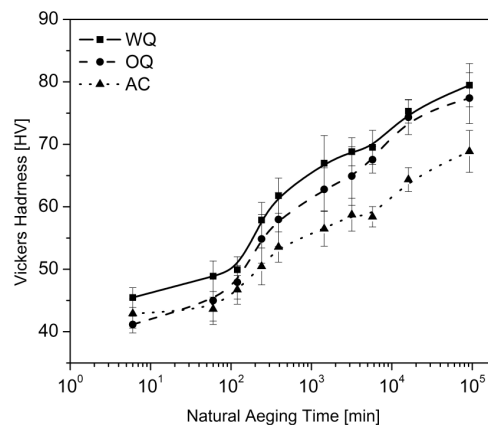
Figure 6-1 Hardening response of samples quenched at different rates during natural ageing.

Figure 6-2 shows the artificial ageing response at 175ºC after 2 min, 30 min and 24 h of natural ageing. The hardness after both natural and artificial ageing is generally greatest for the water quenched sample and lowest for air cooled. The respective water quenched sample reaches its peak hardness earlier compared to the oil quenched and air cooled samples.

After short natural ageing times (here: 2 min and 30 min) the initial hardness for the differently quenched samples shows little difference. The peak hardness of the water

quenched sample is reached after 1 h artificial ageing (2 min natural ageing time), the time when the first measurement was taken, and is at 117 ± 5 HV the highest hardness achieved in this alloy and therefore considered maximum hardness achievable (T6$_{max}$). The air cooled samples reach their maximum hardness of 88 ± 3 HV after 2 min natural ageing and 16 h artificial ageing.

Compared to the samples naturally aged for 2 min and 30 min, the initial hardness after 1440 min (24 h) of natural ageing is already significantly higher (Figure 6-1). However, in fast cooled samples (water and oil quenched) the respective peak hardness after artificial ageing is much less than after short natural ageing times Figure 6-2 a&b). This effect is commonly referred to as the negative effect of natural ageing in highly alloyed 6xxx series alloys [85, 88]. It is more pronounced for water and oil quenched samples than for air cooled samples. Although, the water quenched samples reach its maximum hardness significantly earlier than the air cooled sample (1 h versus 16 hr for 2 min NA and 8 h versus 32 h for 24 h NA), only the air cooled samples show an increase in peak hardness after 24 h natural ageing and hence do not experience the same negative effect (Table 6-1). As a result the differences in hardness evolution between the different cooling conditions are much less pronounced after 24 h natural ageing than after short natural ageing times of 2 min and 30 min.

Table 6-1 Summary of peak hardness and time to peak hardness (in bracket) during artificial ageing at 175°C after different natural ageing times.

Natural Ageing Time	Cooling method		
	Water quenched	Oil quenched	Air cooled
2 min	117 ± 5 HV (1 h)	112 ± 3 HV (4 h)	88 ± 3 HV (16 h)
30 min	110 ± 6 HV (1 h)	103 ± 3 HV (4 h)	87 ± 2 HV (16 h)
24 h	100 ± 6 HV (4 h)	91 ± 3 HV (8 h)	93 ± 2 HV (16 h)
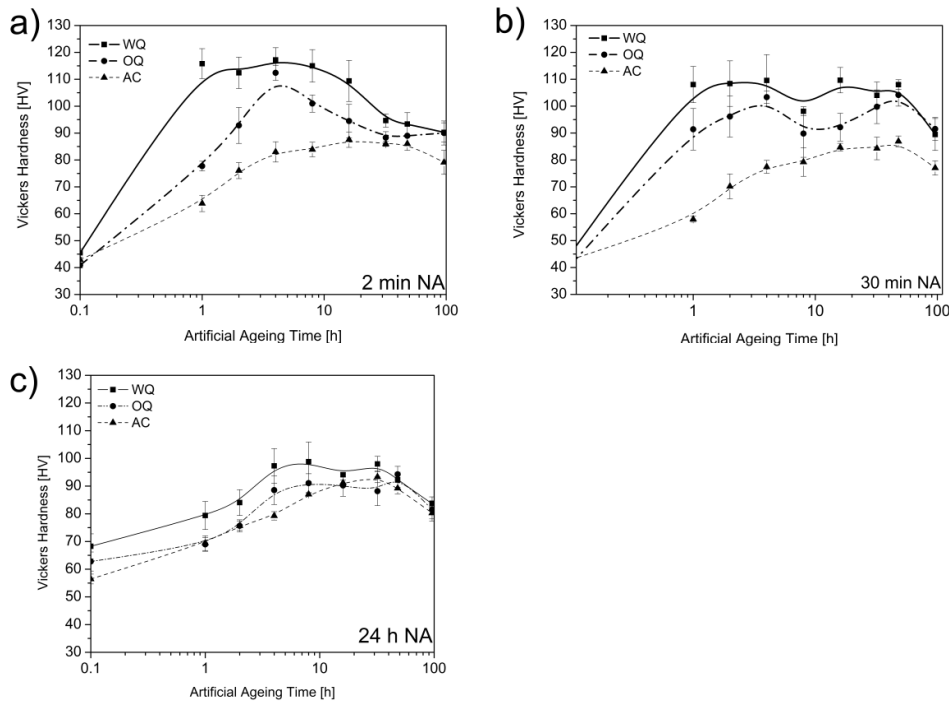
Figure 6-2 Artificial ageing response at 175ºC after a) 2 min, b) 30 min and c) 1440 min (24 h) natural ageing.

6.2.2 Thermal analysis

Differential scanning calorimetry has been conducted to characterise precipitation reactions occurring at two different stages during the production process. Firstly, the investigation of cooling rate dependent precipitation reactions during cooling after solution treatment is a means of gaining qualitative information about these reactions and quantifying solute loss (see Chapters 4 & 5). Secondly, the effect of cooling rate and natural ageing time on the kinetics of precipitation of strengthening phases is investigated by probing samples quenched at different rates and naturally ageing for different times.

6.2.2.1 Precipitation during cooling

Figure 6-3 shows the cooling rate dependence of the precipitation of two different phases in the investigated alloy. The range of cooling rates that could be investigated by differential scanning calorimetry is limited by the sensitivity (low cooling rates) and the cooling capabilities (high cooling rates) of the PERKIN ELMER DSC7. At lower cooling rates a clear separation of the two peaks is evident. With increasing cooling

rate the high temperature peak occurs at lower temperatures and is not detected for cooling rates of 100 K/min and higher. For most investigations in this work a cooling rate of 50 K/min was chosen as a representative of a slow cooling rate for medium to high strength Al-Mg-Si alloys. It is also the cooling rate achieved in air cooled samples in the laboratory set up and by a forced air quench during commercial extrusion.
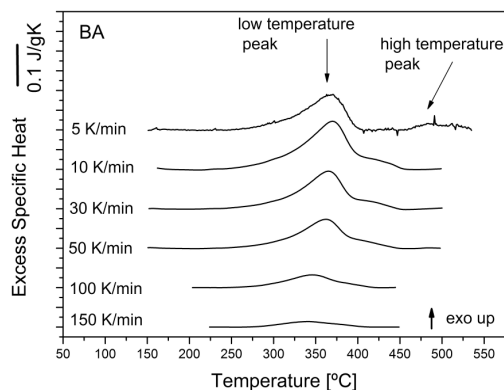
Figure 6-3 Precipitation during cooling recorded by DSC at different cooling rates shows how the amounts of Mg$_2$Si (high temperature peak) and β' (low temperature peak) precipitation are cooling rate dependent.

Figure 6-4 summarises the precipitation reactions occurring during cooling at rates between 5 to 150 K/min. For the hardness measurements (Figure 6-4), samples were cooled continuously at the respective rate in a DSC, stored at room temperature for 24 h and artificially aged for 8 h at 175ºC. It should be considered that this ageing treatment does not necessarily lead to peak hardness, but leads to results that can be compared in regards to solute loss (e.g. Figure 4-5).

For most samples there is an inverse relationship between hardness increase and the enthalpy of the formation of non-hardening Mg-Si-phases (Figure 6-4). The overall formation enthalpy is the sum of the formation of the high temperature phase (Mg$_2$Si) and the low temperature phase (β'-Mg-Si). At cooling rates of 100 K/min and higher the high temperature reaction is suppressed, so that only the low temperature reaction occurs. Comparable experiments in the literature for the commercial alloy AA6005A also show a slight decrease in, or rather constant formation enthalpy for cooling rates lower than 10 K/min [49]. This could be either the result of the

magnitude of the low temperature reaction decreasing and the magnitude of the high temperature reaction only slowly increasing for low, decreasing cooling rates or due to experimental inaccuracies as a result of the small signal.
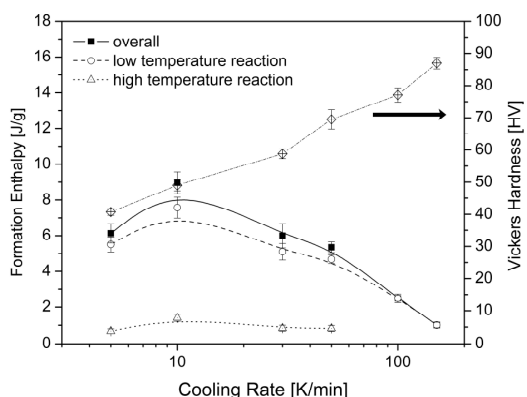
Figure 6-4 Comparison between the formation enthalpy of non-hardening precipitates in BA during cooling at different rates from Figure 6-3 and the achieved hardness for the respective samples after 24 h natural ageing and 8 h artificial ageing at 175ºC.

6.2.2.2 *Precipitation of strengthening phases*

The effect of varying cooling rates and natural ageing times on precipitation of strengthening phases was investigated by differential scanning calorimetry (DSC). Figure 6-5 shows DSC scans at a heating rate of 20 K/min for samples quenched in water or cooled in still air and 30 min natural ageing (Figure 6-5a) or 24 h natural ageing (Figure 6-5b). While the water quenched samples show distinct peaks for clustering, precipitation and dissolution reactions, peaks in air cooled samples are either not observable or overlap greatly. Water quenched samples after both natural ageing times show four exothermic peaks that are attributed to A: formation of clusters, C: formation of the strengthening β"-precipitate, D: precipitation of metastable β'-precipitates and E: formation of β-precipitates. The endothermic peak (B) is attributed to dissolution of clusters. The peaks for cluster formation (A) and dissolution (B), that are observed at approximately 90ºC and approximately 230ºC respectively in water quenched samples, are not observed in air cooled samples. This may be due to the formation being suppressed as a result of a lack of mobile vacancies and/or the amount of cluster formation and dissolution being too small to be

detected. In air cooled samples the peaks for β" and β' precipitation (C and D) overlap greatly and de-convolution is therefore very difficult. Peak E occurs at the same temperature for both air cooled and water quenched samples and is approximately the same size.

The effect of natural ageing is noticeable when comparing the DSC scans of the two water quenched samples (Figure 6-5). After 30 min natural ageing the peak for clustering (A) is larger than after 24 h natural ageing. This shows that clustering has already occurred during the 24 h of natural ageing as significant cluster dissolution peaks (B) are observed in water quenched samples after both 30 min and 24 h natural ageing.
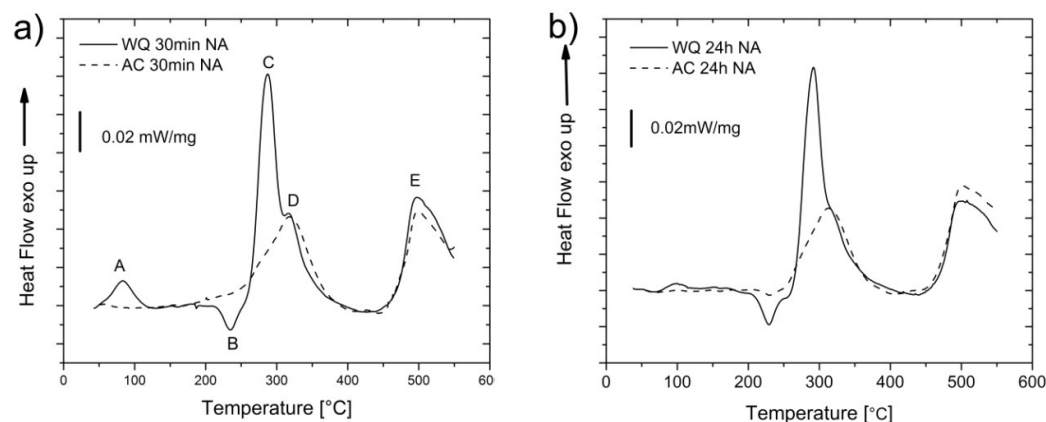
Figure 6-5 DSC curves at a scan rate of 20 K/min a) of samples naturally aged for 30 min and b) of samples naturally aged for 24 h. The letters A to E indicate exo- and endothermic peaks.

The formation of β" and β' precipitates appears to be greatly different in water quenched and air-cooled samples (Figure 6-5). Water quenched samples show a large peak for β"-formation and a significantly smaller peak for β'-formation (Table 6-2, Figure 6-6). For air cooled samples the combined β" and β' peak is at the same temperature as the β'-peak in the water quenched samples, indicating that the precipitation of the strengthening β"-phase is suppressed.

There are a number of possible explanations.

- The precipitation of β" during continuous cooling could be suppressed because β" has already formed during cooling from solution treatment temperature. This explanation is unlikely since the hardness observed prior to the DSC scan, i.e. after 30 min or 24 h natural ageing, would be expected to be significantly higher than the observed hardness of the respective naturally aged water quenched samples.

- The formation of β"-precursor phases, i.e. cluster(s) and/or GP-zones is suppressed and that as a result of that β" do not form/form to a lesser degree.

- During slow cooling vacancies annihilate/ form dislocation (loops) which, due to their high surface energy act as precipitation sites for β'.

Table 6-2 Peak temperatures and formation enthalpies for β" and β' formation in water quenched and air cooled samples after 30 min and 1440 min (24 h) natural ageing during heating at 20 K/min.

	clustering (A)		β" formation (C)		β' formation (D)	
	Peak Temperature [ºC]	ΔH [J/g]	Peak Temperature [ºC]	ΔH [J/g]	Peak Temperature [ºC]	ΔH [J/g]
WQ 30 min NA	83 ± 2	1.6 ± 0.4	284 ± 2	12 ± 0.5	322 ± 1	6.4 ± 0.2
WQ 24 h NA	96 ± 2	0.3 ± 0.1	289 ± 2	11 ± 0.6	330 ± 1	3.7 ± 0.6
AC 30 min NA	-	-	272 ± 4	3.5 ± 0.2	327 ± 2	7.2 ± 0.4
AC 24 h NA	-	-	286 ± 1	2.8 ± 0.3	325 ± 1	6.3 ± 0.3

Although the peak temperature for β"-precipitation does not show a correlation with either cooling rate or natural ageing time, the formation enthalpy for β" is significantly greater in water quenched samples than in air cooled samples. The enthalpy for the β" to β' transformation shows similar, low values for all four cooling/ageing combinations. As a result, $\Delta H_{\beta"}/\Delta H_{\beta'}$ is greater than one in water quenched samples and less than one in air cooled samples. This suggests that β"-precipitation is suppressed in air cooled

samples whereas β' forms preferentially. Since, β' is less effective in strengthening compared to β" [9, 11, 75], the quench sensitivity also appears to be affected by cooling rate dependent changes in the precipitation sequence.
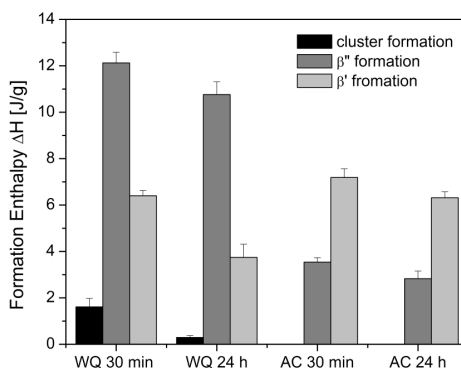
Figure 6-6 Formation enthalpies of cluster-, β"- and β'- formation at 20 K/min after water quenching and air cooling and natural ageing for 30 min and 24 h respectively.

6.2.2.3 Artificial Ageing Kinetics

The activation energies (E_a) for the formation of the different phases precipitating during natural ageing were determined for water quenched and air cooled samples from linear heating studies using a Type B-1.95 Peak method [115]. The estimated activation energies are summarised in Table 6-3.

Table 6-3 gives an overview of the determined activation energies for clustering, dissolution of clusters, β"-precipitation, the transformation of β" to β' and the formation of β-Mg$_2$Si. For the air cooled samples, peaks for clustering and cluster dissolution were not observed, hence no activation energy was determined. The determined activation energies do not in all cases correspond well with literature values. Since the activation energies in the literature [138, 139] have been determined in samples immediately after quenching from solution treatment temperature, deviations of the determined activation energies from the literature values may give information on the cooling rate and natural ageing time dependent differences of the precipitation sequence.
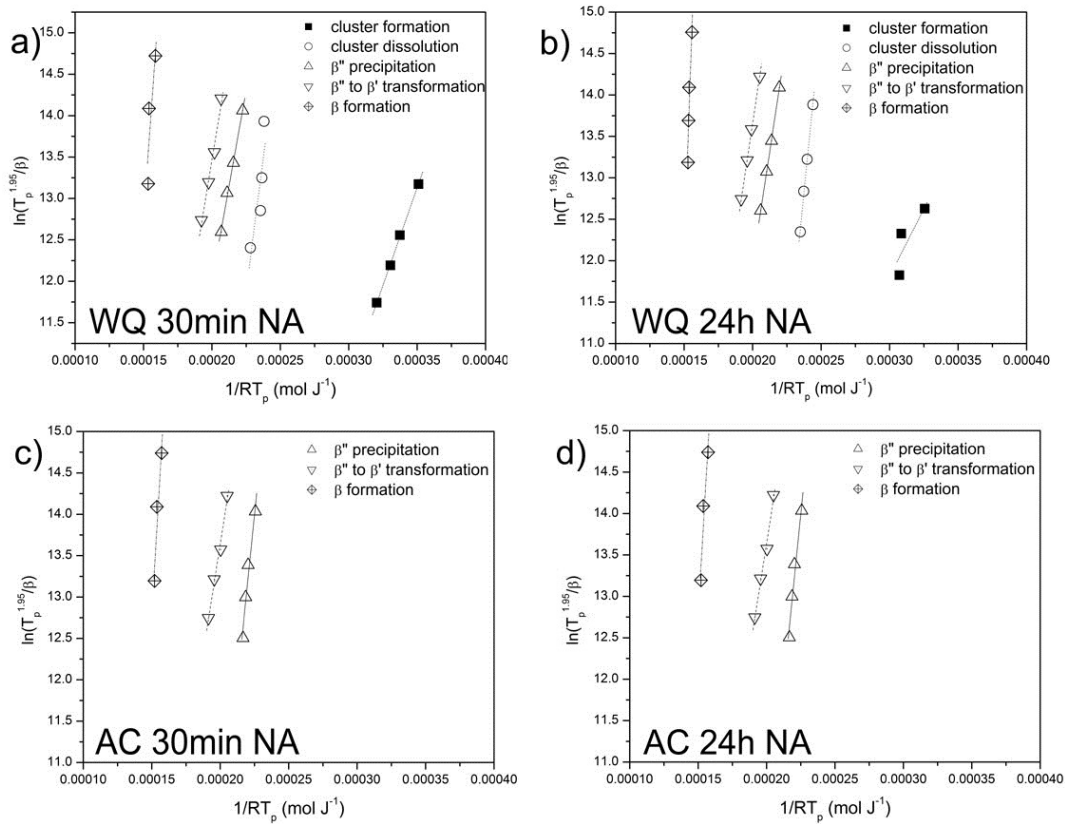
Figure 6-7 Shift of peak temperature (T$_p$) with varying heating rates (β) for (a) water quenched 30 min NA, (b) water quenched 24 h NA, (c) air cooled 30 min NA and (d) air cooled 24 h NA.

Table 6-3 Activation energies of phase transformation occurring during heating

	cluster formation (kJ mol^{-1})	cluster dissolution (kJ mol^{-1})	β"-precipitation (kJ mol^{-1})	β" to β'-transformation (kJ mol^{-1})	β-formation (kJ mol^{-1})
Literature	-	-	76.6 [139]	117.3 [139]	117.4 [139]
WQ 30 min NA	47	128	92	100	231
WQ 24 h NA	32	165	109	111	476
AC 30 min NA	-	-	162	105	281
AC 24 h NA	-	-	90	96	418

The accuracy of the determined activation energies of phase transformations is strongly dependent on the respective peak temperature determined by DSC. For

reactions where only a small volume fraction is transforming, in particular the formation and dissolutions of clusters the accuracy of the peak temperature is limited. Additional limitations to the accuracy of the measurement are given where peaks overlap and have to be separated. This occurs particularly in the air cooled samples as well as in measurements with a fast heating rate.

6.2.3 Microstructure Characterisation

The microstructure of model alloy BA is characterised at several stages of the production process. Firstly, the microstructure after homogenisation gives not only information about successful transformation of primary intermetallics but more importantly about the size and distribution of secondary dispersoids, which have great influence on quench sensitivity. Secondly, after cooling from solution treatment temperature coarse non-hardening Mg-Si-precipitates dominate the microstructure of slow cooled samples. The non-hardening β'-Mg-Si-phase is identified. Thirdly, strengthening precipitates are compared in samples naturally and artificially aged for different times are compared in order to help explain changes in ageing kinetics as a result of changing cooling rates.

6.2.3.1 Dispersoid phases after homogenisation

In the homogenised state the alloy shows coarse, primary, Chinese-script-like α-Al(Fe,Mn)Si intermetallics (Figure 6-8). These intermetallics are located on grain boundaries. A dense distribution of secondary α-Al(Fe,Mn)Si dispersoids has precipitated during heating to homogenisation temperature. The dispersoid density has been determined by image analysis of back-scattered SEM images to be $3 \times 10^5 \pm 7 \times 10^4/mm^2$. This is a slightly lower dispersoid density than the commercial alloys AA6061 and AA6082 (Chapter 4).
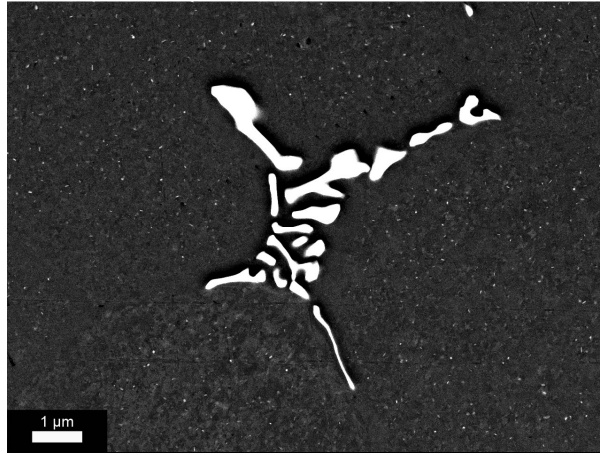
Figure 6-8 Microstructure of alloy BA, recorded in back scattered electron mode after homogenisation shows coarse, Chinese-script like intermetallics and finely dispersed secondary α-Al(Fe,Mn)Si phases within the grains.

6.2.3.2 Precipitation on dispersoids during cooling after solution treatment

Figure 6-9 shows TEM micrographs taken along $[001]_{Al}$ of two samples of the alloy BA that were solution treated, quenched in still air (Figure 6-9a) and water (Figure 6-9b) respectively, naturally aged for 24 h and artificially aged for 8 h. In the air cooled samples the microstructure is dominated by coarse, non-hardening phases that precipitated on Mn- and Fe-containing dispersoids along the <001> direction (Figure 6-10). These phases are surrounded by zones free of strengthening precipitates (precipitate free zones, PFZ, Figure 6-9a). In the water quenched sample (Figure 6-9b) neither coarse, non-hardening precipitates nor a precipitate free zone is observed.
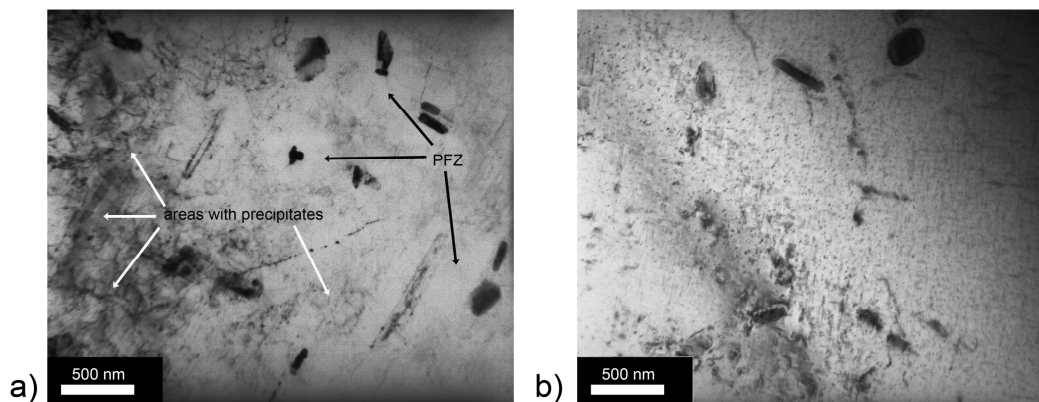
Figure 6-9 TEM micrographs taken along <001> of samples naturally aged for 24 h and artificially aged for 8 h. The air cooled sample (a) shows non-hardening precipitates on dispersoids surrounded by precipitate free zone. Black arrows are indicating examples of precipitate free zones, while white arrows are indicating areas where strengthening precipitates have formed and are surrounded by dislocations from sample preparation. In

the water quenched samples (b) neither coarse non-hardening precipitates nor precipitate free zones are observed.

6.2.3.3 Nature of the non-hardening phase

In air cooled samples with an approximate cooling rate of 50 K/min the microstructure is dominated by coarse, non-hardening precipitates that form during the low temperature reaction (Figure 6-3). They precipitate heterogeneously on secondary dispersoids (Figure 4-7). These phases contain Mg, Si and possibly Al and show a Mg:Si-ratio of 1.68 in wt.% (Figure 6-10b, Figure 6-10b).
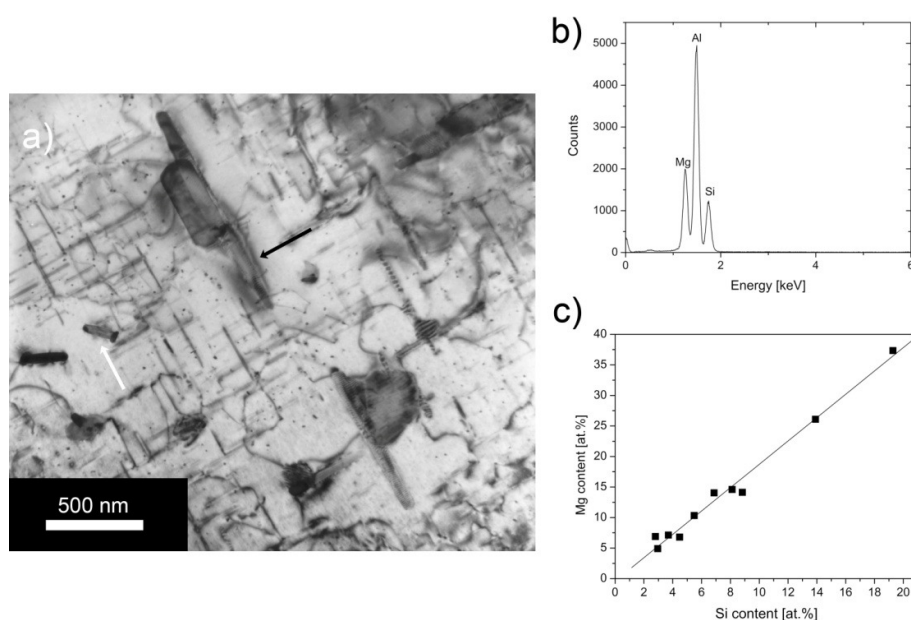
Figure 6-10 (a) TEM micrograph of an air-cooled sample naturally aged for 24 h and artificially aged for 8 h at 175ºC showing coarse non-hardening precipitates on dispersoids surrounded by precipitate free zones, (b) EDX spectrum of a non-hardening precipitate. The Mg:Si-ratio is found to be 1.95 in at.%, which equals 1.68 in wt.% (c).

Figure 6-11a shows a selected area diffraction pattern taken along the $[001]_{Al}$ direction of the Al matrix and the length of the non-hardening precipitate along the beam direction. An example of the direction is indicated by a white arrow in Figure 6-10a. This direction is the $\langle 0001 \rangle_{\beta'}$-direction of the non-hardening precipitate. Figure 6-12a shows a selected area diffraction pattern taken along the $[010]_{Al}$ direction of the matrix and the non-hardening precipitate perpendicular to their longitudinal direction (indicated by the black arrow in Figure 6-10a). This direction is the $\langle 2\text{-}1\text{-}10 \rangle_{\beta'}$-direction of the non-hardening precipitate. The lattice parameters were determined to be

a = 7.15 Å and c = 4.05 Å. It is therefore confirmed that non-hardening precipitates in alloys without excess Si are β'-phases and show a $[001]_{Al}//[0001]_{β'}$ and $(100)_{Al}//$ $(2\bar{1}\,\bar{1}0)_{β'}$-orientation relationship.

Figure 6-11b and Figure 6-12b show schematic diffraction patterns of the Al matrix and the β'-precipitate according to the crystal structure described by Vissers et al. [75], using c = 4.05 Å as opposed to c = 12.15 Å in [75], for the $[0001]_{β'}$ and the $[2\bar{1}\,\bar{1}0]_{β'}$ direction respectively. There is good agreement between the recorded patterns and the simulated patterns using the web based software package webEMAPS [116].
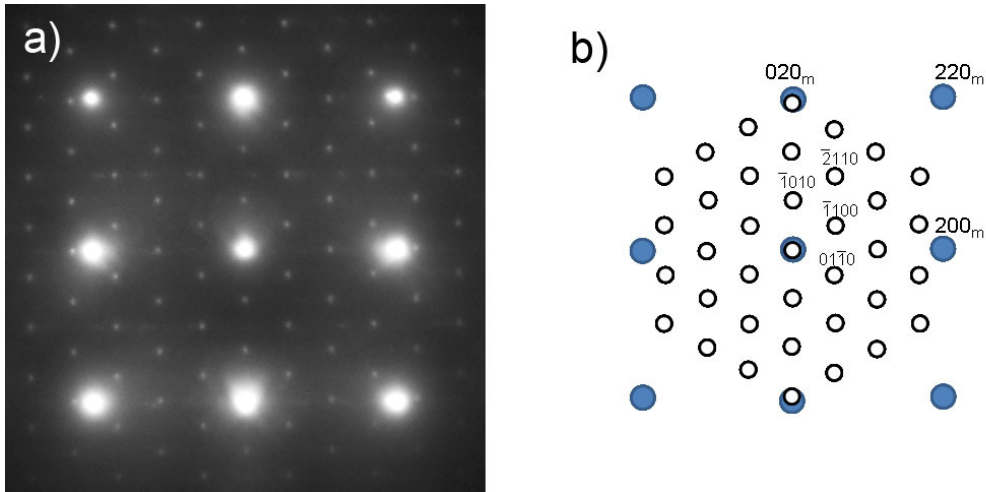
Figure 6-11 (a) SAD diffraction of a non-hardening precipitate and matrix from [0001]$_{β'}$//[001]$_{Al}$ and (b) schematic illustration of a β'-precipitate and Al-matrix. Open and closed circles indicated diffraction spots of the precipitate and matrix, respectively.
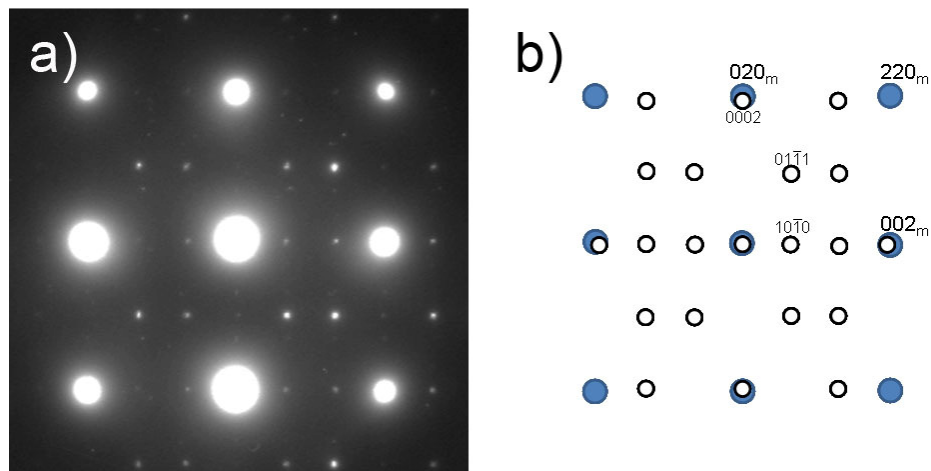
Figure 6-12 (a) SAD diffraction of a non-hardening precipitate and matrix from $\left[2\,\overline{1}\,\overline{1}\,0\right]_{\beta'}$ //[010]$_{Al}$ and (b) schematic illustration of a β'-precipitate and Al-matrix with c = 4.05 Å. Open and closed circles indicated diffraction spots of the precipitate and matrix, respectively.

6.2.3.4 Precipitation of strengthening phases

Figure 6-13 and Figure 6-14 shows the microstructure of four samples after different quenching and ageing conditions. After 30 min natural ageing and one hour artificial ageing the distribution of strengthening precipitates is very different depending on the cooling rate. While the water quenched sample (Figure 6-13a) shows very small, equi-axed precipitates, no precipitates can be resolved by conventional TEM in the air cooled sample (Figure 6-13b). This corresponds with the hardness data (Figure 6-2), where water quenched samples show significantly higher values than air cooled samples, which have not experienced a major increase in strength after one hour of artificial ageing.

After 24 h natural ageing and 8 h artificial ageing the size and number density of strengthening precipitates is very similar in both the water quenched (Figure 6-14a) and air cooled samples (Figure 6-14b). This correlates well with the hardness values, which are similar for this ageing condition (Figure 6-2c). The strengthening precipitates are elongated rods and significantly larger in size than after the short ageing treatment.
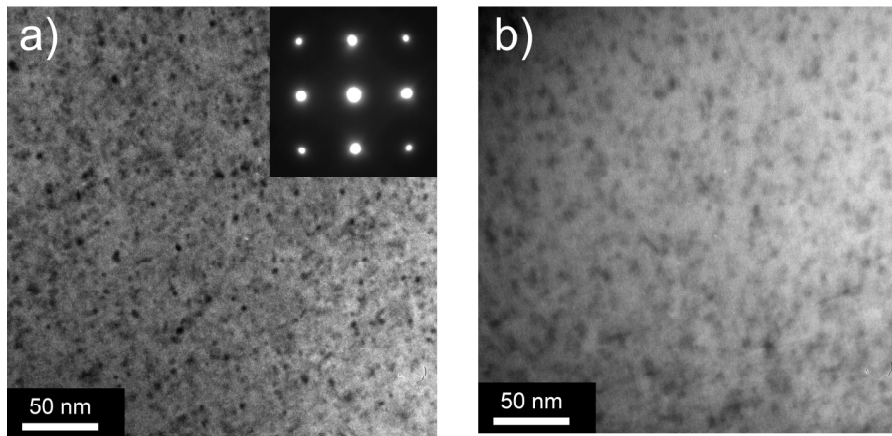
Figure 6-13 Precipitate distribution in AlMgSiMn along <001>Al. After 30 min natural ageing and 1 h artificial ageing the precipitate distribution of a WQ sample (a) varies greatly form the precipitate distribution of an AC sample (b), where no precipitates were visible under conventional TEM.
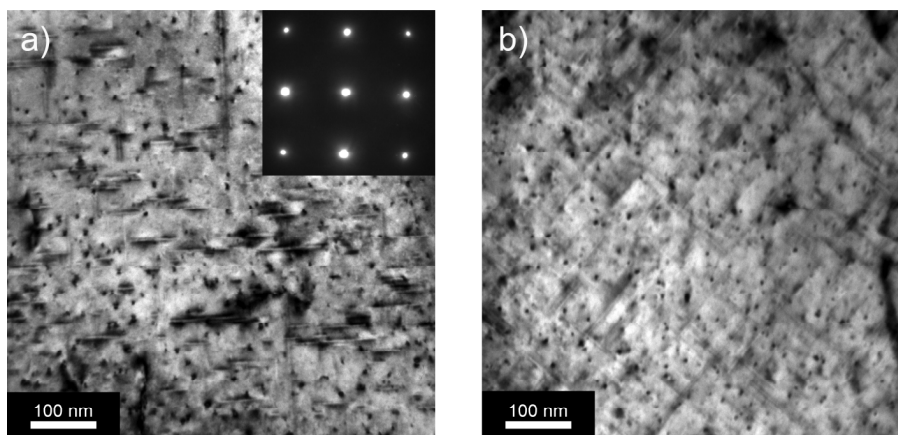
Figure 6-14 TEM micrographs along <001>Al of (a) a water quenched sample and (b) an air cooled sample after 24 h natural ageing and 8 h artificial ageing.

6.2.3.5 Precipitate free zone

The precipitation of β'-phases on dispersoids leads to the formation of precipitate free zones during natural and artificial ageing, which in contrast to the remaining matrix are solid solutions free of strengthening clusters and precipitates. This suggests that the microstructure consists of soft PFZs and hard, strengthening phase containing areas and the achievable hardness can be described by a simple composite model,

$$HV = \alpha \times HV_{ss} + (1 - \alpha) \times HV_{ppt} \qquad \text{6-1}$$

where α is the volume fraction of the PFZs, HV_{SS} the hardness of the precipitate-free solid solution and HV_{ppt} the hardness of precipitation-strengthened matrix. At a cooling rate of 50 K/min the volume fraction of the PFZ has been determined by analysing transmission electron micrographs to be about 20% ± 2%. This is a considerable amount compared to soft Al-Mg-Si alloys where, due to a very small dispersoid density the fraction of the PFZ is only about 1 % of the matrix (5.3.1.1).

6.2.4 Vacancies and clustering

In order to monitor vacancy concentration and clustering reactions during natural ageing in-situ positron lifetime spectroscopy was performed on solution treated samples quenched at different rates. The evolution of the average positron lifetime during natural ageing in the investigated alloy is presented in Figure 6-15. The initial positron lifetimes for the three alloy samples follow the same trend as for pure Al (Figure 5-10) and alloy AA6060 (Figure 5-11). The initial lifetime of the water quenched samples is highest in both materials with ~220 ps. The initially measured lifetimes of the oil quenched and air cooled samples are 215 ps and 205 ps respectively. This is significantly higher in the alloy than the initial lifetimes of the oil quenched and air cooled samples in pure Al (190 ps and 170 ps, respectively). In contrast to the pure Al samples the average positron lifetime increases in all three samples of the investigated alloy in the first minutes of the measurements, with the water quenched sample reaching a peak of ~230 ps at 20 min natural ageing and the oil quenched sample reaching a peak of ~220 ps at 30 min natural ageing. At 100 min natural ageing the water and oil quenched samples show a local minimum of 217 ps. At the same time, after a steady increase, the air cooled samples reaches the same average lifetime of 217 ps. From this point the average lifetime is independent of the cooling rate and after a slight increase reaches a local maximum of 219 ps at 300 min natural ageing and slowly decreases form there on. The average positron lifetime is very similar for all investigated samples of BA and AA6060 (Figure 5-11) after approximately 100 min natural ageing.
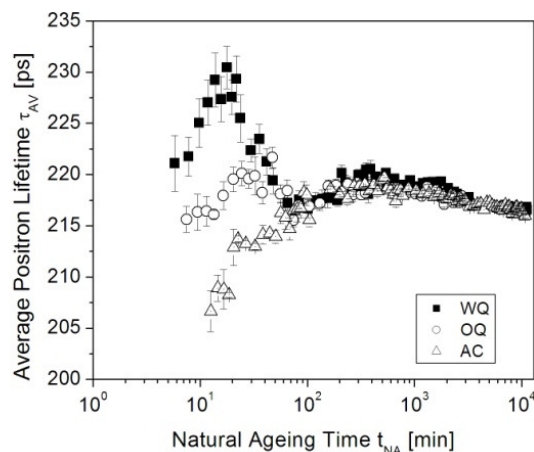
Figure 6-15 Evolution of the average positron lifetime τAV in samples of alloy BA quenched at different rates during natural ageing.

6.3 Discussion

In dispersoid containing alloys that experience significant precipitation of non-hardening precipitates on dispersoids during slow cooling and contain large amounts of Mg and Si, the separation of the effects of solute loss and the influence of non-equilibrium vacancies is rather complex. In addition to these two previously observed phenomena, changes in the precipitation sequence observed in this alloy are to be quantitatively evaluated. The following sections will therefore first attempt to quantify the single effects and then offer explanations for their interactions. The outcomes are finally summarised in a concept model.

6.3.1 Quantification of quench sensitivity

Solute loss to the precipitation of non-hardening β-Mg_2Si and β'-Mg-Si on dispersoids has long been held responsible for the reduced hardening response of samples that are cooled below the respective critical cooling rate [3, 49, 111]. It leads to unfavourable (strength-reducing) circumstances: a reduced amount of solute is available for the formation of strengthening phases and the formation of PFZs.

However, the influence of solute loss independent of the difference in the amount of mobile, non-equilibrium vacancies is difficult to determine as the number of mobile vacancies influences not only artificial ageing reactions but also clustering reactions that occur immediately after quenching at room temperature. The hardness measured during artificial ageing after prolonged natural ageing (here 24 h) therefore offers the closest approximation of hardness evolution independent of mobile vacancies, since non-equilibrium vacancies have either annihilated or are trapped in clusters. The hardness evolution after 24 h natural ageing (Figure 6-2c) shows that solute loss leads to a significant reduction in achievable hardness, especially at fixed artificial ageing times of commercial interest (< 8 h).

6.3.1.1 Quantification of Solute Loss

There is no evidence in the current results that solute loss extends past the precipitate free zone. TEM images of PFZs surrounded by regions containing a strengthening precipitates suggest a sharp border between the two regions (Figure 4-7a; Figure 5-5a and Figure 6-9). This can be further explained by the diffusion range of the strengthening phase forming solute atoms Mg and Si.

The diffusion range D is described by the Arrhenius equation

$$D = D_0 \times \exp\left(\frac{-Q}{RT}\right) \qquad \text{6-2}$$

where D_0 is the pre-exponential factor, Q the activation energy for diffusion and R the gas constant (8.314 $JK^{-1}mol^{-1}$). The diffusion range x_{dr} is determined for the temperature range between 450ºC and 250ºC according to the cooling curve recorded during slow cooling with

$$x_{dr} \propto \sqrt{Dt} \qquad \text{6-3}$$

The results are summarised in Table 6-4. At these temperatures solute atoms diffuse easily and their determined diffusion range is slightly larger than the radius determine from TEM micrographs of 188 nm ± 30 nm.

Table 6-4 Pre-exponential factor D_0 and activation energy for diffusion Q for the solute atoms Mg and Si as well as vacancies. Diffusion range x_{dr} during cooling at 50 K/min between 450 and 250ºC is determined by using the Arrhenius equation

	D_0 (m^2/s)	Q (kJ/mol)	x_{dr} (μm)
Mg	3 × 10-5 [140]	123.9 [140]	11
Si	6.3 × 10-6 [140]	113 [140]	13
Vacancy	1.1 × 10-5 [141]	125.4 [141]	5

6.3.1.2 Composite Theory

The composite theory is based on the assumption that the microstructure of slow cooled samples consists of soft, precipitate free zones and hard, precipitate-containing regions and additionally that precipitate containing regions in slow cooled samples gain the same hardness at the same rate as their fast cooled counterparts.

In order to estimate the hardness of an air cooled sample the hardness of the solid solution (HV$_{ss}$) is approximated as the hardness of a air cooled sample straight after quenching (42.9 HV) and HV$_{ppt}$ is the hardness of the corresponding water quenched sample that has experienced the same age-hardening treatment. By using the corresponding water quenched sample the hardness contribution of primary intermetallics and secondary dispersoids that should be the same in both fast and slow cooled samples is accounted for. Using Equation 1 with the above described parameters, theoretical hardness values of air cooled samples are determined. Figure 6-16 compares the measured hardness of air cooled samples to the theoretical hardness values.

After short natural ageing times (2 min and 30 min) the hardness measured for air cooled is significantly lower than the hardness that would be expected if artificial ageing kinetics are the same as in the corresponding water quenched sample. The difference between the measured and the theoretical values is more pronounced during short artificial ageing times and reduced (30 min natural ageing) or become negligible (24 h natural ageing) during long artificial ageing times. After long natural ageing times the measured hardness and the hardness determined according to the composite theory is nearly identical.
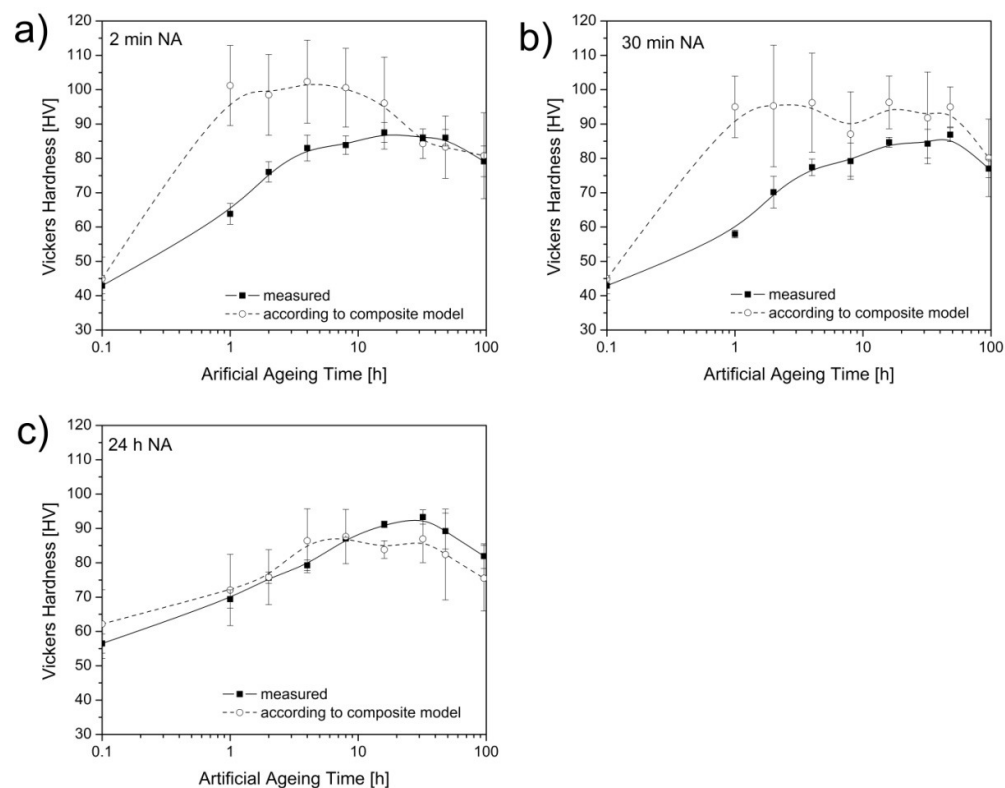
Figure 6-16 Comparison between the measured hardness and a theoretical hardness according to the composite model of air cooled samples after a) 2 min, b) 30 min and c) 24 h natural ageing.

These comparisons demonstrate that after long natural ageing times the hardness of the air cooled sample can be described using the composite model and that therefore the artificial ageing kinetics of both the water quenched and air cooled samples are the same. After short natural ageing times however, the hardness of the air cooled samples cannot be described using the composite model. This indicates that the artificial ageing kinetics are significantly different between the water quenched and air

cooled samples. As a result, solute loss in general, but also the more refined description of solute loss leading to the formation of PFZs, is not sufficient to accurately describe the effect of cooling rate on artificial ageing behaviour in Al-Mg-Si alloys.

6.3.1.3 The role of natural ageing

In contrast to low strength Al-Mg-Si alloys with combined Mg and Si contents below 1 wt.% where natural ageing has a positive effect on the artificial ageing response (Chapter 5), the alloy investigated in this section reacts negatively to natural ageing. This negative effect has been widely described in literature [43, 81, 90, 129], where studies mainly investigated the natural ageing response in fast cooled samples. In fast cooled samples the negative effect of natural ageing has been attributed to the annihilation and trapping of mobile, non-equilibrium vacancies [43] and solute loss to stable clusters, which do not act as nucleation sites for the precipitation of strengthening phases [81, 90, 129]. Little work has been conducted on samples that had been cooled at slow rates [142] so it is of great interest whether the two negative effects, slow cooling rate and natural ageing, add up to cause a strong negative effect or whether there are dependent processes that lead to a reduction in the negative effect.

The current results demonstrate that in air cooled samples a slightly higher peak hardness of 93 ± 2 HV is reached after long natural ageing times (here 24 h) compared to short natural ageing times (<30 min), where the peak hardness is 88 ± 3 HV. The hardness after artificial ageing of samples without natural ageing appears to be the result of a moderate hardness increase during artificial ageing, whereas for samples naturally aged for 24 h it is the result of a significant hardness increase during natural ageing and a small increase during artificial ageing. For the investigated natural ageing times the achieved hardness after artificial ageing is almost independent of natural ageing time.

Whether quench sensitivity or the negative effect of natural ageing is more detrimental to the alloys age-hardening cannot be easily answered. There are a

number of simultaneously occurring processes that influence age hardening. These processes are discussed in the following sections.

6.3.2 Explanation for Quench Sensitivity

The following sections give explanations for quench sensitivity in a dispersoid containing alloy. The role of solute loss is discussed, followed by the role of natural ageing. The result of both these effects on artificial ageing is included in the discussion. The outcomes are summarised and presented in a concept model.

6.3.2.1 Effect of solute loss

Microstructural observations of precipitate free zones (Figure 6-9a) suggest that solute loss is not uniform but rather concentrated in distinct zones around dispersoids and non-hardening precipitates [23, 38]. This has been previously described by Deschamps et al. [38]. Solute that forms the non-hardening precipitate is sourced from a limited volume and therefore leads to a limited zone depleted of solute, which during artificial ageing becomes the precipitate free zone. The remaining matrix is unaffected. This disproves the more popular view that solute is lost evenly and the reduced amount of solute leads to a reduction in driving force for precipitation. Models based on the assumption, that solute is lost evenly [21, 26, 55] offer high accuracy and predict quench sensitivity well. However, this is because these models are calibrated using experimental data. Hence, their accuracy does not offer an indication for the validity of the underlying assumption.

6.3.2.2 Effect of natural ageing

The instability of the solid solution leading to clustering during room temperature storage in 6xxx series alloys is well known [22, 85, 90, 143]. Simultaneously, quenched-in vacancies annihilate or get trapped in the forming clusters. How these processes differ depending on the cooling rate after solution treatment or extrusion is discussed in the following paragraphs.

The initial positron lifetime is related to the concentration of quench-induced vacancies and varies greatly for water quenched, oil quenched and air cooled samples. Since mobile, non-equilibrium vacancies determine diffusion controlled processes and hence clustering and precipitation reactions, the formation of early clusters occurs faster for fast quenched samples compared to air cooled samples. This is reflected in the faster hardness increase during natural ageing in water and oil quenched samples (Figure 6-1) and the early exothermic reaction in the water quenched sample during DSC scans after 30 min natural ageing (Figure 6-5a). The water quenched sample shows a significant peak A compared to the air cooled sample where no clustering peak is observed.

The initial average positron lifetime τ_{AV} of the water quenched sample of alloy BA measured about 3-6 minutes after the quench is at ~221 ps slightly lower than initial lifetimes reported in literature, which are ~245 ps for a lean Fe free alloy [96] , ~ 230 ps for the commercial alloy AA6060 (Figure 5-11), 227 ± 4 for a Fe and high Si-containing Al-Mg-Si alloy [135] and ~224 ps for a Fe-free alloy with similar Mg and Si content [96]. Although Banhart et al. [96] measured a similar initial lifetime to the 221 ps that were measured in the present study, all of the mentioned curves experience an initial decrease compared to the water quenched sample in this study that shows a lower initial lifetime followed by an increase in τ_{AV} for the first 30 min. The lower initial lifetime might be characteristic for alloys containing high Mg and possibly Si contents or the result of early vacancy annihilation on heterogeneous interfaces, mainly between matrix and dispersoids.

The early peak (~20 – 30min) in average positron lifetime is observed in both the water and the oil quenched sample and might be related to early clustering reactions which have been described by Chang et al. [90] to occur during the early stages of natural ageing. A similar increase is observed in the oil quenched sample of alloy AA6060 and has been also related to clustering (Figure 5-11). It is difficult to determine the nature of the cluster and whether it traps vacancies or not. Banhart et al. interpreted a decrease in lifetime in the early stages of natural ageing with the formation of vacancy free clusters [96], which were proposed to have a lower lifetime of ~200 ps. The initial

increase observed in this study therefore leads to the conclusion that early clusters contain vacancies and hence act as vacancy traps which lower the concentration of mobile vacancies.

At 100 min natural ageing from where all three samples show a very similar average lifetime and follow the same trend, the water and oil quenched samples have experienced a peak, which is related to clustering, whereas the average positron lifetime of the air cooled sample has increased steadily. The lack of an early lifetime peak in combination with the lack of a clustering peak in the DSC scan after 30 min natural ageing (Figure 6-5a) indicate that clustering occurs to a lesser degree in air cooled samples.

However, that extensive clustering occurs within the first 24 h of natural ageing is evident from the significant increase in hardness during natural ageing (Figure 6-1) and from the DSC scans of naturally aged samples (Figure 6-5b). Peak A, attributed to cluster formation in the water quenched sample, is much reduced compared to the sample naturally aged from the DSC for 30 min (Figure 6-5a) and not observed in the air cooled samples. The endothermic peak B for cluster dissolution is observed in both samples that were naturally aged for 24 h, with the peak in the water quenched sample being larger than in the sample naturally aged for 30 min (Figure 6-5). The decrease in peak A while peak B is similar in size shows firstly that a large amount of clusters have formed in both samples (more in the water quenched) and secondly that the clustering rate after 24 h natural ageing is reduced significantly compared to 30 min natural ageing.

The distinct differences that characterise the microstructure of an as-quenched sample compared to a sample aged for 24 h are a reduced number of mobile, non-equilibrium vacancies (as a result of vacancy annihilation during natural ageing and clustering), resulting in the trapping of vacancies as well as solute loss. These differences are more pronounced in fast cooled samples compared to air cooled samples.

6.3.2.3 Effect of artificial ageing

A high artificial ageing response is achieved when the alloy contains a homogeneously distributed, highly supersaturated solid solution in addition to a high concentration of mobile non-equilibrium vacancies. In this study the water quenched sample after 2 min natural ageing is closest to this condition and reaches the highest peak hardness after short natural ageing times (Figure 6-2a).

It has been demonstrated in the previous sections that both a reduced cooling rate as well as natural ageing affect various alloy parameters and therefore reduce the artificial ageing response. A reduced quench rate leads to non-uniform solute loss, and hence PFZs are found plus a reduced concentration of quenched-in vacancies. Natural ageing leads to further solute loss due to the formation of stable clusters and vacancy loss, due to trapping in clusters and annihilation.

The negative effect of natural ageing is apparent in water and oil quenched samples after 24 h natural ageing (Figure 6-1). Cluster formation and vacancy annihilation cause an increase in the activation energy for β''-precipitation (Table 6-3) which in turn leads to reduced peak hardness as well as the prolonged artificial ageing time to peak hardness (Figure 6-2c).

In air cooled samples prolonged natural ageing does not lead to reduced hardness after artificial ageing. Although the increase in hardness is less after 24 h natural ageing compared to 2 min and 30 min, the overall hardness is increased. Due to the low concentration of mobile, non-equilibrium vacancies directly after quenching, artificial ageing kinetics are slow independent of the natural ageing time and therefore unaffected by annihilation of non-equilibrium vacancies. Simulations of vacancy concentration depending on the cooling rate show that the vacancy concentration after air cooling (~50-100 K/min) is below that of the equilibrium concentration at artificial ageing temperature, so that precipitation kinetics are determined by thermal activation [39, 43, 48].

PALS measurements of the air cooled sample do not show a peak within the first hour of natural ageing, but rather a steady increase that leads to a peak at about 300 min natural ageing, at which time water and oil quenched samples have their second peak. The increased hardness after 24 h natural ageing may be the result of clusters adding to the final hardness, promoting the precipitation of more potent strengthening phases [98] or slowly dissolving during artificial ageing to release additional solute [89], similar to the mechanisms that have been proposed to be responsible for the positive effect of natural ageing in lean Al-Mg-Si alloys [89, 98].

The reduced hardness response might also be affected by the type of precipitates that form during artificial ageing. The major strengthening phase β" is unstable and forms as part of a precipitation sequence from GP-zones and evolves into meta-stable precipitates β', B', Type A and Type B [11, 76]. DSC scans give an indication of the relative dominance of the single phases (Figure 6-5) as the peak area (formation enthalpy ΔH) relates to the magnitude of the reaction which can be related to the volume fraction of the formed precipitates. While DSC curves of water quenched samples show two distinct peaks for the formation of β" and β', with the peak for β"-precipitation being significantly larger than the peak for β'-formation, these two peaks are melded together in the air cooled samples (Table 6-2). De-convolution of these peaks in the air-cooled sample shows that while the area of the peak for β'-formation is about the same as in water quenched samples, the peak area for β"-formation is significantly smaller. This indicates that the formation of the strengthening β"-precipitates is suppressed at low cooling rates. Although the microstructure in Figure 6-14b is taken after 24 h NA and 8 h artificial ageing, before peak hardness is reached, precipitates are long, elongated rods, which indicate β'. This suggests that the microstructure of air cooled samples at their peak hardness consists of the meta-stable β'-precipitates are generally less effective in strengthening than their pre-cursor β".

The suppression of β"-formation and hence a change in precipitation sequence is possibly due to solute and/or vacancy loss, but it contributes further to the reduced strength and hardness achieved in air cooled samples compared to water quenched samples.

6.3.2.4 Concept model

The results presented in this chapter show that there are a number of effects that influence quench sensitivity. These are primarily the loss of solute during slow cooling from extrusion or solution treatment temperature and a reduced number of mobile, non-equilibrium vacancies as the result of slow cooling. The loss of solute is significant in medium to high strength alloys due to the relatively high number density of secondary dispersoids.

Figure 6-17 shows a schematic of processes involved in quench sensitivity in dispersoid containing Al-Mg-Si alloys. While large amounts of solute and vacancies remain in solid solution after fast cooling, heterogeneous nucleation of β'-phases and a vacancy concentration closer to the equilibrium concentration at room temperature are the result of cooling in still air. Immediate artificial ageing results in a rapid response and high hardness in water quenched samples and a slow response and low hardness in air cooled samples. This difference in ageing response is mainly determined by the difference in the amount of mobile vacancies. When samples are stored at room temperature directly after quenching vacancy annihilation and clustering occurs. Analogous to artificial ageing, the clustering rate is dependent on the concentration of mobile vacancies as well. Therefore, a larger number of clusters form in water quenched samples compared to air cooled samples.

Room temperature clustering has a negative effect on the artificial ageing response and together with the reduced amount of mobile vacancies the artificial ageing response in water quenched samples is strongly reduced after 24h NA. Although the artificial ageing response, i.e. the hardness increase of air cooled samples is also reduced, the peak hardness is higher after 24 h NA compared to 30 min NA. This appears to be due to a hardening contribution of clusters formed during natural ageing.
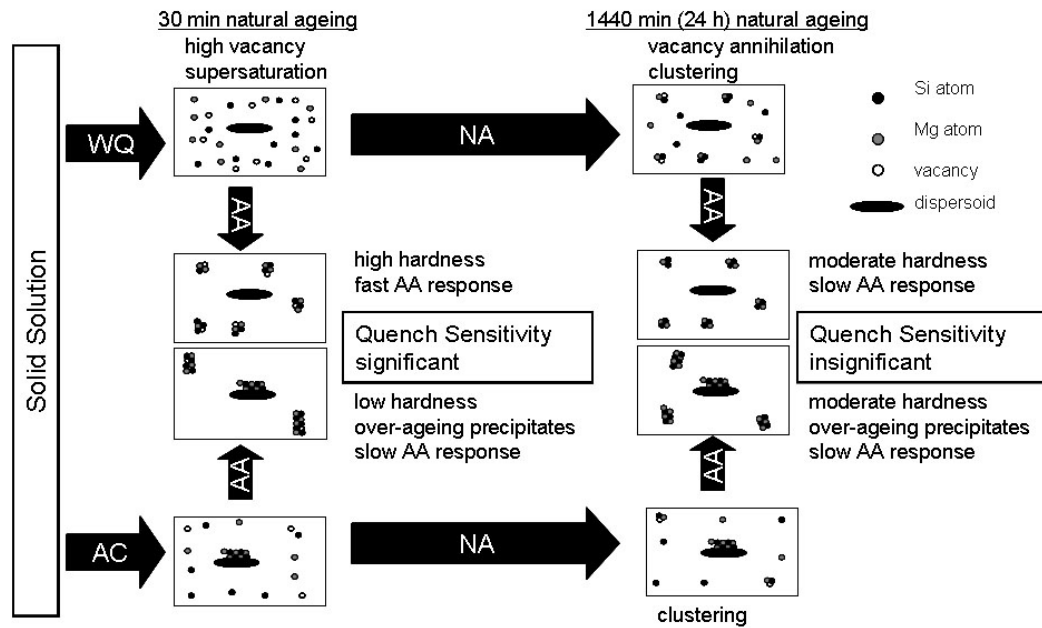
Figure 6-17 Schematic visualisation shows the effects of cooling rate and natural ageing time on age-hardening behaviour in dispersoid containing alloys with combined Mg+Si contents greater than 1 wt.%. The artificial ageing response is compared after different quench rates (water quenched and air cooled) and for short and long natural ageing times (30 min and 24 h). The indicated microstructures are hypothetical and have not been verified experimentally.

The clustering rate during natural ageing appears to be therefore dependent on the cooling rate after solution treatment temperature. Air cooled samples experience limited clustering and limited vacancy annihilation, while both these processes are significant in water quenched samples. The artificial ageing response (here: increase in hardness) after long natural ageing times is therefore reduced – by a small amount for air cooled samples and a large amount for water quenched samples. As a result, air cooled samples experience a slightly positive effect from natural ageing, while water quenched samples experience a large negative effect.

Comparing the artificial ageing response after 24 h, where mobile vacancies have negligible influence on the artificial ageing response after very short natural ageing times (here 2 min), it becomes obvious that the difference in mobile, non-equilibrium vacancies, which affects artificial ageing kinetics, is more significant than that of solute loss. The amount of mobile vacancies not only affects the artificial ageing response, but also the natural ageing response. The clustering rate appears to be greatly enhanced in the presence of mobile vacancies.

In addition, the formation of the major strengthening phase β" appears to be inhibited in slow cooled samples. Therefore, slow cooled samples seem to show mainly the coarser, meta-stable β'-phase at their respective peak hardness. The strengthening contribution of the meta-stable phase is lower than of β"-precipitates adding to the reduction in peak hardness.

From a practical point of view the balance between quench sensitivity and the negative effect of natural ageing has to be considered. Where prolonged natural ageing times cannot be avoided, the improvement gained by quenching in water is significantly reduced.

6.4 Conclusions

In contrast to the lean AA6060, which contains few dispersoids, quench sensitivity in Al-Mg-Si alloys with a high dispersoid content is significantly influenced by solute loss. Although solute loss is limited to a precipitate free zone around dispersoids and the attached β'-Mg-Si non-hardening precipitates, precipitation kinetics in the supersaturated regions is affected by slow cooling rates. A lower concentration of quenched-in vacancies after slow cooling results in a lower number of point defects that act as nucleation sites for clusters or precipitates and a reduced diffusion rate. As both driving force for and kinetics of clustering and precipitation are affected by the cooling rate it was important to investigate the age-hardening behaviour after cooling at different rates. While fast quenched samples experience the well described negative effect of natural ageing significantly, slow cooled samples reach higher hardness values after prolonged natural ageing. As a result, quench sensitivity is not only dependent on the cooling rate but also changes with natural ageing, due to the varying response to room temperature storage of fast and slow cooled samples.

Chapter 7   Influence of Excess Si and Cu on Quench Sensitivity

7.1 Introduction

In this chapter the influence of the strengthening phase forming elements Mg, Si and Cu on quench sensitivity in dispersoid containing alloys is investigated. The alloys are designed to have the same dispersoid density as this has been found to have a major effect on quench sensitivity (Chapter 4). The strengthening phase forming elements are expected to affect quench sensitivity in the two previously identified key areas, solute loss and age-hardening response. Therefore, firstly, the effect of alloy composition on the amount and composition of non-hardening precipitates is determined. Secondly, the investigation attempts to rationalise the effects of alloy composition and quench rate on natural and artificial ageing behaviour. As reports in literature [65, 81, 99, 107] suggest that the natural ageing effect is affected by the alloy composition and, which was found in Chapter 6 to be cooling rate dependent, this relationship is of particular interest.

7.2 Results

In order to compare the effect of the strengthening phase forming elements Mg, Si and Cu on quench sensitivity, their artificial ageing response at 175ºC was determined after 30 min and 24 h natural ageing. Three alloys (Table 3-2) were chosen to compare the influence of the strengthening phase forming elements Mg, Si and Cu on quench sensitivity. A high Si content as well as Cu additions have been previously found to increase strength [65, 144, 145]. In order to avoid the influence of a varying dispersoid density the same Mn and Fe contents were chosen.

Table 7-1 Composition (in wt.%) of the model alloys investigated in Chapters 6&7.

	Si	Mg	Mn	Fe	Cu	Al
Base Alloy (BA)	0.67	0.84	0.35	0.25	-	bal.
High Si (HS)	0.85	0.59	0.39	0.25	-	bal.
Base Alloy + Cu (BA+Cu)	0.69	0.82	0.34	0.29	0.22	bal.

The observed similarities and differences are then explained by quantifying dispersoid density and the amount of solute lost to non-hardening precipitates and determining their composition and crystal structure.

7.2.1 Hardening response

The age hardening response of the three different alloys after 30 min and 24 h natural ageing is shown in Figure 7-1, with key features summarised in Table 7-2. For all alloys the maximum hardness is reached when samples are water quenched and natural ageing times are short (here 30 min).These peak values were reached after short artificial ageing times (1-8 h). The artificial ageing responses of air cooled samples after 30 min NA are significantly slower than that of the water quenched samples and reach a lower peak hardness of about 85 HV for the Cu-free alloys and 92 HV for the Cu-containing alloy (see Table 7-2).

The hardening response is characterised by several parameters: the peak hardness, the artificial ageing time to peak hardness and the hardness increase for the hardness after natural ageing to peak hardness. The peak hardness, particularly after water quenching and short natural ageing, shows an alloy's hardening ability and is determined by the content of strengthening phase forming elements. The time to peak hardness relates to artificial ageing kinetics and is influenced by the number of precipitation sites and the mobility of solute. The hardness increase during artificial ageing is itself influenced by a number of things: there is the amount and mobility of solute in solid solution as well as the number of precipitation sites.
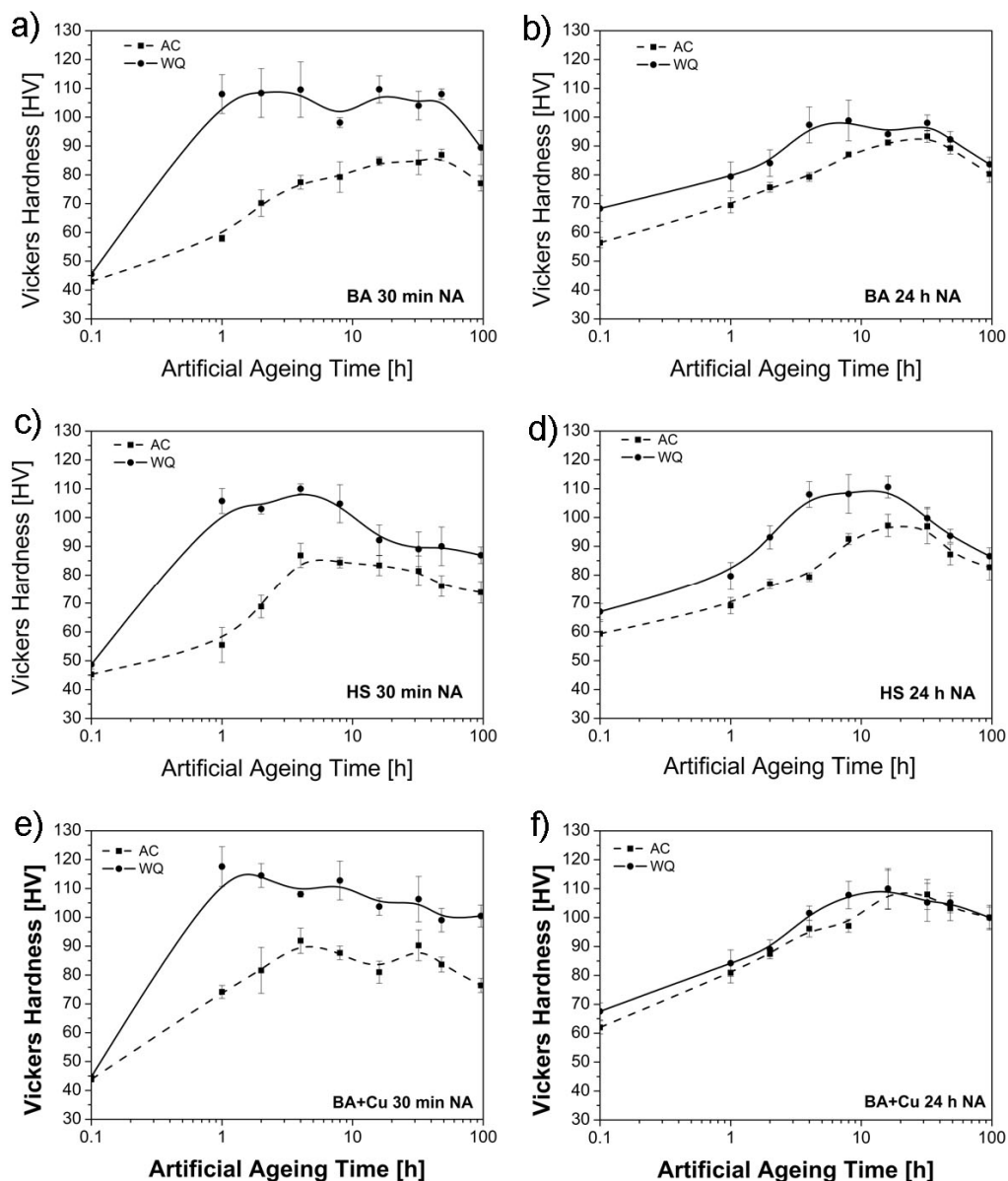
Figure 7-1 Artificial ageing response of alloys BA, HS and BA+Cu after 30 min and 24 h natural ageing (a) BA 30 min NA, (b) BA 24 h NA, (c) HS 30 min NA, (d) HS 24 h NA, (e) BA+Cu 30 min NA and (f) BA+Cu 24 h NA.

The Cu-containing alloy generally reaches the highest hardness, confirming that Cu-additions lead to increased hardness. Although it would be expected that the relatively high Si content in HS leads to increased hardness compared to BA, it is not observed in water quenched samples after 30 min natural ageing, but only in water quenched samples after 24 h natural ageing. The increased negative effect of excess Si, as described by Murayama et al. [99], is not observed here. The time to peak hardness is shortest in water quenched samples after short natural ageing times, where the solute

supersaturation is high and a high number of mobile, non-equilibrium vacancies guarantee solute mobility. A lack of mobile, non-equilibrium vacancies causes a delay in artificial ageing response and hence longer times to peak hardness as experienced by air cooled samples and water quenched samples after 24 h natural ageing. Differences attributed to the alloy composition can be observed in air cooled samples after short natural ageing times where alloys HS and BA+Cu show a significantly shorter time to peak hardness with 4 h compared to 16 – 48 h in alloy BA.

Table 7-2 Key features of the age hardening response.

Alloy–quench	Peak Hardness (HV)/time (h)				Increase in hardness to peak hardness (HV)	
	NA time					
	30 min		24 h		30 min	24 h
BA - WQ	110	1-16 h	100	4-8 h	65 ± 10	30 ± 10
BA - AC	88	16-48 h	93	16-32 h	45 ± 4	37 ± 4
HS - WQ	110	1-8 h	110	4-16 h	60 ± 7	44 ± 6
HS- AC	87	4 h	97	16-32 h	42 ± 3	38 ± 6
BA+Cu - WQ	118	1-8 h	110	8 h	70 ± 9	56 ± 7
BA+Cu - AC	92	4 h	110	16-32 h	58 ± 7	57 ± 8

The hardness increase is largest in water quenched samples after 30 min natural ageing, due to a high amount and high mobility of solute in solution. This has also been observed in Chapters 5 & 6. The difference between the hardness increase between water quenched and air cooled samples is much more significant after 30 min natural ageing than it is after 24 h, indicating that the negative effect of natural ageing is more significant in water quenched samples than in air cooled samples. The reduction in hardness increase is also more severe in alloy BA than it is in alloys HS and BA+Cu. This is a further indication of increased ageing kinetics in the presence of a high Si content and Cu-additions under conditions where the concentration of mobile vacancies is low.

It should be noted that after 24 h natural ageing the air cooled sample of the Cu-containing alloy reaches the same peak hardness (110 HV), although it is delayed. This suggests that solute loss and the age hardening behaviour are both reasons for quench sensitivity as has been found in the previous chapters.

7.2.2 Thermal analysis

Differential scanning calorimetry is performed during cooling at different rates after solution treatment for 2 h at 550ºC. All alloys indicate at least two different reactions occurring at low cooling rates between 5 – 30 K/min, which have been attributed to the precipitation of equilibrium phases like Mg_2Si and (Si) (high temperature reaction) and the precipitation of meta-stable phases (low temperature reaction). With increasing cooling rates the high temperature reaction moves to lower temperatures and decreases in size. At a cooling rate of 150 K/min there is still precipitation detected and hence solute is being lost. This means, the critical cooling rate to avoid precipitation is higher than 150 K/min for all three investigated alloys.

In order to quantify the solute loss during cooling, DSC measurements were performed at 50 K/min. All three alloys experience significant precipitation and hence solute loss during cooling from the solution treatment temperature. Figure 7-3 shows exothermic reactions occurring during cooling. The combined formation enthalpies of both the high and low temperature reaction were determined as 5.3 J/g for alloy BA, 5.9 J/g for alloy HS and for 5.8 J/g for alloy BA+Cu. Figure 7-4 separates the formation enthalpy for the low and high temperature reaction.
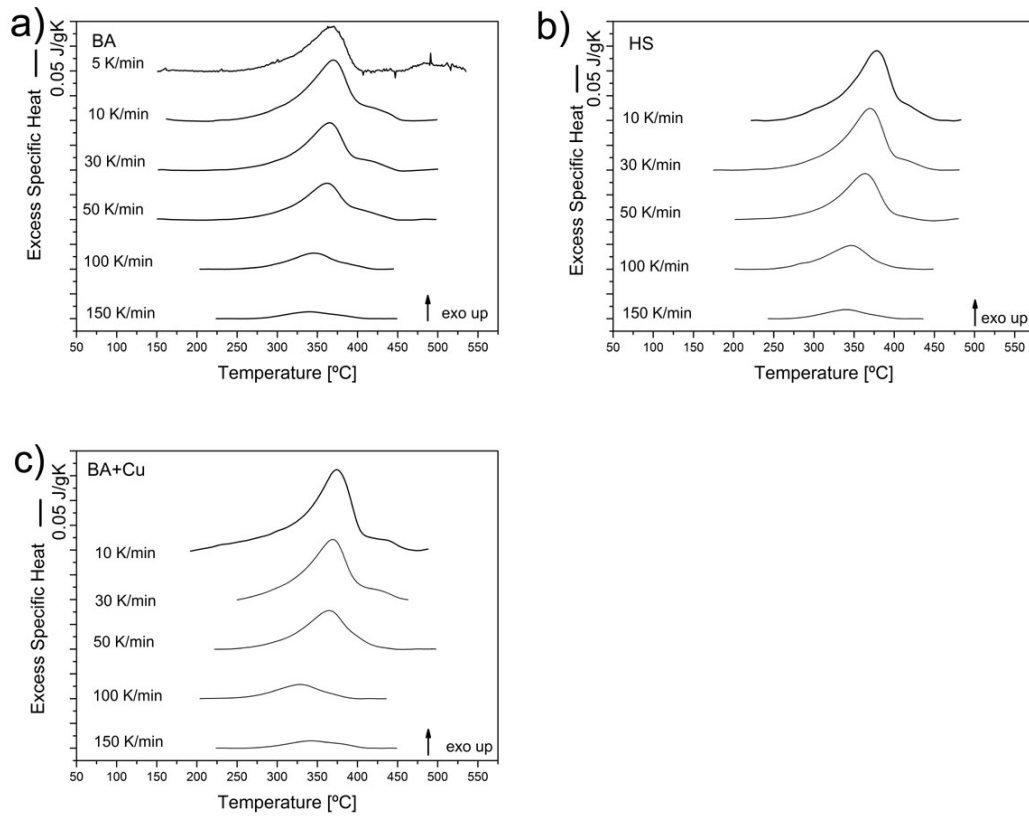
Figure 7-2 Precipitation reactions during cooling after solution treatment monitored by DSC in (a) BA, (b) HS and c) BA+Cu.
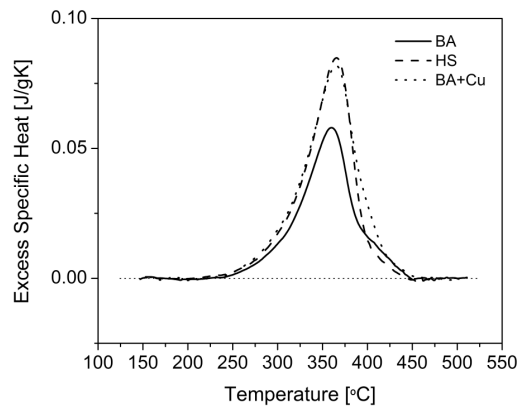
Figure 7-3 Typical DSC curves of the exothermic precipitation reactions of non-hardening phases during cooling at 50 K/min.
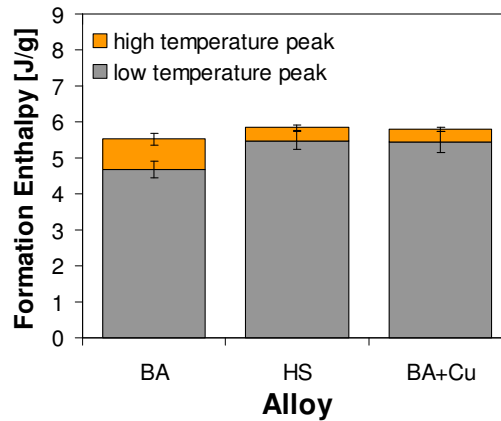
Figure 7-4 Formation enthalpy of non-hardening precipitates divided into the formation of metastable phases in the low temperature reaction and equilibrium phases in the high temperature reaction in the three investigated alloys.

7.2.3 Microstructure characterisation

The microstructure of the three different alloys has been investigated on two different levels. In order to quantify quench sensitivity the dispersoid density has been determined by image analysis of back scattered electron micrographs. Secondly, to clarify the influence of high relative Si contents and Cu-additions the crystal structure and composition of non-hardening precipitates is investigated using TEM.

7.2.3.1 Microstructure after homogenisation

After homogenisation all three investigated alloys show an even distribution of secondary dispersoids throughout the matrix (Figure 7-5). As the material has not been deformed the dispersoids do not show a strong orientation in any direction, compared to the extruded commercial alloys investigated in Chapter 4.
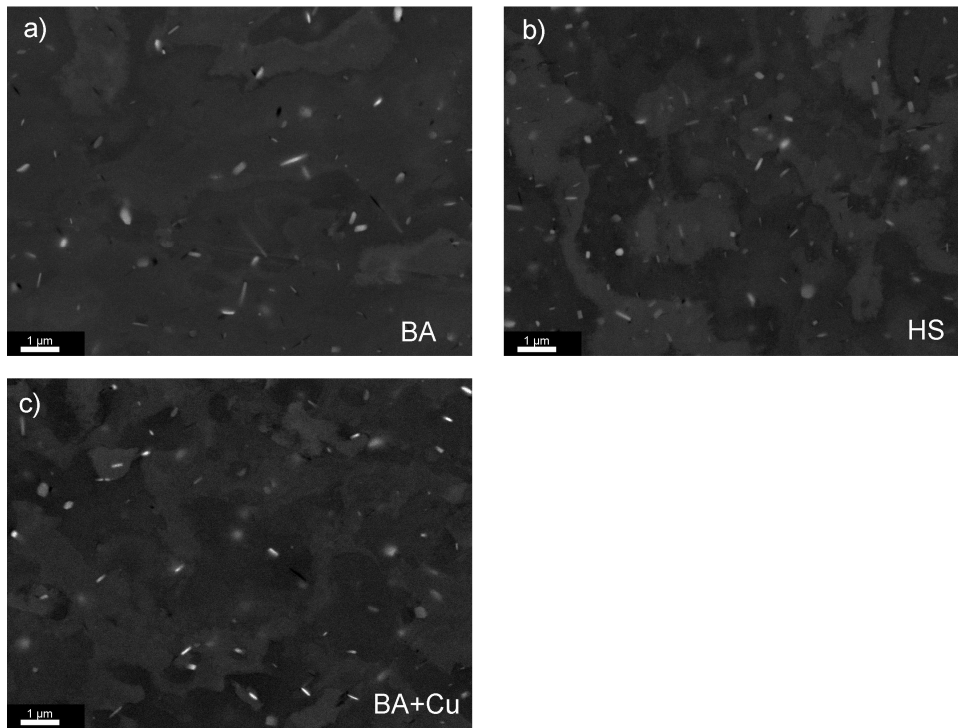
Figure 7-5 Dispersoid distribution in the three investigated alloys BA (a), HS (b) and BA+Cu (c).

The Fe- and Mn content in the model alloys was chosen to produce a very similar dispersoid distribution to exclude the varying dispersoid number density as an influence on quench sensitivity. Detailed image analysis showed that the differences in number density are small (Figure 7-6).
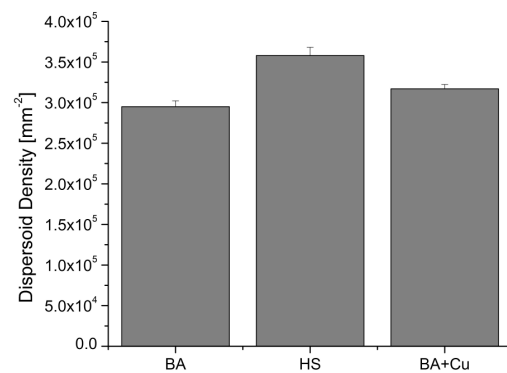
Figure 7-6 **Number density of dispersoids in the three investigated model alloys.**

7.2.3.2 Microstructure after slow cooling

In order to investigate whether the low Mg/Si ratio or the addition of Cu has an influence on the type, i.e. crystal structure and composition of non-hardening precipitate forming, TEM investigations were conducted. The Mg:Si-ratios of the non-hardening precipitates were determined using EDX (Figure 7-7). Figure 7-8 shows the microstructure of an air cooled sample of alloy HS. The microstructure shows, similar to the microstructure of the air cooled sample of alloy BA (Figure 6-9a), shows coarse, lath-shaped Mg-Si-containing precipitates that have formed on dispersoids and are surrounded by densely distributed strengthening precipitates. Compared to the non-hardening precipitates that have formed in alloy BA, which contain a Mg:Si-ratio of about 1.68 ± 0.15 (in wt.%), the non-hardening precipitates formed in HS contain a lower Mg:Si-ratio of about 1.55 ± 0.2(in wt.%) (Figure 7-7, Figure 7-7b).
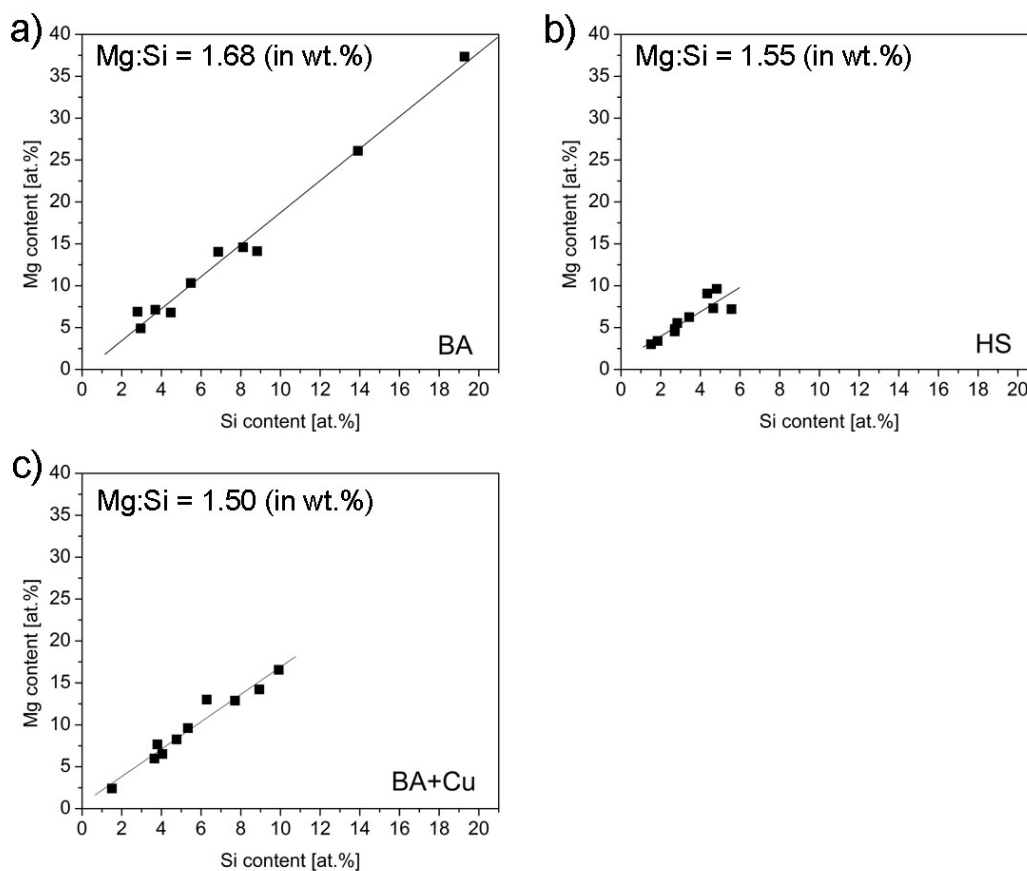
Figure 7-7 Mg to Si ratio of non-hardening precipitates in (a) BA, (b) HS and (c) Ba+Cu.
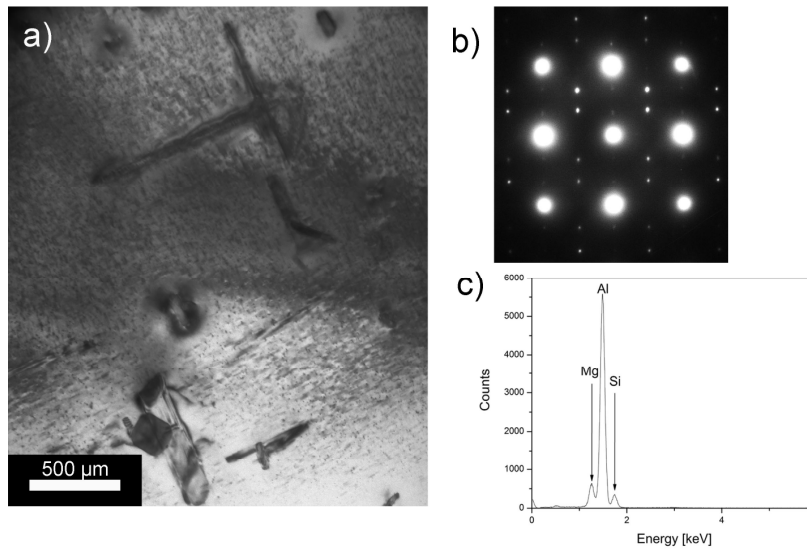
Figure 7-8 TEM micrograph of dispersoids with attached non-hardening precipitates (ppt) in HS (a), (b) SAD pattern along $\left[2\,\overline{1}\,\overline{1}\,0\right]_{ppt}$//[001]$_{Al}$ of Al-matrix and the non-hardening precipitate and (c) EDX spectrum of non-hardening precipitate.

Figure 7-9 shows a high resolution bright field TEM micrograph taken on a JEOL F20 FEG-TEM of a non-hardening precipitate that has formed on a dispersoid. The micrograph is taken along a [001]$_{Al}$ direction of the matrix and along the <0001>$_{\beta'}$ direction of the non-hardening precipitate.
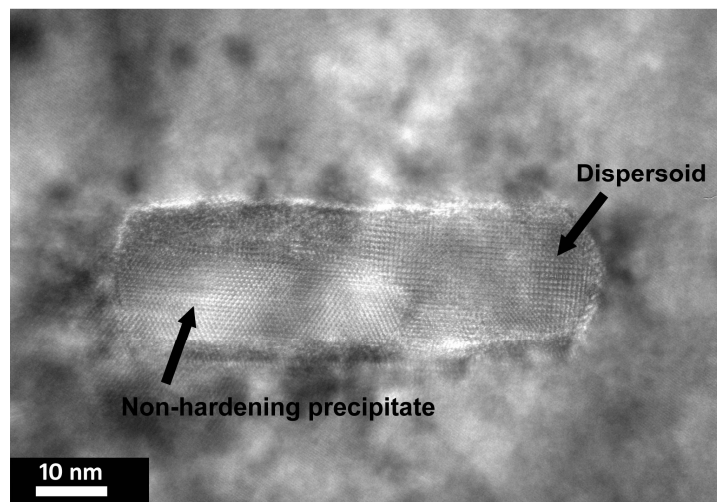
Figure 7-9 High resolution bright field TEM micrograph along an [001]$_{Al}$ direction of the matrix and the <0001> direction of the non-hardening precipitate showing a hexagonal non-hardening phase that has precipitated on the cubic dispersoid.

Figure 7-10a shows a close up of the non-hardening precipitate and the matrix in Figure 7-9. Figure 7-10b is the FFT of the interface between matrix and dispersoid and shows that non-hardening precipitates that precipitated during cooling at 50 k/min in

alloy HS has the same lattice parameter of $a = 7.15$ Å and $c = 4.05$ Å as the non-hardening precipitates that precipitated under the same conditions in alloy BA. This is supported by the SAD pattern along a $[001]_{Al}$ direction and the $\langle 2\bar{1}\,\bar{1}0\rangle_{\beta'}$-direction of the precipitate (Figure 7-8b).
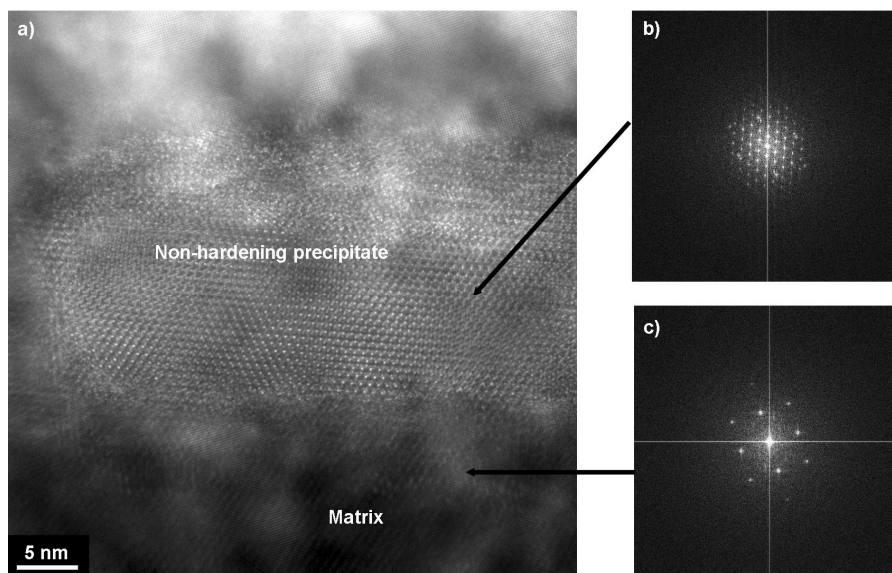
Figure 7-10 (a) High resolution bright field TEM micrograph of a section of Figure 7-9 with FFTs of (b) the hexagonal non-hardening precipitate along <0001>$_{\beta'}$ and (c) the cubic matrix along [001]$_{Al}$.

The microstructure of BA+Cu (Figure 7-11) is similar to the microstructures of the other two investigated alloys BA and HS. Although the precipitates contain Cu in addition to Mg, Si and potentially Al, their Mg:Si-ratio at 1.5 ± 0.17 (wt.%) shows no significant difference to the Mg:Si-ratio of non-hardening precipitates in the alloys BA and HS. They also have the same lattice parameters. The solute content therefore appears to have no significant influence on the phase precipitating during slow cooling.

Figure 7-12a shows a high resolution bright field TEM micrograph of a triple pint between matrix, dispersoid and non-hardening precipitate along a $[001]_{Al}$ direction and the <0001>$_{\beta'}$ direction of the precipitate. The FFTs of the matrix (Figure 7-12a) and the non-hardening precipitate (Figure 7-12c) show that the precipitate is rotated around the c-axis by 30º.
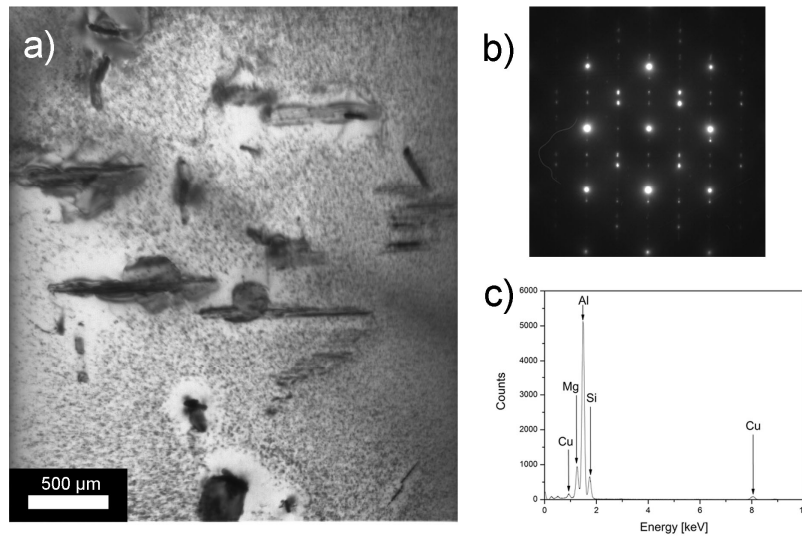
Figure 7-11 TEM micrograph of dispersoids with attached non-hardening precipitates in BA+Cu (a), (b) SAD pattern along $\left[2\bar{1}\,\bar{1}0\right]_{ppt}$//[001]$_{Al}$ of Al-matrix and the non-hardening precipitate and (c) EDX spectrum of non-hardening precipitate.
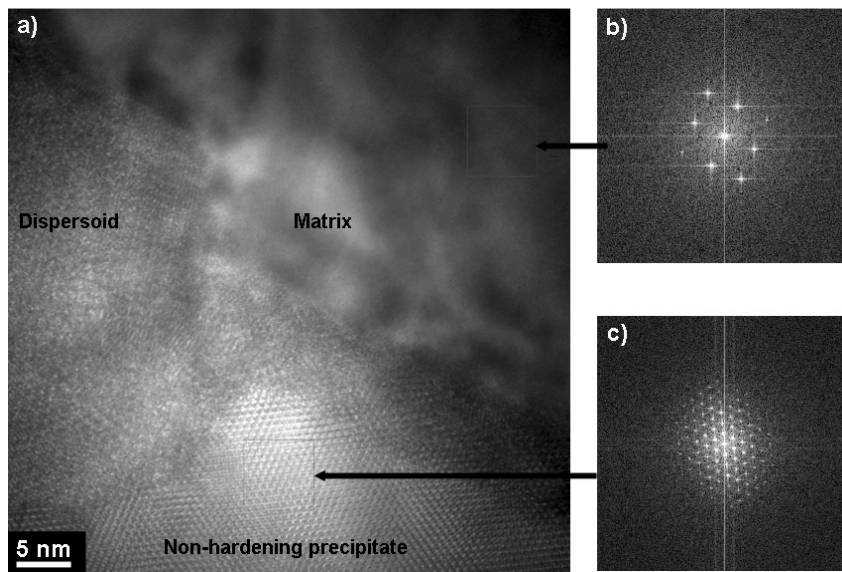
Figure 7-12 (a) High resolution TEM micrograph taken along [001]$_{Al}$ showing the interfaces between matrix, cubic dispersoid and hexagonal non-hardening precipitate. The FFTs are taken from the matrix (b) and the non-hardening precipitate (c).

The average size of the non-hardening precipitates is determined from TEM micrographs (Table 7-3). Non-hardening precipitates were found to be largest in the Cu-containing alloy BA+Cu and smallest in alloy BA. This might explain why a relatively high formation enthalpy was measured in alloy BA+Cu (Figure 7-4), considering the dispersoid density is slightly lower than in alloy HS (Figure 7-6).

Table 7-3 Average sizes of non-hardening precipitates in the three investigated alloys after cooling at 50 K/min

Alloy	Precipitate dimensions [nm]		
	length	thickness	width
BA	550 ± 160	42 ± 15	110 ± 53
HS	590 ± 200	45 ± 15	110 ± 41
BA+Cu	610 ± 200	53 ± 15	140 ± 51

7.3 Discussion

In this chapter three Al-Mg-Si alloys with distinctly different contents of the strengthening phase forming elements Mg, Si and Cu are investigated. Figure 7-13 compares the Mg:Si ratios of the three investigated alloys to the Mg:Si ratios in the equilibrium β-Mg_2Si phase and the major strengthening phase β''-Mg_5Si_6. As the dispersoid density is relatively similar, differences in quench sensitivity can be related to the effects of high Si-content and additions of Cu on precipitation during cooling from solution treatment temperature and during age-hardening. In the following sections the effects of compositional changes will first be quantified. Later, explanations for these effects are given.
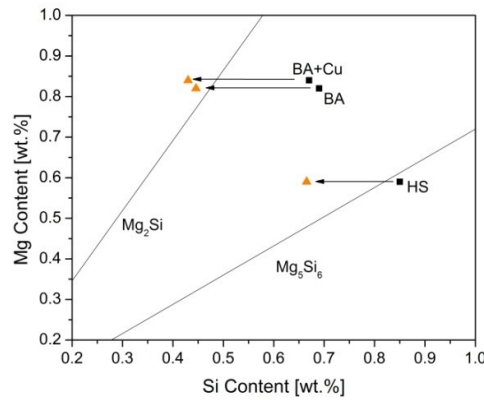
Figure 7-13 Mg:Si ratio in the three investigated alloys in relation to the Mg:Si ratio of the equilibrium phase Mg₂Si and the strengthening β"-precipitates (Mg₅Si₆). Orange marker represent the Mg:Si ratio after accounting for Si tied up in intermetallic phases and dispersoids.

7.3.1 Quantification of quench sensitivity

7.3.1.1 Quench sensitivity

Both, the dispersoid number density (Figure 7-6) as well as the formation enthalpy of phases precipitating during cooling suggest only small differences in quench sensitivity between the three investigated alloys. When plotting the difference in hardness between a water quenched and an air cooled sample, i.e. quench sensitivity, over artificial ageing time (Figure 7-14) it becomes obvious that the differences in quench sensitivity based on the differences in alloy composition are small. This is particularly true after 30 min natural ageing (Figure 7-14a), where quench sensitivity varies greatly with artificial ageing time and remains significant, showing values over 10 HV, for all investigated natural ageing times.
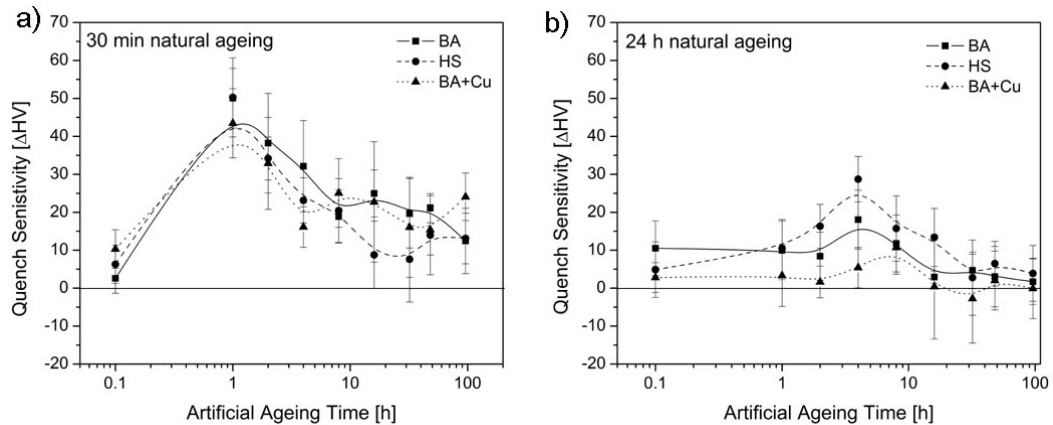
Figure 7-14 Difference in hardening response of the three model alloys between water quenched samples and air cooled samples after (a) 30 min and (b) 24 h natural ageing.

After 24 h natural ageing (Figure 7-14b) quench sensitivity is generally reduced compared to samples with 30 min natural ageing and also far less dependent on the artificial ageing time. Most interestingly, there is hardly any difference in age hardening response after long natural and long artificial ageing times, particularly in the Cu-containing alloy.

In addition it should be noted that alloy HS shows the lowest quench sensitivity amongst the three alloys after 30 min natural ageing and long artificial ageing times, but the highest quench sensitivity is after 24 h natural ageing. The artificial ageing curves suggest that the relatively low quench sensitivity after 30 min natural ageing is due to relatively fast over-ageing of the water quenched sample [105], whereas the relatively high quench sensitivity after 24 h natural ageing is due to water quenched samples showing only little negative response to natural ageing compared to the other two alloys. This indicates that the particular ageing responses of the alloys have a substantial effect on the relative differences in hardness and hence quench sensitivity.

7.3.1.2 Solute loss

The three alloys were designed to have similar dispersoid densities in order to remove the effect of the number of precipitation sites for Mg-Si-phases during cooling from the study of quench sensitivity. The number density is found to be sufficiently similar varying only by $1.5 \times 10^5/mm^2$. In comparison the dispersoid density of the commercial

alloys investigated in Chapter 4 varies by two orders of magnitude between $1.5 \times 10^4/mm^2$ and $1.7 \times 10^6/mm^2$.

The formation enthalpy of precipitates forming during cooling after solution treatment is significant in all three investigated alloy. This indicates that significant amounts of solute are lost to non-hardening precipitates forming during slow cooling. However, there are slight differences between the three alloys. Although the overall formation enthalpy of the three samples is very similar, the relative magnitude of the peaks for the high temperature reaction and for the low temperature reaction is different. In alloy BA the formation enthalpy appears to have a higher contribution from β-Mg$_2$Si than the other two samples do. As the formation enthalpy for the equilibrium β-Mg$_2$Si phase (-33.8 kJ/mol atoms [69]) is only slightly higher than the formation enthalpy of the meta-stable β'-phase (-29.4 kJ/mol atoms for β' with a composition of Mg$_2$Si suggested by Vissers et al. and described in Ravi and Wolverton [69]). Therefore, the amount of solute lost is not considered to be significantly different.

It is, however, of interest, whether any of the strengthening phase forming elements Mg, Si and Cu are removed preferentially during solute loss and whether therefore the composition of the solid solution changes with a reduction in cooling rate. Table 7-4 summarises the chemical compositions of the non-hardening precipitates which have been determined using the Oxford INCA EDX system on the conventional TEM PHILIPS CM20. The measured Mg:Si(:Cu)-ratios are then compared to the Mg:Si(:Cu)-ratios of the solid solution of the investigated alloys (accounting for Si involved in the formation of primary intermetallics and secondary dispersoids as described in Chapter 3). In comparison, the β'-phase reported by Vissers et al. [75], that corresponds well with the determined composition and lattice parameter in this work, contains a Mg:Si-ratio of 1.56:1. Earlier reports [71-73]of the β'-phase reported a Mg:Si ratio of 2, the same as the Mg:Si ratio of the equilibrium β-Mg$_2$Si-phase.

Table 7-4 Comparison between Mg:Si(:Cu) ratio in the alloy (Si content corrected based on intermetallic content) and in non-hardening precipitates forming during slow cooling.

Alloy	Mg:Si(:Cu) ratio in solid solution	Mg:Si(:Cu) ratio in nhp (measured)
BA	1.95:1	1.68:1
S	0.887:1	1.55:1
BA+Cu	1.83:1:0.49	1.5:1:0.24

The comparison shows that the non-hardening precipitates in the three investigated alloys have similar Mg:Si-ratios. For the alloys with high relative Mg contents, BA and BA+Cu, the Mg:Si-ratio in the non-hardening precipitate is found to be lower than the Mg:Si-ratio in the solid solution, indicating a relative enrichment of Mg in the solid solution. In contrast, the Mg:Si-ratio of the non-hardening precipitate in alloy HS is higher than the Mg:Si-ratio of the solid solution, suggesting a higher relative loss of Mg compared to Si due to the formation of non-hardening precipitates during slow cooling.

It has been known for several years [11, 146] that the composition of the major strengthening precipitate β" is close to 1, and potentially changes slightly with alloy composition. Marioara et al. [146] suggested an atomic Mg:Si ratio of 5:6 to produce the most favourable β"-precipitates. As the Mg:Si-ratio in the solid solutions of alloys BA and BA+Mn is far greater than the Mg:Si-ratio of the strengthening β"-precipitate a reduction of Mg in solid solution is not expected have a major effect on final age-hardening. The formation of favourable strengthening β"-precipitates is limited by the availability of Si.

In the Cu-containing alloy BA+Cu non-hardening precipitates contain Cu, however their Cu:Si-ratio is lower than in the solid solution. This indicates that after slow cooling the Cu-content in solid solution relative to the content of Mg and Si is higher compared to fast cooled samples, potentially improving the age hardening response.

7.3.1.3 Composite theory

Analogously to Chapter 6, the hardness of air cooled samples is described here by the composite model. Figure 7-15 compares the measured hardness of air cooled samples of the HS and BA+Cu alloys after 30 min and 24 h natural ageing to the hardness that would be expected according to the composite model. In alloy HS, after short natural ageing times (Figure 7-15a) and during short artificial ageing times the measured hardness is significantly lower than the predicted hardness, highlighting that vacancy-concentration related differences in precipitation kinetics dominate quench sensitivity under these age-hardening conditions. This trend is also observable after 24 h natural ageing (Figure 7-15b), although it is less pronounced, mainly due to reduced ageing kinetics in the water quenched sample in the early stages of artificial ageing.
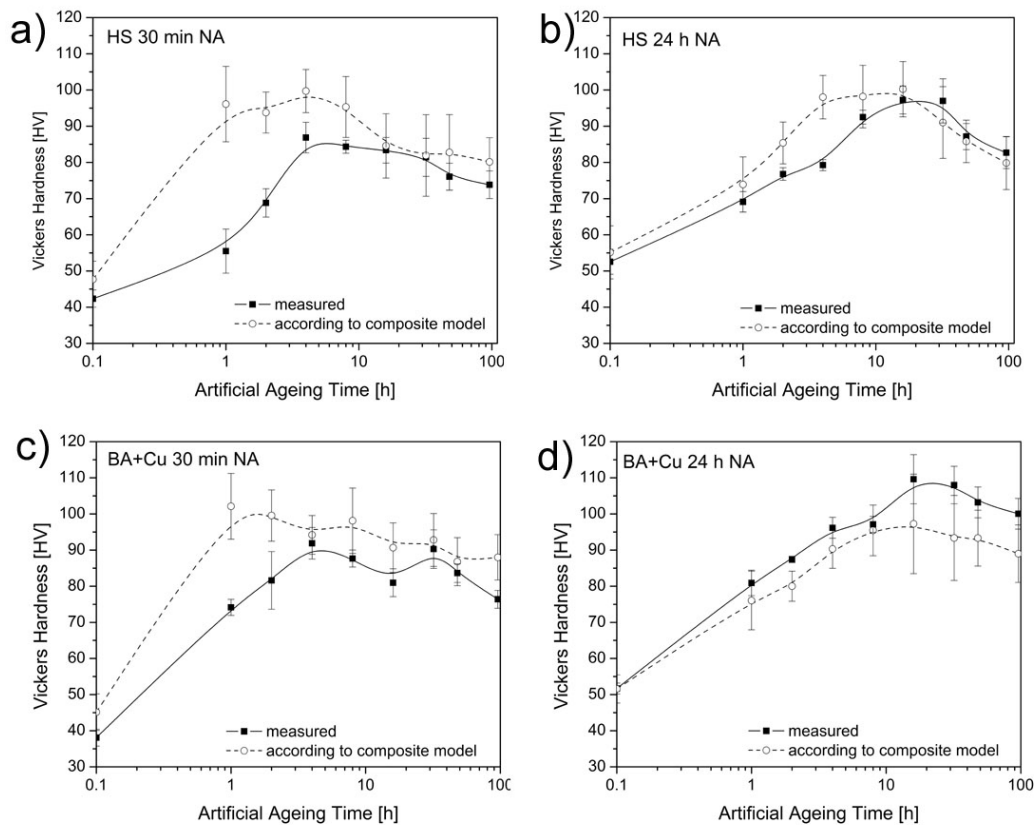
Figure 7-15 Comparison between the measured hardness and a theoretical hardness according to the composite model for alloy HS after (a) 30 min natural ageing and (b) 24 h natural ageing and for alloy BA+Cu after (c) 30 min natural ageing and (d) 24 h natural ageing.

In alloy BA+Cu (Figure 7-15c) the difference between the measured hardness and the hardness predicted by the composite model is far less pronounced after short natural ageing times than it is in alloys BA (Figure 6-15) and HS, although the same general trend is still observable. After 24 h natural ageing (Figure 7-15d) the composite model predicts lower hardness values than the measured hardness values, particularly in the later stages of artificial ageing. This suggests that age hardening response in Cu-containing alloys might be less vacancy-dependent and hence leads to lower quench sensitivity in Cu-containing alloys.

7.3.2 Explanation for quench sensitivity

7.3.2.1 Influence of natural ageing time

While quench sensitivity varies strongly with artificial ageing time after 30 min natural ageing it is almost constant over the investigated artificial ageing times after 24 h natural ageing. This circumstance, which is independent of the alloy composition, can be explained by the difference in the concentration of mobile, non-equilibrium vacancies at the start of the artificial ageing treatment. As outlined in Chapters 5 & 6, after short natural ageing times (here 30 min), a high concentration of quenched-in vacancies enhance nucleation and drive diffusion and hence growth of strengthening precipitates during the early stages of artificial ageing in water quenched samples. In contrast, precipitation of strengthening phases is thermally activated in air cooled samples and not assisted by non-equilibrium vacancies.

After long natural ageing times (here 24 h), vacancy annihilation and vacancy trapping in clusters have reduced the number of mobile vacancies in water quenched samples, such that precipitation during artificial ageing is mostly thermally activated in a very similar way as it is in air cooled samples after short natural ageing times.

7.3.2.2 Influence of alloy composition

The composition of non-hardening precipitates might influence the composition of the solid solution and therefore precipitation of the strengthening phase. However, solute that forms non-hardening precipitates diffuses from a limited region around the

dispersoid, such that large regions of the material are unaffected by solute loss in general and compositional changes as a result of solute loss in particular. Nevertheless it is interesting to note, that the alloy composition is found to have only a small effect on the composition and crystal structure of the non-hardening precipitate forming during slow cooling. While Cu appears to be involved in the formation of non-hardening precipitates, the Mg:Si-ratio of the alloy has little effect on the Mg:Si-ratio of the non-hardening precipitate.

The artificial ageing response highlights the differences in Mg-, Si- and Cu-contents. The well described, strengthening effect of Cu-additions [100, 103] leads to higher hardness in samples of alloy BA+Cu compared to alloys BA and HS during artificial ageing after 30 min natural ageing. The artificial ageing response, in particular the time to peak hardness, of the air cooled samples, where precipitation is not enhanced by the presence of mobile, non-equilibrium vacancies, is significantly faster in alloys HS and BA+Cu than it is in alloy BA. This highlights the positive effect of increased amounts of Si and Cu-additions on the strengthening and hardening response. Quench sensitivity is high in all investigated alloys. The differences between the three investigated alloys are most obvious after 24 h natural ageing. The two effects that have been identified in Chapter 6 and now determine the difference between the hardness of the water quenched and air cooled sample are the negative effect of natural ageing experienced in water quenched samples and the "positive" effect of natural ageing experienced in air cooled samples.

Compared to alloy BA, where the water quenched sample experiences a significant negative effect of natural ageing, the water quenched sample of alloy HS shows not only a delay in hardness increase but reaches the same maximum hardness values after 24 h natural ageing. As the artificial ageing response of the air cooled sample increases only a moderately, the quench sensitivity of alloy HS is the highest amongst the three investigated alloys after 24 h natural ageing. In contrast to alloy HS, natural ageing has a negative effect on water quenched samples of alloy BA+Cu, whereas the air cooled sample experiences a significantly positive effect. As a result, quench sensitivity in alloy BA+Cu is very small after 24 h natural ageing.

7.4 Conclusions

The effects of the strengthening phase forming elements Mg, Si and Cu on quench sensitivity is related to their response during natural and artificial ageing rather than their effect on precipitation of non-hardening phases during slow cooling. Although the non-hardening precipitates do not have the same composition as their respective alloys, preferential loss of any of the strengthening phase forming elements cannot be unambiguously made responsible for any of the differences in hardening response arising from the different alloy compositions. However, at a constant dispersoid density, the effects of solute loss in general and subtle differences in solute loss due to alloy composition in particular, are outweighed by the effect of a different concentration of mobile, non-equilibrium vacancies on the age-hardening response. These findings further highlight the link between slow cooling and subsequent natural ageing and emphasis the need to include the age-hardening response next to solute loss during cooling, when studying quench sensitivity.

Chapter 8   Discussion

8.1 Introduction

In this chapter the results presented in Chapters 4 to 7 are discussed and used to draw general rules for quench sensitivity in Al-Mg-Si alloys. Firstly, it is highlighted that quench sensitivity is not only dependent on precipitation during cooling from extrusion or solution treatment temperature but also on the reduced amount of quenched-in vacancies in slow cooled samples. Secondly, the role of quenched-in vacancies on the natural ageing response is discussed.

8.2 Quench sensitivity

The following sections discuss quench sensitivity in relation to both

- solute loss on heterogeneous interfaces and
- concentration of quenched-in vacancies.

Although the concentration of non-equilibrium vacancies is determined by the cooling rate from solution treatment temperature, its effect only becomes apparent during natural and artificial ageing. Therefore particular emphasis is given to the discussion of the natural and artificial ageing behaviour as a result of different vacancy concentrations.

8.2.1 Precipitation of non-hardening precipitates – Solute loss

Solute loss during slow cooling has a significant impact on the subsequent age-hardening response. The key variable for solute loss is the number density of heterogeneous nucleation sites, in particular the number density of secondary dispersoids. As a result of the precipitation of non-hardening phases the microstructure of air cooled samples shows a composite structure of solute depleted, and hence precipitate free zones and precipitate containing regions (e.g. Figure 6-9, Figure 7-7 & Figure 7-10).

In order to quantify the effect of solute loss on quench sensitivity, a number of parameters influencing solute loss have to be considered. Figure 8-1 shows a

schematic of the alloy characteristics and processing parameters that influence solute loss and ultimately lead to the formation of precipitate free zones. The dispersoid density, i.e. the number of nucleation sites is determined by the Mn and Cr content in the alloy and the homogenisation treatment. The concentration of strengthening phase forming elements Mg, Si and Cu determines the driving force for precipitation. The size of the non-hardening precipitate and the precipitate free zone are related to the cooling conditions.
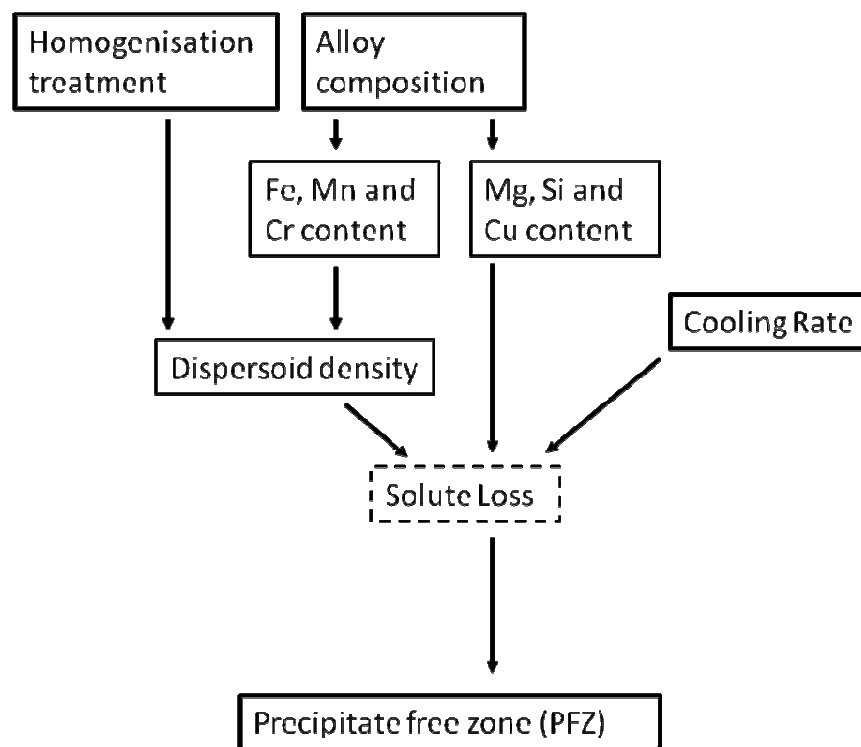
Figure 8-1 Alloy and processing parameters influencing solute loss. Solute loss leads to the formation of a precipitate free zone and hence leads to an inhomogeneous distribution of strengthening precipitates. The area fraction of the precipitate free zone limits the peak hardness of slow cooled samples.

There is a linear relationship between quench sensitivity and dispersoid density after 24 h natural ageing and 8 h artificial ageing at 175ºC for medium to high strength alloys and 8 h at 190ºC for AA6060 (Figure 8-2). At this relatively long natural ageing time the influence of non-equilibrium vacancies on quench sensitivity is negligible, such that solute loss, which is in turn related to the number density of dispersoids, is

the determining factor for quench sensitivity. Equation 1 shows the empirical relationship between the solute loss dependent quench sensitivity (QS_{SL}) and dispersoid density (ρ_d) that has been derived from all investigated alloys at the above mentioned ageing condition:

$$QS_{SL} = 5.2 + 10^{-5} \times \rho_d \qquad\qquad 8\text{-}1$$
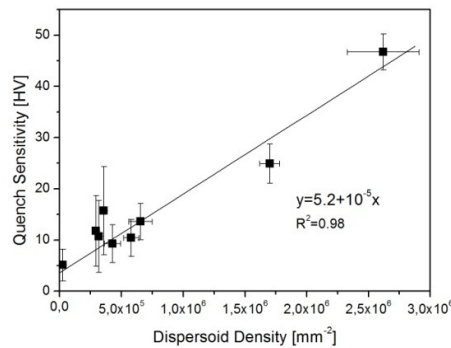
Figure 8-2 Relationship between quench sensitivity and dispersoid density after 24 h natural ageing and 8 h artificial ageing at 175ºC for the medium to hard alloys and 6 h at 190ºC for AA6060. After 24 h natural ageing, where the difference in non-equilibrium vacancies has little effect, dispersoid density is the most significant alloy feature to determine quench sensitivity.

The following sections discuss how the transition metal content and the homogenisation treatment with its parameters time and temperature determine the dispersoid density.

8.2.1.1 Influence of transition metal content on dispersoid density

Apart from homogenisation time and temperature the Mn- and Cr-content affect the dispersoid density (Figure 8-3). As the investigated alloys (Table 1 & Table 2, Chapter 3) contain Fe in excess for what is needed for the formation of dispersoids, the Fe-content will be neglected in the empirical relationship between dispersoid density and the transition metal content. The results of commercial alloys (Figure 5, Chapter 4) and laboratory alloys (Figure 4, Chapter 7), that had been heated to the homogenisation temperature of 570ºC at a rate of 200 K/h and held at this temperature for 2 h, show that there is a linear relationship between dispersoid density and transition metal content (Figure 8-3b). Cr is determined to be three to five times more efficient in

forming dispersoids than Mn (Figure 8-3a). This corresponds with the relationship proposed by Lohne and Dons [3] where Cr was suggested to be three times as potent as Mn.

$$\rho_d \sim c(Mn) + xc(Cr) \qquad \text{where } x = 3\text{-}5 \qquad \text{8-2}$$
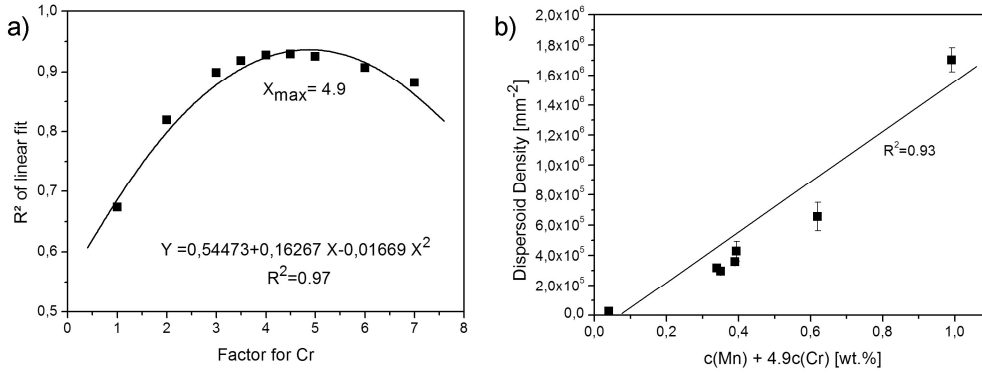
Figure 8-3 (a) Optimisation of R^2 of the linear approximation for the relationship between disperoid density and alloying elements. (b) Relationship between dispersoid denisty and transition metal content for model and laboratory alloys homogenised at 570ºC for 2 h. Cr is found to be significantly more efficient in forming dispersoids than Mn.

8.2.1.2 Influence of homogenisation treatment on dispersoid density

Dons [147] has modelled the dispersoid density as a function of alloy composition and homogenisation time and temperature. Time dependent coarsening is described by $x_{dr} \sim \sqrt{Dt}$ (6-3) whereas the dispersoid density in linearly dependent on temperature.

From the measured dispersoid density after different homogenisation treatments for alloy AA6082 (Figure 10a, Chapter 4) an empirical relationship between the homogenisation time, the homogenisation temperature and the dispersoid density can be established. Figure 8-4 shows the dispersoid density versus ln(t)×T^2 which can be fitted with an exponential relationship.
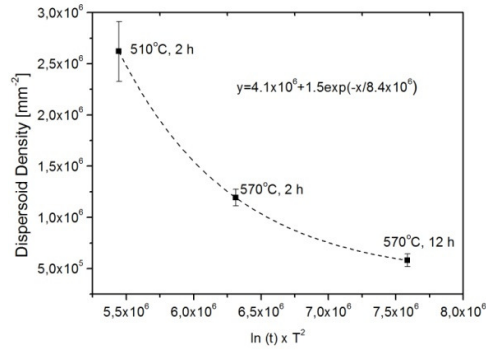
Figure 8-4 Empirical relationship between dispersoid density and homogenisation time and temperature according to the results of section 4.3, Chapter 4.

For the investigated alloy AA6082 the following empirical relationship was derived. The dispersoid density is proportional to the homogenisation time t and decreases exponentially with homogenisation time T.

$$\rho_d = 4.1 \times 10^6 + 1.5t \times e^{\left(\frac{-T}{4.2\times10^6}\right)} \qquad\qquad 8\text{-}3$$

8.2.1.3 Formation of non-hardening precipitates

Beside the dispersoid density, the number density of heterogeneous nucleation sites, solute loss is influenced by the driving force for precipitation related to the solute supersaturation. The amount of non-hardening phase precipitating during cooling from extrusion or solution treatment temperature is represented by the formation enthalpy ΔH measured by DSC (Table 1, Chapter 4; Figure 4, Chapter 7). As well as depending on the amount of the phase forming ΔH is influenced by the crystal structure and composition. Figure 8-5 compares quench sensitivity to the formation enthalpy measured during cooling at 50 K/min. It can be seen that there is a linear relationship between the two parameters in Cu-free alloys. The two Cu-containing alloys AA6061 and BA+Cu show a higher ΔH relative to the measured quench sensitivity. Hence the findings of the TEM studies, which found that non-hardening precipitates contain Cu (Figure 7, Chapter 4; Figure 10, Chapter 7) indicate that the Cu content may change the formation enthalpy ΔH of that phase.
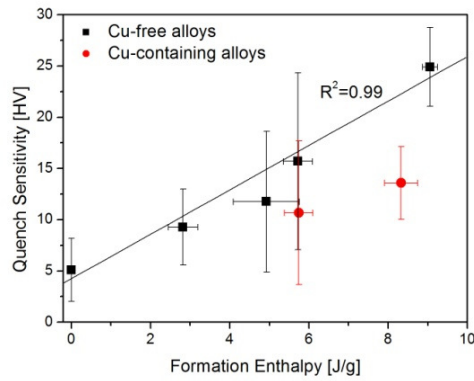
Figure 8-5 The relationship between quench sensitivity (after 24 h natural ageing and the standard artificial ageing treatment) and the formation enthalpy recorded during cooling after solution treatment shows that only part of quench sensitivity is related to solute loss.

It is assumed that each dispersoid is a precipitation site for one non-hardening precipitate. The formation enthalpy of non-hardening precipitates during cooling at 50 K/min (Figure 6, Chapter 4 and Figure 4, Chapter 7) standardised by the dispersoid density (ρ_d) should then be a measure for the size of the non-hardening precipitates and be related to the solute content, which drives this precipitation. The composition of the non-hardening β'-precipitates is discussed controversially in literature [69, 75, 76, 148]. Mg:Si-ratios between 0.44:1 and 1.8:1 have been reported [69, 75, 76, 148]. On average the Mg:Si-ratio of non-hardening precipitates n this study was determined to be 1.58.

$$\frac{\Delta H}{\rho_d} \sim c(Mg_{1.58}Si) \qquad\qquad 8\text{-}4$$

Figure 8-6, however, shows that there is no obvious relationship between the formation enthalpy per non-hardening precipitate and the solute content.
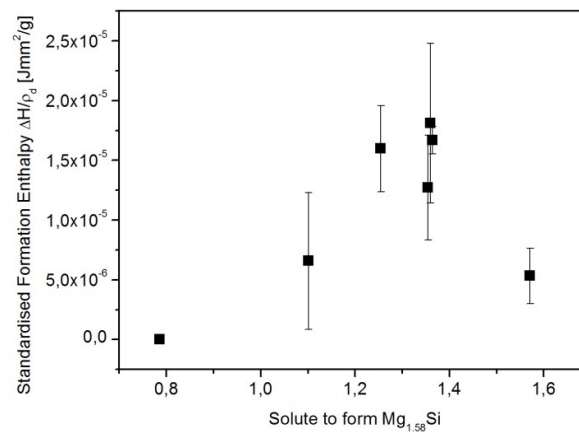
Figure 8-6 The standardised formation enthalpy for non-hardening precipitates is plotted against the Mg$_2$Si content of the investigated alloys.

It is therefore concluded that the Mg and Si content and hence the driving force for precipitation have only a small influence on the precipitation of non-hardening β'-phases during cooling after extrusion or solution treatment. Nucleation on heterogeneous sites is the dominant factor determining solute loss.

8.2.2 Vacancy concentration

The concentration of mobile, non-equilibrium vacancies is responsible for a high age-hardening response [43]. Vacancies are able to affect both nucleation and growth of zones and precipitates. As nucleation and growth occur during both natural and artificial ageing, the influence of non-equilibrium vacancies has to be investigated in both processing steps (Figure 8-7).
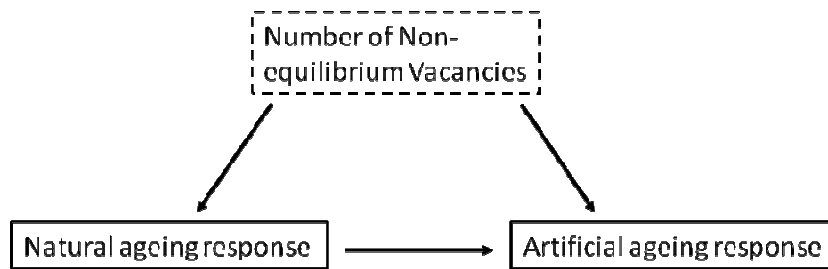
Figure 8-7 The natural and artificial ageing response are significantly influenced by the concentration of non-equilibrium vacancies, which in turn is a result of the cooling rate from solution treatment temperature.

In the following sections it will be rationalised how non-equilibrium vacancies affect precipitation, i.e. whether either nucleation or growth or both are affected.

8.2.2.1 Effect of vacancies on nucleation

Heterogeneous nucleation is the predominant nucleation mechanism in alloys as the destruction of non-equilibrium defects releases some free energy. These non-equilibrium defects can be excess vacancies, dislocations, grain boundaries and free surfaces. Excess, non-equilibrium vacancies can act as heterogeneous precipitation sites in various ways. On the one hand, excess vacancies can act directly as nucleation sites. Pogatscher et al. [43, 149, 150] highlight that the presence of non-equilibrium vacancies is the rate determining step during artificial ageing immediately after fast quenching as they have a relatively high energy due to their high concentration. Although the misfit strain energy of a mono-vacancy is not particularly high, the high vacancy concentration (e.g. 10^{-6} per atom) results in a high total free energy of the material. Therefore, precipitates that form on a mono-vacancy need to have a low interfacial energy (i.e. be fully coherent) and a high driving force needs to be present [27]. The high concentration of point defects, however, provides a high number density of precipitation sites, such that a dense distribution of clusters and/or zones can form.

On the other hand, non-equilibrium vacancies annihilate during natural ageing and potentially during slow cooling, depending on the original microstructure on jogs at existing dislocations, on Frank loops or on grain boundaries [41], and thereby increase the density of the respective defects. These can then act as nucleation sites [149].

Compared to a single vacancy, which is a point defect, dislocations, Frank loops and grain boundaries are line or surface defects and have higher free energies. Therefore, the precipitation of semi- or incoherent phases is promoted. The number density of surface defects is generally significantly smaller than the number density of quenched-in vacancies, such that there are significantly less nucleation sites.

In this context, apparent changes in the precipitation sequence between water quenched samples and air cooled samples shall be discussed. The strengthening β''-precipitates form as part of a precipitation sequence from coherent clusters and GP-zones [11, 113]. This is promoted by the presence of a high concentration of non-equilibrium vacancies in fast cooled samples. DSC scans during heating show two distinct peaks for the formation of β'' and β', respectively (Figure 6-5 & Table 6-2). The peak for β''-formation is with approximately 12 J/g ± 0.5 significantly larger than the peak for β'-formation (6.4 J/g ± 0.2 for 30 min natural ageing). In contrast, in slow cooled samples the lack of quenched in vacancies suppresses the formation of clusters and/or zones. In turn, the lack of β''-precursors suppresses the precipitation of β'' during artificial ageing. The peaks measured in DSC scans for β''-formation (3.5 ± 0.2 J/g) is significantly smaller than for β'-formation (7.2 ± 0.4 J/g). In addition, the increased amount of heterogeneous nucleation sites might promote the precipitation of the semi-coherent β'-precipitate and hence lead to changes in the precipitation sequence.

Although no precise, quantitative statement on the strengthening contribution of β''- and β'-precipitates can be made from the current results, it should be pointed out that both β''- and β'-precipitates add to the strength of the material. The smaller formation enthalpy of β''-precipitates and the larger formation enthalpy of the semi-coherent β'-precipitates suggest a similar strengthening contribution from β''- and β'-precipitates.

8.2.2.2 Effect of vacancies on cluster and precipitate growth

Quenched-in vacancies enhance the growth of clusters and precipitates by accelerating diffusion. The effective diffusion coefficient D_{eff} is directly proportional to the vacancy site fraction y_0 [41].

$$D_{eff} = \frac{y_0}{y_{eq}} D_{eq} \qquad \text{8-5}$$

D_{eq} is the equilibrium diffusion coefficient and y_{eq} is the equilibrium vacancy site fraction at the respective temperature. In order to approximate the vacancy concentration at a given natural ageing time, a relationship between vacancy site fractions simulated for a similar alloy by Lang et al. [39] and the initial average positron lifetime measured for pure Al, AA6060 and the model alloy BA is established (Figure 8-8, equation 6). The raw data is presented in Table 8-1.

In the following section an effort is made to relate vacancy density to average positron lifetime. The average positron lifetime is the result of a number of effects that cause differences in electron densities, e.g. alloying elements and their surrounding, the type and density of matrix – second phase – interfaces and vacancy density.

Using the initial positron lifetime immediately after quenching offers the closest approximation of lifetime solely related to vacancy concentration without the influence of clusters and phases, which have not formed at this early stage. This assumption is not without flaws. The relatively large difference between the initial average positron lifetime in air cooled samples of alloy BA and pure Al shows that solute-vacancy interactions take place and have a significant influence on the average positron lifetime.

$$D_{eff} = \frac{y_0}{y_{eq}} D_{eq} \qquad \text{8-5}$$

Table 8-1 Average lifetime τ$_{AV}$ values determined for alloy BA (Figure 6-15) and corresponding vacancy site fractions simulated by Lang et al. [39] immediately after quenching. The vacancy site fraction after 30 min natural ageing is very similar to the initial vacancy site fraction and therefore not listed separately.

	WQ	OQ	AC	equilibrium at RT
initial average positron lifetime (τ$_{AV}$) in alloy BA	221 ps	215 ps	205 ps	164 ps
initial average positron lifetime (τ$_{AV}$) in AA6060	231 ps	194 ps	187 ps	164 ps
initial average positron lifetime (τ$_{AV}$) in pure Al	215 ps	190 ps	170 ps	164 ps
initial vacancy site fraction (y$_0$)	1×10^{-5}	4×10^{-7}	1.7×10^{-8}	6×10^{-12}
vacancy site fraction after 24 h NA	2×10^{-10}	2×10^{-10}	1×10^{-10}	6×10^{-12}
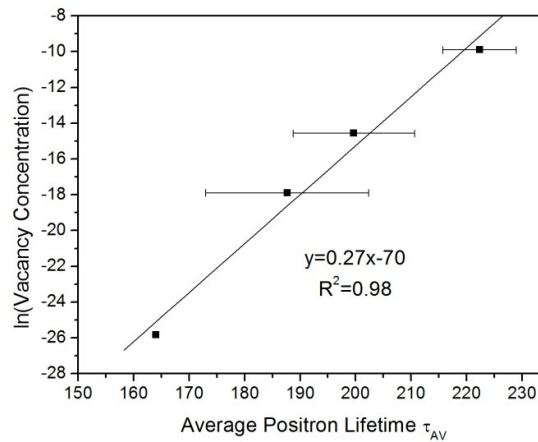
Figure 8-8 Relationship between simulated vacancy concentration and the initial average positron lifetime from PALS measurements of the model alloy BA (Table 8-1).

Empirically the relationship between the vacancy concentration y_0 and the average positron lifetime τ_{AV} is determined to be:

$$y_0 = 4.0 \times 10^{-31} e^{(0.27\tau_{AV})} \qquad\qquad 8\text{-}6$$

This relationship is applied to the average positron lifetime measured for water quenched, oil quenched and air cooled samples of pure Al (99.99%) shown in Figure 8-9 (Figure 5-10), as the average positron lifetime of pure Al is not influenced by

clustering and hence mainly related to the vacancy concentration. The solid points represent the simulated vacancy concentrations [39].

Determining the vacancy concentration from τ_{AV} bears some inaccuracies. Due to a lack of vacancy-solute interactions, the vacancy concentration in pure Al samples is rather low (Figure 5-10). However, clustering reactions affect τ_{AV} more significantly (Figure 5-11 & Figure 6-15), such that determining vacancy concentration from τ_{AV} of the pure Al sample gives the most accurate approximation.
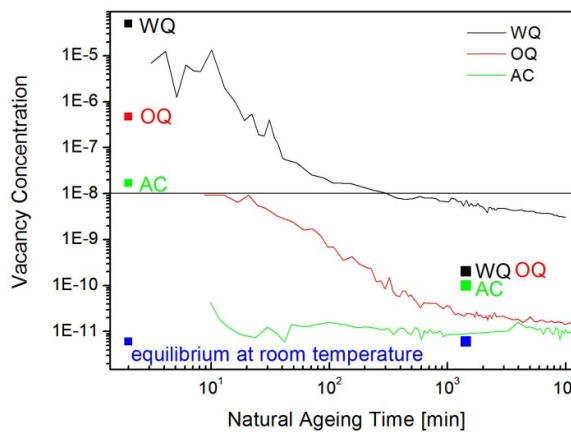
Figure 8-9 Vacancy concentration determined from PALS data from a pure Al sample (Figure 5-10) is in a similar order of magnitude as the simulated vacancy concentrations. The horizontal line indicates the equilibrium vacancy concentration at artificial ageing temperature.

There is a reasonable agreement between the two sets of data. Discrepancies between the simulated and determined vacancy concentrations result from rapid vacancy annihilation within the first minutes in the pure Al samples as well as probably the formation of Frank loops in the water quenched sample after prolonged natural ageing [41, 118].

At room temperature, where the equilibrium vacancy concentration is low (6×10^{-12}), all samples have diffusion kinetics enhanced by the presence of non-equilibrium vacancies (Figure 8-9). However, at the artificial ageing temperatures of 175ºC for the medium to high strength alloys and 190ºC, where the equilibrium vacancy concentration is approximately $1 - 2 \times 10^{-8}$ [39] (indicated by the horizontal line) most

samples do not show vacancy supersaturation. As a result diffusion kinetics at artificial ageing temperature are only enhanced for fast cooled samples after short natural ageing times. It should be kept in mind that the enhancing effect of non-equilibrium vacancies is always relative to the equilibrium diffusion coefficient, such that, although diffusion at room temperature is enhanced by mobile vacancies, it is slow compared to diffusion at the artificial ageing temperature.

For a calculated diffusion factor $y_0/y_{eq} < 1$, i.e. where the initial vacancy concentration is smaller than the equilibrium vacancy concentration at the respective artificial ageing temperature, diffusion is thermally activated [43]. Within the first minutes of artificial ageing [48] the vacancy concentration increases to the equilibrium vacancy concentration at artificial ageing temperature, such that diffusion is driven by the equilibrium vacancy concentration and not enhanced by the presence of mobile, non-equilibrium vacancies. The diffusion coefficient at the equilibrium vacancy concentration is then the effective diffusion coefficient (D_{eq} (T_{AA}) = D_{eff}).

8.2.2.3 Precipitation kinetics during natural ageing

There are many reports in the literature that discuss possible mechanisms and the effect of natural ageing in water quenched samples [22, 81, 85, 129]. Chang and Banhart et al. [90, 95-97] identified several clustering reactions occurring within the first hour of natural ageing and another one which is completed after 2 weeks. The present DSC results show in both AA6060 (Figure 5-3) and alloy BA (Figure 6-5) that significant clustering has occurred in water quenched samples at 24 h natural ageing. These results correlate with the findings of the present PALS study. Water and oil quenched samples show a peak in average lifetime within the first hour of natural ageing, and a second peak after approximately 1000 min. The first peak relates to the early clusters described by Chang and Banhart [90], whereas the second peak in the observed PALS curves can be related to the later clustering reaction identified by the same authors.

Since hardness increases during natural ageing in all investigated samples (Figure 5-1 & Figure 6-1) clustering must occur in air cooled samples as well. Several results from the present study indicate a reduced rate and intensity of clustering in air cooled samples:

- The hardness increase during natural ageing is lower in air cooled samples compared to oil and water quenched samples (Figure 5-1 & Figure 6-1**)**.
- No peaks for clustering can be recorded during DSC scans in air cooled samples of alloy BA (Figure 6-5).
- Air cooled samples do not show a peak in average positron lifetime within the first 100 min after quenching (Figure 5-11 & Figure 6-15)

Although this study has not produced any direct evidence on the nature or density of clusters in air cooled samples, it is suggested that a lack of non-equilibrium vacancies leads to a lack of nucleation sites for clusters (8.2.2.1The large distance between clusters and the low diffusion coefficient (Figure 8-8) as a result of the low vacancy supersaturation leads to slow cluster growth. It is concluded that the clusters that form in slow cooled samples show a lower density and are not necessarily the same clusters as those that from in fast cooled samples.

8.2.2.4 Precipitation kinetics during artificial ageing

As a measure for precipitation kinetics an age hardening rate is introduced. The initial age hardening rate $H\dot{V}_0$, defined as the hardness increase in the first hour of artificial ageing, is related to precipitation of β"-precursors, i.e. GP-zones, and the formation and growth of β"-precipitates [11]. As these processes are controlled by vacancy-assisted nucleation and diffusion, $H\dot{V}_0$ is also related to the concentration of mobile, non-equilibrium vacancies at the start of artificial ageing. Furthermore, a general age hardening response $H\dot{V}_P$ is defined as the hardening rate to peak hardness.

Figure 8-10 shows $H\dot{V}_0$ for a) BA, b) HS, c) BA+Cu and d) AA6060. $H\dot{V}_0$ is generally high in water quenched samples of the model alloys after short natural ageing times. For alloys BA (Figure 8-10a) and BA+Cu (Figure 8-10b) the maximum hardness is reached within the first hour of artificial ageing such that $H\dot{V}_0$ is the same as $H\dot{V}_P$.
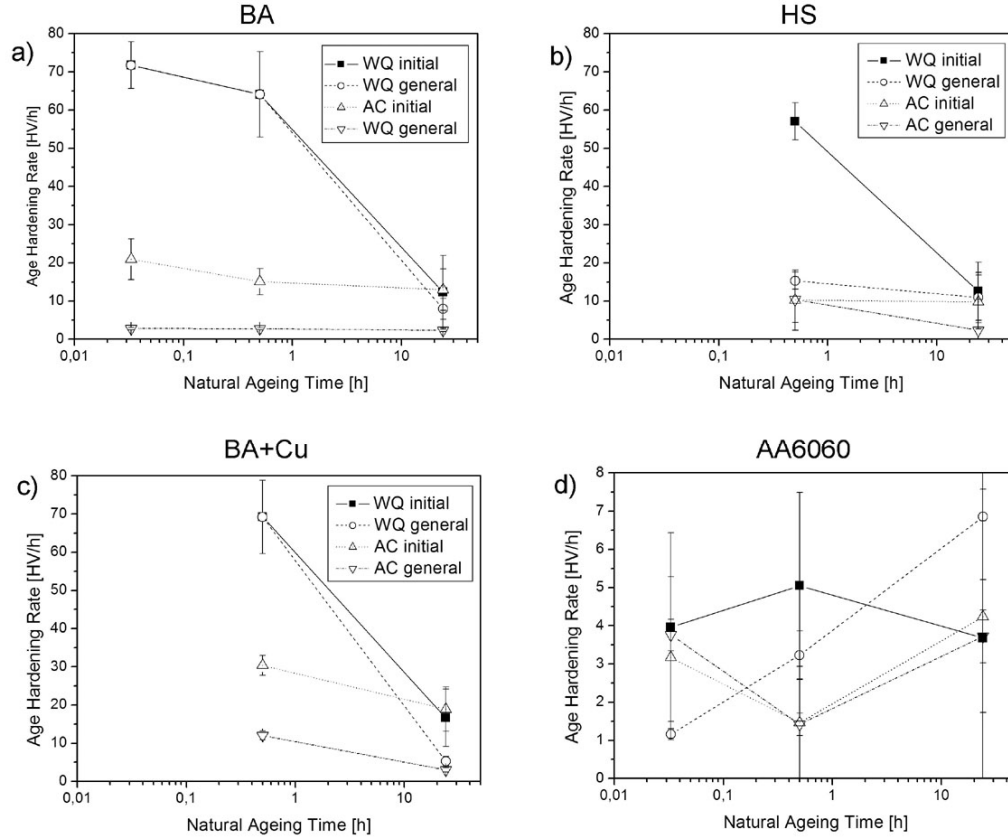
Figure 8-10 Initial age hardening rate and general age hardening response depending on the natural ageing time of water quenched and air cooled samples of (a) BA, (b) HS, (c) BA+Cu and (d) AA6060. The y-scale for AA6060 is one tenth of the y-scale of the model alloys, showing significantly lower age hardening rates. The symbols are the same as for the model alloys.

The contribution of non-equilibrium vacancies on $H\dot{V}_0$ can be derived from Figure 8-11. The initial vacancy concentration y_0 is determined from the initial average positron lifetime (Table 8-1) and the relationship in equation 6. For the diffusion factor y_0/y_{eq} the equilibrium vacancy concentration at the respective artificial ageing temperature, 1×10^{-8} at 175ºC for the model alloy BA and 2×10^{-8} at 190ºC for AA6060, are used [39]. The vertical lines indicate where the diffusion factor y_0/y_{eq} equals 1. This means that after short natural ageing times fast cooled samples show some enhanced diffusion, whereas in slow cooled samples and in all samples after 24 h natural ageing diffusion and hance $H\dot{V}_0$ are independent of the vacancy supersaturation.

It can be seen, that the age hardening rate of the lean, commercial AA6060 alloy is generally low and independent of the concentration of non-equilibrium vacancies. Although the diffusion factor for water quenched samples greater than one suggests that diffusion and nucleation is enhanced by non-equilibrium vacancies (Figure 8-11), the low age hardening rate indicates thermally activated diffusion. This can be related to the low solute supersaturation and hence a low driving force.
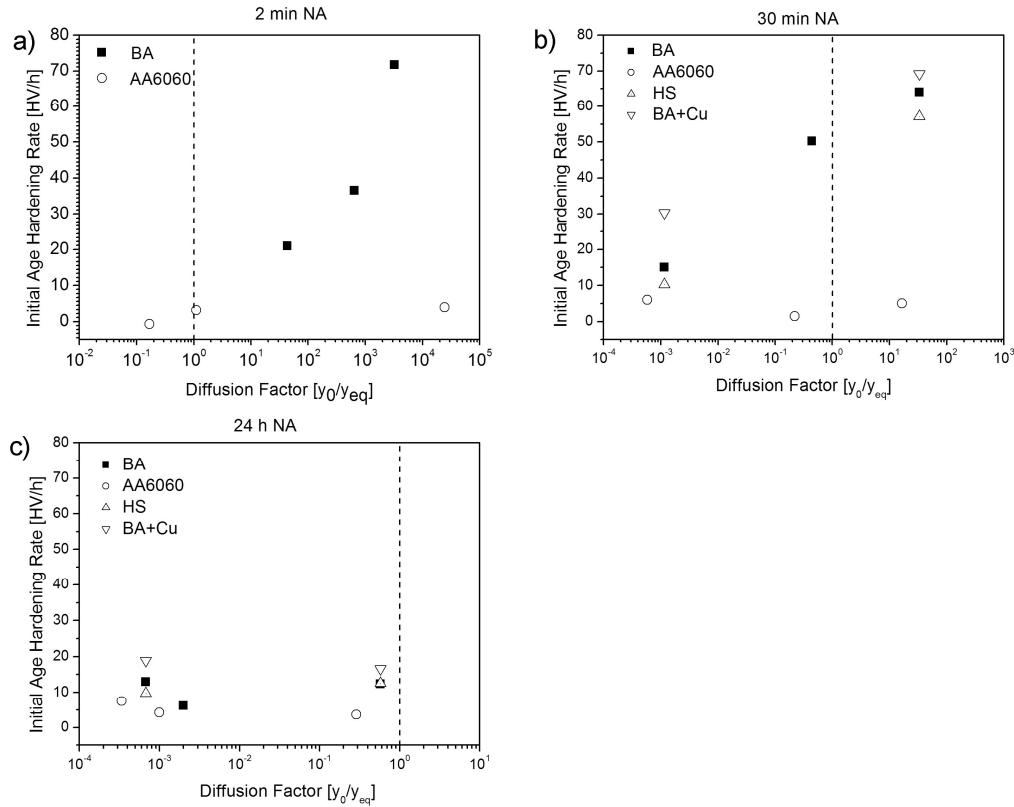
Figure 8-11 Comparison between diffusion factor y_0/y_{eq} at artificial ageing temperature (175ºC for alloy BA and 190ºC for AA6060 from [39]) and initial age hardening rate shows that the initial age hardening rate is dependent on the diffusion factor for the model alloys after 2 min (a) and 30 min (b). After long natural ageing times (c) and in slow cooled samples there is no enhancing effect of vacancy supersaturation. In the lean alloy AA6060 vacancy supersaturation does not enhance diffusion.

In the fast cooled samples of the model alloys $H\dot{V}_0$ is the same as $H\dot{V}_P$ (Figure 8-10) as peak hardness is achieved within the first hour. Quench sensitivity of model alloys for short natural ageing times is also greatest after very short artificial ageing times, where water quenched samples have undergone a rapid hardness increase due to the high vacancy supersaturation and the hardness increase is slow in air cooled samples. An

empirical relationship between vacancy related quench sensitivity and the initial vacancy concentration in water quenched samples can be drawn. As an example alloy BA is used. The relationship between $H\dot{V}_0$ and y_0/y_{eq} can be derived from Figure 8-11a:

$$H\dot{V}_0 = 0.015 \frac{y_0}{y_{eq}} + 23 \qquad\qquad 8\text{-}7$$

In the model alloys quench sensitivity is greatest after short natural and artificial ageing time (Figure 7-14), here 2 min and/or 30 min natural ageing and 1 h artificial ageing. At these ageing conditions the great hardness increase of water quenched samples is caused by the vacancy supersaturation enhancing precipitation. In air cooled samples precipitation kinetics and the hardness increase are slow. Quench sensitivity is therefore related to the difference in vacancy supersaturation and therefore designated QS_{Va}. Figure 8-12 compares the quench sensitivity after 1 h artificial ageing to $H\dot{V}_0$.
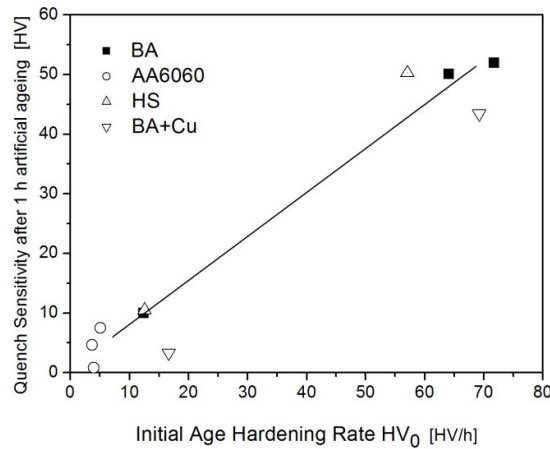
Figure 8-12 Relationship between quench sensitivity after 1 h of artificial ageing and the initial age hardening rate for determining the maximum contribution of the vacancy concentration to quench sensitivity.

$$QS_{Va} = 0.8\, H\dot{V}_0 = 1.2 \times 10^7 y_0 + 18.4 \qquad\qquad 8\text{-}8$$

The artificial ageing temperature is 175ºC, such that the equilibrium vacancy concentration is 1×10^{-8}.

The general age hardening rate is defined as the rate to the respective peak hardness. It allows conclusions on the feasibility of ageing treatments. A high general age hardening rate indicates a short artificial ageing time to peak hardness and hence an effective ageing treatment. This is particularly interesting with regards to the effect on natural ageing, which is discussed in section 8.3.

There are distinct differences between the model alloys and the dilute commercial alloy AA6060. The initial and general age hardening rates as well as the peak hardness are much lower in AA6060 than in the model alloys. Neglecting the air cooled sample after 2 min natural ageing, the general age hardening rate increases with increasing natural ageing time. This shows that mobile, non-equilibrium vacancies do not significantly assist artificial ageing. Artificial ageing is therefore thermally activated rather than supported by mobile vacancies, independent of the natural ageing time.

8.2.2.5 Influence of Mg:Si-ratio and Cu on age hardening

The present results do not allow statements on the influence of the Mg:Si-ratio or Cu additions on clustering during natural ageing. However, since no significant differences have been observed in the precipitation of non-hardening phases during cooling, the differences in quench sensitivity between the model alloys must arise from the influence of the Mg:Si-ratio or Cu additions on age hardening. In alloy HS, which contains a high Si content relative to Mg, natural ageing has only a small negative effect in fast cooled, such that quench sensitivity is relatively large after prolonged natural ageing. In the Cu-containing alloy BA+Cu, natural ageing has a relatively strong positive effect in the slow cooled samples, such that quench sensitivity is relatively small after prolonged natural ageing. Both the low Mg:Si-ratio and the Cu additions lead to an increase in peak hardness.

However, Cu additions appear to have a strong negative effect on natural ageing in water quenched samples (Figure 8-13 & Figure 8-14). Since this negative effect is not observed in air cooled samples, it is suggested that vacancy trapping is particularly pronounced in Cu-containing samples.

Samples containing high amounts of Si compared to their Mg content (e.g. alloy HS) show a delayed artificial ageing response even after short natural ageing times. In this case the high vacancy supersaturation seems not to be sufficient to drive rapid precipitation. This might also offer an observation for the limited negative effect of natural ageing. Vacancies might also not drive clustering in the same ways as they do in Cu containing samples, such that natural ageing has a lesser effect.

8.2.3 Rationalisation of Solute Loss and Reduced Number of Vacancies

The key finding of the present work is that quench sensitivity, the difference in age hardening response between water quenched and air cooled samples, is the result of a combination of solute loss during slow cooling and a difference in the concentration of quenched-in vacancies.

$$QS = QS_{SL} + QS_{Va} \qquad \text{8-9}$$

where

$$QS_{SL} = 5.2 + 10^{-5} \times \rho_d \qquad \text{8-1}$$

and

$$QS_{Va} = 1.2 \times 10^7 y_0 + 18.4 \qquad \text{8-8}$$

Although a number of assumptions have been made to derive these empirical equations the data still gives a reasonable description of quench sensitivity and offers a basis for comparing physical models.

8.3 Natural ageing response

The present study not only leads to the explanation of quench sensitivity, but also allows some conclusions on the effect of natural ageing and the mechanisms behind this phenomenon and its different effect on different alloys.

Figure 8-13 compares the hardness after various cooling rates and natural ageing times after 4 h artificial ageing at 175ºC for the model alloys BA, BA+Cu and HS, which all contain combined Mg and Si contents greater than 1 wt.% and after 8 h at 190ºC for AA6060 which contains a combined Mg and Si content of 0.88 wt.%. These artificial ageing conditions are typical for the respective alloys during industrial processing.

It shows that water quenched samples (Figure 8-13a) of the moderately alloyed model alloys BA and BA+Cu show a negative response to natural ageing, while the hardness of the water quenched sample of alloy HS appears to be independent of the natural ageing time. The water quenched sample of the lean commercial alloy AA6060 responds positively to natural ageing. This confirms the general trend that has been reported in literature [88-90, 98, 137].

However, slow cooled samples do not necessarily follow the same trend as their fast cooled counterparts (Figure 8-13b). While the air cooled samples of alloys BA and HS show a steady to slightly negative response to natural ageing, the air cooled sample of alloy BA+Cu shows a positive response. The air cooled sample of alloy AA6060 also shows, with exception of the hardness after 2 min natural ageing a positive response.
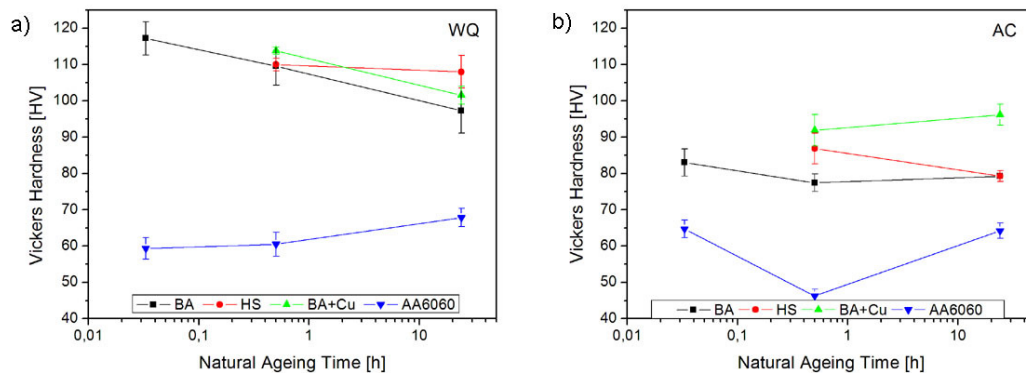
Figure 8-13 The hardness values achieved after 4 h at 175ºC (model alloys) or after 8 h at 190ºC (AA6060) for (a) water quenched and (b) air cooled samples show that natural ageing can have a positive or negative effect depending on cooling rate and alloy composition.

This trend is more obvious when the respective peak hardness values are compared (Figure 8-14). As some of these peak hardness values are reached after commercially viable times (> 8 h) the comparison is used to highlight the physical mechanisms rather

than optimised ageing conditions. Air cooled samples of the model alloys show a significantly higher peak hardness after 24 h natural ageing, whereas the peak hardness is reduced to a greater extent in the water quenched alloys.
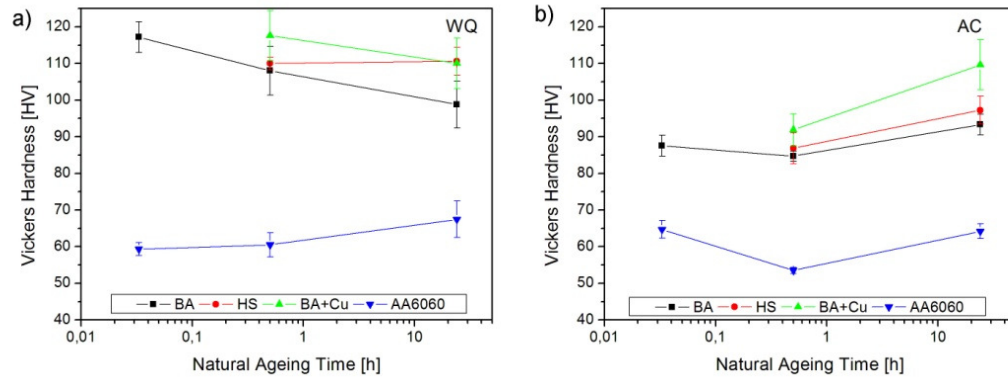
Figure 8-14 Maximum achievable hardness values during artificial ageing at 175ºC for model alloys and 190ºC for alloy AA6060 in (a) water quenched and (b) air cooled samples show the potential for optimising the age-hardening regime.

In the following sections possible origins of negative and positive effects that can be drawn from the present study are discussed separately.

8.3.1 Negative effect of natural ageing

The negative effect of natural ageing is predominantly present in fast cooled samples with a Mg+Si content greater than 1 wt.%. Most studies in the literature [22, 81, 85, 90, 99, 129] highlight the role of solute loss to stable clusters that do not act as precipitation sites or precursors of the major strengthening phase β". Only recently Zurob [44] and Pogatscher et al. [43] described the importance of mobile, non-equilibrium vacancies in artificial ageing and vacancy trapping during natural ageing as a contributor to the negative effect of natural ageing.

The present results show that after short natural ageing times water quenched samples of the model alloys all show very high initial age hardening rates for the first hour of artificial ageing and mostly reach their peak hardness in this time (Figure 8-10). At this stage a high concentration of mobile, non-equilibrium vacancies support diffusion and hence precipitation of strengthening precipitates and cluster growth has

not been significant. $H\dot{V}_P$ decreases for all water quenched samples with natural ageing time demonstrating reducing artificial ageing kinetics. In alloy HS this decrease in general age hardening rate is less pronounced, as is the negative effect of natural ageing. This suggests that the decrease of the concentration of mobile, non-equilibrium vacancies, which can occur by trapping in clusters or annihilation, has a major impact on the decrease in achievable hardness and strength after prolonged natural ageing.

8.3.2 Positive effect of natural ageing

The positive effect of natural ageing is well known for alloys with a Mg+Si content less than 1 wt.% [88, 89, 98]. Several mechanisms have been proposed:

- Clusters that form during natural ageing might act as precipitation sites in a similar way as clusters formed during pre-ageing do [81, 98, 129].

- Clusters predominately take up Si, such that the precipitating β" are Mg-rich and remain finer [98].

- Clusters act as solute-reservoirs. By dissolving slowly during artificial ageing previously unavailable Mg and Si becomes available leading to increased strength and hardness [89].

In the present study the positive effect has not only been observed in the dilute, commercial alloy AA6060. Air cooled samples of the higher alloyed model alloys can also show a positive effect (Figure 8-14b). In these samples the peak hardness is higher but the hardness increase is slower, such that it depends on the artificial ageing time as to whether natural ageing has a no effect (Figure 8-13b) or a positive effect (Figure 8-14b). This work cannot clarify whether or not the same mechanisms are responsible for higher peak hardness values after longer natural ageing times, however, there are similarities in the age hardening response between AA6060 and the air cooled samples of the model alloys. Neither group of samples shows a high artificial ageing response after short natural ageing times (Figure 8-10; Figure 2, Chapter 5; Figure 2, Chapter 6). The general age hardening rate is either constant (BA air cooled Figure 8-10a) or varies

slightly. This is a result of diffusion during artificial ageing being thermally activated rather than enhanced by a high supersaturation of mobile vacancies.

In addition to similar artificial ageing kinetics it is suggested that clustering during natural ageing has some effect. In contrast to fast cooled samples with a Mg+Si content greater than 1 wt.%, a smaller number of clusters form and their growth is slow. This leads to reduced solute loss and potentially leads to small clusters that can act as nucleation sites for β" precipitation. The activation energies determined for air cooled samples of alloy BA (Chapter 6, Table 3) are significantly higher in the sample naturally aged for 30 min (167 kJ/mol) than in the sample naturally aged for 24 h (90 kJ/mol). This indicates that some mechanism, possibly the presence of precipitation sites, enhances precipitation in air cooled samples and consequently the samples' response to natural ageing.

8.4 Summary

This study has identified the origins of the difference in hardening response between fast and slow cooled samples of 6xxx series alloys. Figure 8-15 shows a schematic of the influence of process parameters and alloy characteristics that are responsible for quench sensitivity. It is well known, that solute loss, determined by the number density of secondary dispersoid phases which act as precipitation sites for solute during cooling leads to a reduced age hardenability of slow cooled samples. It has been previously suggested [38] and confirmed by the present work, that solute loss is limited to a precipitate free zone with the remaining regions remaining supersaturated with solute. This means that solute loss only affects a limited volume of the microstructure.

The remainder of the difference in age hardening response is attributed to the reduced number of quenched-in vacancies and their effect on natural and artificial ageing response. Both natural and artificial ageing are influenced by the Mg, Si and Cu content, such that quench sensitivity is the result of slow cooled and fast cooled samples reacting differently to a number of processing steps.

Figure 8-16 summarises the effect of alloy composition and cooling rate and describes the resulting artificial aging responses. Four categories can be differentiated:

- Slow cooled soft alloys
- Fast cooled soft alloys
- Slow cooled medium to hard alloys
- Fast cooled medium to hard alloys

Soft alloys and the slow cooled samples of medium to hard alloys all contain a low concentration of quenched-in vacancies such that clustering and precipitation kinetics are thermally activated and hence low, independent of the natural ageing time. In contrast, fast cooled samples of medium to high strength alloys are initially highly supersaturated with vacancies, such that clustering and precipitation kinetics are driven by vacancies and hence rapid. During natural ageing vacancy annihilation and trapping lead to a reduction in the number of mobile, non-equilibrium vacancies. After prolonged natural ageing, artificial ageing kinetics are thermally activated and hence much reduced compared to the vacancy driven kinetics.

As a result, quench sensitivity is not only the result of solute loss during cooling but also ageing kinetics and the different response to natural ageing between fast and slow cooled samples.
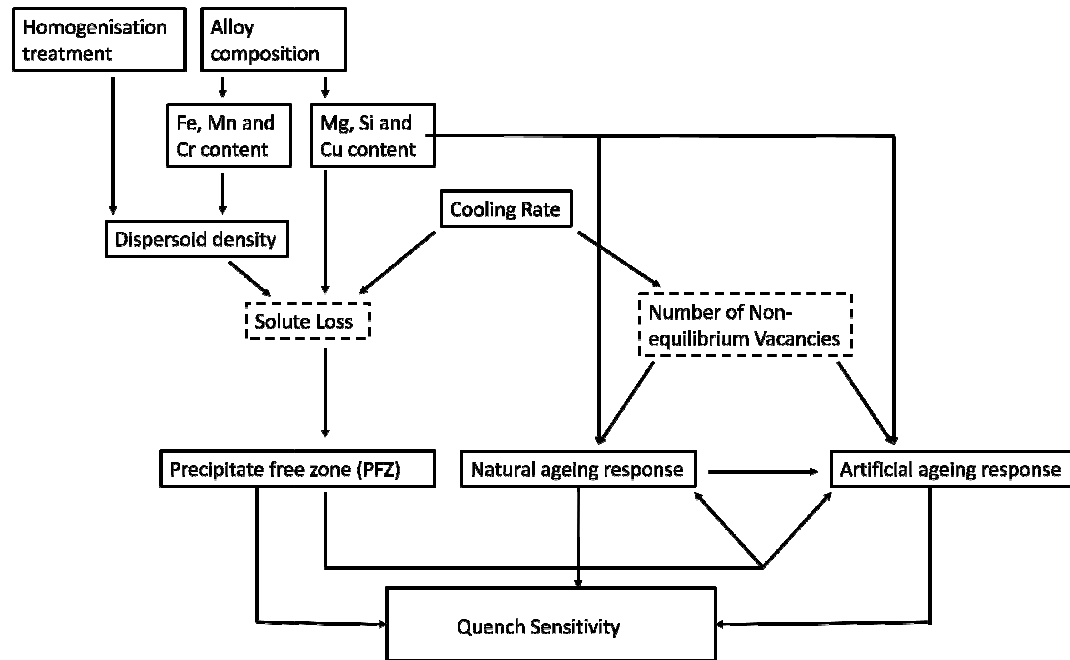
Figure 8-15 Schematic showing the alloy and processing parameters affecting quench sensitivity in Al-Mg-Si alloys.
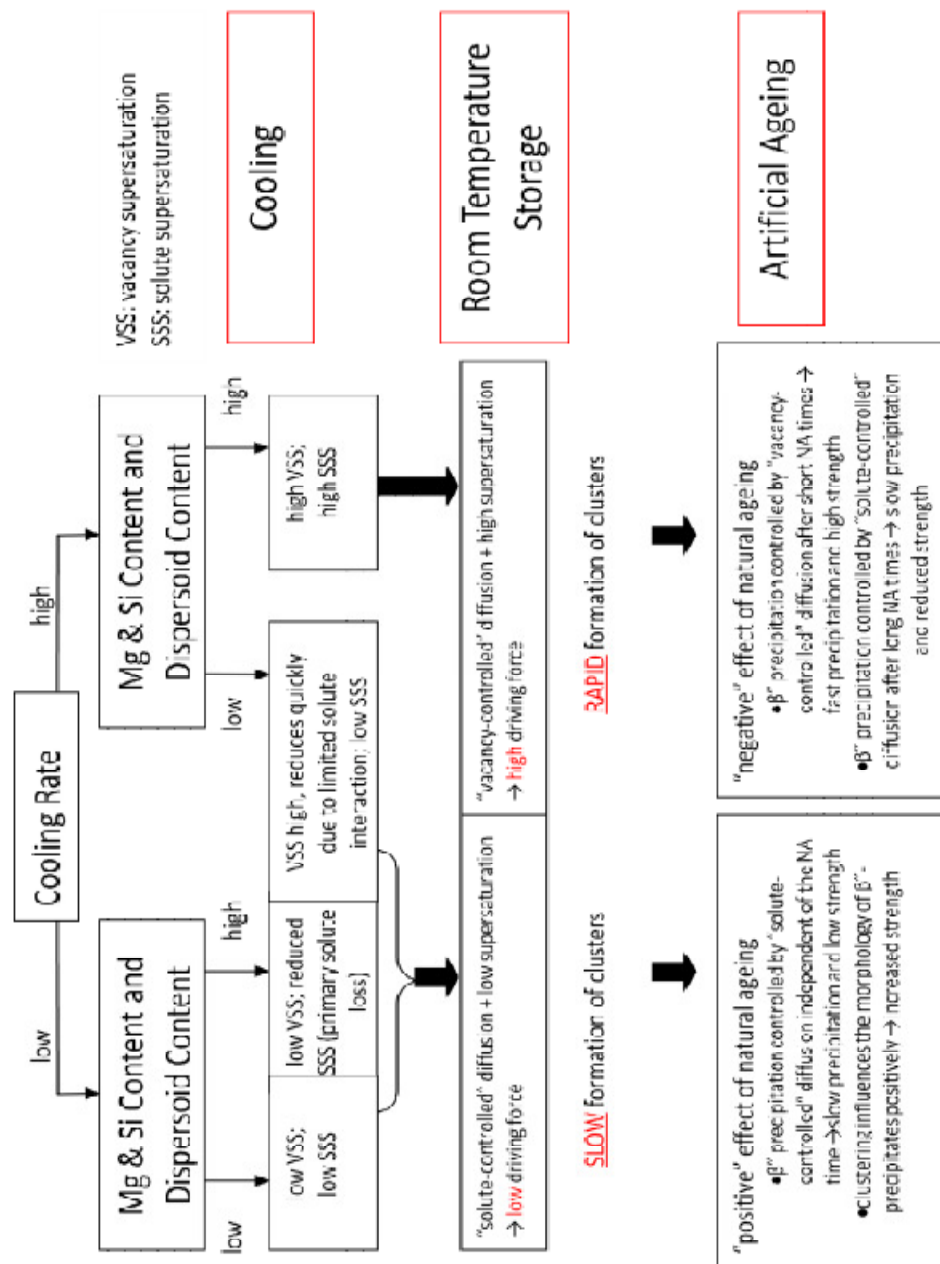
Figure 8-16 Schematic of the conclusions drawn from this work in regards to solute loss and effect of natural ageing.

Chapter 9   Conclusions and Recommendations for Future Work

9.1 Conclusion

The aim of this work was to describe the physical mechanisms behind quench sensitivity in Al-Mg-Si alloys. The results from this study allow conclusions on the key contributors to quench sensitivity and their mechanisms. Furthermore, conclusions on the mechanisms behind natural ageing can be drawn:

- **Quench Sensitivity is the result of both solute loss and a reduced vacancy supersaturation**

Artificial ageing curves after three different natural ageing times show that the difference in hardness between fast and slow cooled samples is not constant. Solute loss was found to be limited to a zone around non-hardening precipitates that had formed on heterogeneous nucleation sites during slow cooling from extrusion or solution treatment temperature. The difference in hardening response is therefore not driven by a difference in solute content but is the result of a cooling rate dependent difference in vacancy super-saturation.

As the concentration of mobile, non-equilibrium vacancies decreases with increasing natural ageing time, its contribution to quench sensitivity decreases as well. Therefore, quench sensitivity is the result of a nearly constant contribution of solute loss and a natural ageing time dependent contribution of vacancy supersaturation. Solute loss is the dominant contributor to quench sensitivity when the difference in vacancy concentration is low and age hardening is driven by the equilibrium vacancy concentration at artificial ageing temperature, i.e. after long natural ageing times.

- **<u>The dispersoid density is the determining factor for solute loss</u>**

The material parameter that influences solute loss most is the density of secondary dispersoids, whereas the Mg-, Si- and Cu-content have little effect on the size, composition and crystal structure of the non-hardening precipitates forming during slow cooling from extrusion or solution treatment temperature. The dispersoid density itself is determined by the homogenisation parameters time and temperature as well as the transition metal content.

- **<u>Quenched-in vacancies affect the formation of clusters and strengthening precipitates</u>**

The concentration of mobile, non-equilibrium vacancies varies by several orders of magnitude depending on the cooling rate. It appears that for alloys with relatively high solute contents (Mg+Si greater than 1 wt.%) vacancies are able to interact with solute and affect precipitation, where as low solute-vacancy interaction in lean alloys (Mg+Si less than 1wt.%) reduces the effect of vacancies significantly. If present, their effect on age hardening is twofold:

1. by acting as nucleation sites for the coherent precursors of the strengthening β''-phase

2. by enhancing diffusion kinetics and hence the rate of age hardening

DSC during heating after cooling at different rates indicated that the formation of the major strengthening β''-precipitate is suppressed in slow cooled samples. This is explained by the absence of non-equilibrium vacancies as precipitation sites for the β''-precursor phases in slow cooled samples. In contrast, in fast cooled samples a high density of vacancies provides nucleation sites for coherent clusters and GP-zones leading to a dense distribution of β''-precipitates. The precipitation sequence is therefore dependent on the cooling rate.

A high vacancy supersaturation in fast cooled samples leads to enhanced diffusion kinetics and hence to rapid hardness increases during artificial ageing after short natural ageing times. Low cooling rates and/or prolonged natural ageing times lead to a low vacancy concentration, often lower than the equilibrium vacancy concentration at the artificial ageing temperature. As a result, precipitation is driven by the equilibrium vacancy concentration at artificial ageing temperature and the hardening increase is slow.

- **Whether natural ageing has a negative effect or not is dependent on the solute content as well as the vacancy supersaturation after quenching**

In samples, where the age hardening response is greatly enhanced by the presence of vacancies, i.e. fast cooled samples of alloys with combined Mg+Si-contents greater than 1 wt.%, natural ageing has a negative effect on the artificial ageing response. The decrease in vacancy supersaturation with increasing natural ageing time causes a decrease in diffusion kinetics and therefore a negative effect of natural ageing.

In contrast, in samples where vacancies do not enhance age hardening after short natural ageing times, i.e. in slow cooled samples and/or samples with a low solute content, age hardening is always driven by the vacancy concentration at artificial ageing temperature. Clusters forming during natural ageing time most likely contribute to strength and hardness and hence have a positive effect on the overall age hardening performance.

9.2 Future Work

Whilst this work offers reasonable explanations for quench sensitivity being the result of both solute loss and cooling rate dependent differences in vacancy concentration, there are a number of areas where more detailed testing and validation would be useful.

- **Clustering during natural ageing:** In fast cooled samples containing a combined Mg+Si content > 1 wt.% natural ageing is known to have a negative effect, which has been attributed to solute loss to stable clusters that do not act as precipitation sites for the strengthening β''-phases [81, 90]. However, the present study suggests that the decrease in mobile, non-equilibrium vacancies with increasing natural ageing time also contributes to the decrease in artificial ageing response in these fast cooled samples. In contrast, slow cooled samples of the same alloys showed higher peak hardness values during artificial ageing after longer natural ageing times.

  A three dimensional atom probe (3DAP) study of the microstructure of slow cooled samples in comparison to that of fast cooled samples could assist with clarifying the role of clusters on the effect of natural ageing. By firstly investigating the cluster size distribution and composition after prolonged natural ageing it should be clarified whether the same type of clusters precipitate in fast and slow cooled samples. Secondly, investigating the microstructure after prolonged natural ageing and subsequent artificial ageing will reveal whether clusters co-exist with β''-precipitates and hence directly contribute to strength and hardness, or whether these clusters act as precipitation sites for the strengthening β''-precipitates. From this one can make conclusions on the role of clusters in the negative effect of natural ageing in fast cooled samples and rationalise the influence of changes in the concentration of mobile, non-equilibrium vacancies.

- **Precipitates present at peak hardness:** Although there has been a significant amount of work [11, 67, 76, 105] published on the precipitation sequence of strengthening phases in Al-Mg-Si, little is known about precipitation in slow cooled samples as precipitation is typically investigated in fast cooled samples. In order to confirm whether there are cooling rate dependent changes in the precipitation sequence, the strengthening precipitates at the respective peak hardness of air cooled and water quenched samples should be investigated

using TEM. This will clarify whether the precipitation of β" is suppressed or retarded.

- **<u>The role of vacancies on clustering and precipitation:</u>** Recently, Pogatscher et al. [43, 150] proposed that vacancies act as nucleation sites for the β"-precursors and hence lead to an enhanced age hardening response. The results from this work show that the presence of non-equilibrium vacancies enhances the age hardening response significantly. Besides the improvement by providing nucleation sites it is also suggested that diffusion is significantly enhanced by the presence of non-equilibrium vacancies. A study on quantifying the contributions of nucleation and diffusion enhanced by non-equilibrium vacancies to age hardening could lead to a greater understanding of clustering and precipitation.

- **<u>Combined model considering solute loss and cooling rate dependent vacancy concentration:</u>** The present study has shown that the age hardening response of age-hardenable, wrought aluminium alloys is dependent on the cooling rate dependent concentration of non-equilibrium vacancies and distribution of strengthening precipitates, i.e. the size of the precipitates free zones. These findings can make a valuable contribution to the development of physical models.

The formation of precipitate free zones as a function of cooling rate and dispersoid density can be implemented in a model describing the precipitation of clusters and strengthening precipitates as a function of vacancy concentration. A satisfying model for dispersoid density as a function of alloy composition and homogenisation conditions is provided by Dons [147]. The model developed by Fischer, Falahati and Lang et al. [37, 39, 41, 48] predicts the vacancy supersaturation as a function of cooling rate, annihilation of vacancies during natural ageing and precipitation of clusters and strengthening precipitates and is therefore considered the most promising basis for a model predicting quench sensitivity.

References

[1] http://www.alueurope.eu/, accessed 04.03.2013

[2] I. Polmear, Light Alloys, Butterworth-Heinemann, 2005, p. 1-416.

[3] O. Lohne, A. L. Dons, Scandinavian Journal of Metallurgy 12 (1983) 34-36.

[4] H. Zoller, A. Ried, Zeitschrift Metallkunde 62 (1971) 5.

[5] B. Milkereit, N. Wanderka, C. Schick, O. Kessler, Materials Science and Engineering: A (2012).

[6] R. T. Shuey, A. J. Den Bakker, Relating strength loss to solute loss in a 6xxx alloy, in: Materials Solution Conference, ASM International, Indianapolis, IN, United states, 2001, pp. 189-194.

[7] T. A. Association, Registration Record Series Teal Sheets, Arlinton, VA, 2009

[8] E. D. Sweet, B. R. Harker, X. Zhang, M. J. Couper, Quench sensitivity test method for aluminium extrusion alloys, in: E. T. Foundation (Ed.) Preceedings of the Ninth International Aluminum Extrusion Technilogy Seminar, vol 1, ET Foundation, Orlando, 2008, pp. 415-424.

[9] H. W. Zandbergen, S. J. Andersen, J. Jansen, Science 277 (1997) 1221-1225.

[10] S. J. Andersen, H. W. Zandbergen, J. Jansen, C. Traeholt, U. Tundal, O. Reiso, Acta Materialia 46 (1998) 3283-3298.

[11] G. A. Edwards, K. Stiller, G. L. Dunlop, M. J. Couper, Acta Materialia 46 (1998) 3893-3904.

[12] M. J. Couper, G. A. Edwards, 6XXX series aluminium alloy, in: C. A. Limited (Ed.) vol US 6,364,969 B1, United States, 2002, p. 7.

[13] S. Zajac, B. Hutchinson, A. Johansson, L. O. Gullman, Materials Science and Technology 10 (1994) 323-333.

[14] J. E. Tibballs, J. A. Horst, C. J. Simensen, Journal of Materials Science 36 (2001) 937-941.

[15] N. C. W. Kuijpers, E. Vermolen, C. Vuik, P. T. G. Koenis, K. E. Nilsen, S. van der Zwaag, Materials Science and Engineering A 394 (2005) 9-19.

[16] N. C. Parson, H. L. Yiu, Light Metals (1989) 713-724.

[17] M. Qian, D. H. StJohn, S. Maloney, M. J. Couper, Materials Science Forum 396-402 (2002) 191-196.

[18] L. Katgerman, D. G. Eskin, Material Science Forum 710 43-49.

[19] M. H. Mulazimoglu, A. Zaluska, J. E. Gruzleski, F. Paray, Metallurgical and Materials Transactions A: Physical Metallurgy and Materials Science 27 A (1996) 929-936.

[20] O. Reiso, The effect of composition and homogenization treatment on extrudability of AlMgSi alloys, in: A. E. Council (Ed.) ET 1984: Third International Aluminum Extrusion Technology Seminar, ET Foundation, Atlanta, Georgia, 1984, pp. 31-40.

[21] J. W. Evancho, J. T. Staley, Metallurgical Transactions 5 (1974) 43-47.

[22] D. W. Pashley, M. H. Jacobs, J. T. Vietz, Philosophical Magazine 16 (1967) 51-76.

[23] H. Bomas, Fortschritt-Berichte der VDI-Zeitschriften, Reihe 5: Grund- und Werkstoffe (1980).

[24] D. L. Zhang, L. Zheng, Metallurgical and Materials Transactions A (Physical Metallurgy and Materials Science) 27A (1996) 3983-3991.

[25] P. A. Rometsch, S. C. Wang, A. Harriss, P. J. Gregson, M. J. Starink, Materials Science Forum 396-402 (2002) 655-660.

[26] D. H. Bratland, O. Grong, H. Shercliff, O. R. Myhr, S. Tjotta, Acta Materialia 45 (1997) 1-22.

[27] D. A. Porter, K. E. Easterling, M. Y. Sherif, Phase transformations in matals and alloys, CRC Press, 2009.

[28] I. Musulin, O. C. Celliers, Light Matals 1990 (1990) 951-954.

[29] J. Yoo, Journal of Materials Science 34 (1999) 2679.

[30] H. Westengen, L. Auran, O. Reiso, Aluminium Dusseldorf 56 (1980) 768-775.

[31] L. Lodgaard, N. Ryum, Materials Science and Engineering A 283 (2000) 144-152.

[32] H. Hirasawa, Scripta Metallurgica 9 (1975) 955-958.

[33] L. Lodgaard, N. Ryum, Aluminum Transactions 2 (2000) 267-275.

[34] L. Lodgaard, N. Ryum, Materials Science and Technology 16 (2000) 599-604.

[35] L. Lodgaard, N. Ryum, Material Science Forum 331-337 (2000) 945-950.

[36] J. E. Yoo, A. Shan, I. G. Moon, S. J. Maeng, Journal of Materials Science 34 (1999) 2679-2683.

[37] A. Falahati, P. Lang, E. Kozeschnik, Materials Science Forum 706-709 (2012) 317-322.

[38] A. Deschamps, G. Texier, S. Ringeval, L. Delfaut-Durut, Materials Science and Engineering A 501 (2009) 133-139.

[39] P. Lang, A. Falahati, M. R. Ahmadi, P. Warczok, E. Povoden-Karadeniz, E. Kozeschnik, R. Radis, Modeling the influence of cooling rate on the precipitate evolution in Al-Mg-Si (Cu) alloys, in: Phase Stability, Diffusion, Kinetics and their Applications, Columbus, Ohio, 2011, pp. 284-291.

[40] R. C. Picu, X. Zhijie, Scripta Materialia 57 (2007) 45-48.

[41] F. D. Fischer, J. Svoboda, F. Appel, E. Kozeschnik, Acta Materialia 59 (2011) 3463-3472.

[42] B. Klobes, T. E. M. Staab, M. Haaks, K. Maierand, I. Wieler, Physica Status Solidi - Rapid Research Letters 2 (2008) 224-226.

[43] S. Pogatscher, H. Antrekowitsch, H. Leitner, T. Ebner, P. J. Uggowitzer, Acta Materialia 59 (2011) 3352-3363.

[44] H. S. Zurob, H. Seyedrezai, Scripta Materialia 61 (2009) 141-144.

[45] C. Wolverton, Acta Materialia 55 (2007) 5867-5872.

[46] H. Seyedrezai, D. Grebennikov, P. Mascher, H. S. Zurob, Materials Science and Engineering A 525 (2009) 186-191.

[47] S. Esmaeili, D. Vaumousse, M. W. Zandbergen, W. J. Poole, A. Cerezo, D. J. Lloyd, Philosophical Magazine 87 (2007) 3797-3816.

[48] A. Falahati, M. R. Ahmadi, P. Warczok, P. Lang, E. Povoden-Karadeniz, E. Kozeschnik, Thermo-kinetic computer simulation of precipitation and age-hardening effect in Al-Mg-Si alloyswith arbitrary heat treatment, in: Phase Stability, Diffusion, Kinetics and their Applications, Columbus, Ohio, 2011, pp. 292-299.

[49] B. Milkereit, Kontinuierliche zeit-temperatur-ausscheidungs-diagramme von Al-Mg-Si-Legierungen, Doktor-Ingenieur, Universität Rostock, 2010

[50] B. Milkereit, C. Schick, O. Kessler, Continuous cooling precipitation diagrams depending on the composition of aluminium-magnesium-silicon alloys, in: s. Kumai, O. Umezawa, Y. Takayama, T. Tsuchida, T. Sato (Eds.), The 12th International Conference on Aluminium Alloys, The Japan Institute of Light Metals, Yokohama, 2010, pp. 407-412.

[51] S. Ma, M. Maniruzzaman, S. R.D.Jr, Application of Joniny end quench for the development of quench factor analysis and microstructure prediction of cast Al-Si-Mg-alloys, in: International Conference of Solid to Soild Phase Transformations in Organic Materials Phoenix, 2005.

[52] G. E. Totten, D. S. Mackenzie, Materials Science Forum 331-337 (2000) 589-594.

[53] B. Milkereit, O. Kessler, C. Schick, Thermochimica Acta 492 (2009) 73-78.

[54] P. A. Rometsch, M. J. Starink, P. J. Gregson, Materials Science and Engineering A 339 (2003) 255-264.

[55] J. T. Staley, Materials Science and Technology 3 (1987).

[56] J. T. Staley, R. D. Doherty, A. D. Jaworski, Metallurgical Transactions 24A (1993).

[57] ASTM, Standard Test Methods for Determining Hardenability of Steel, West Conshockon, 2006

[58] A. Bryant, Journal of the Institute of Metals 90 (1961) 406-409.

[59] W. G. J. 't Hart, H. J. Kolkman, L. Schra, The Jominy end-quench test for investigation of corrosion properties and microstructure of high strength aluminium alloys, in: National Aerospace Laboratory NLR, Amsterdam, 1980, p. 47.

[60] B. Milkereit, M. Beck, M. Reich, O. Kessler, C. Schick, Thermochimica Acta 522 (2011) 86-95.

[61] J. W. Cahn, Acta Metallurgica 4 (1956) 572-575.

[62] R. T. Shuey, T. M., K. B. Lippert, Mathematical pitfalls in modeling quench sensitivity of aluminum alloys, in: 1st Interantional Symposium on Metallurgical Modeling for Aluminum Alloys, Pittsburg, 2003.

[63] G. P. Dolan, R. J. Flynn, D. A. Tanner, J. S. Robinson, Materials Science and Technology 21 (2005) 687-692.

[64] M. Tsukuda, S. Koike, M. Harada, Journal of Japan Institute of Light Metals 28 (1978) 8-14.

[65] W. F. Miao, D. E. Laughlin, Metallurgical and Materials Transactions A: Physical Metallurgy and Materials Science 31 (2000) 361-371.

[66] M. Torsater, R. Vissers, C. Marioara, S. Andersen, R. Holmestad, Crystal structure determinationof the Q' and C-type plate precipitates in Al-Mg-Si-Cu (6xxx) alloys, in: J. Hirsch, B. Skrotzki, G. Gottstein (Eds.), 11th International Conference on Aluminium Alloys, vol 2, Wiley-VHC, Aachen, Germany, 2008, pp. 1338-1344.

[67] D. J. Chakrabarti, Y. Peng, D. E. Laughlin, Materials Science Forum 396-402 (2002) 857-862.

[68] W. F. Miao, D. E. Laughlin, Scripta Materialia 40 (1999) 873-878.

[69] C. Ravi, C. Wolverton, Acta Materialia 52 (2004) 4213-4227.

[70] C. D. Marioara, S. J. Andersen, J. Jansen, H. W. Zandbergen, Acta Materialia 49 (2001) 321-328.

[71] K. Matsuda, S. Ikeno, S. Tada, Journal of the Japan Institute of Metals 57 (1993) 1107-1113.

[72] M. H. Jacobs, Philosophical Magazine 26 (1972) 1-13.

[73] K. Matsuda, S. Tada, S. Ikeno, Journal of Electron Microscopy 42 (1993) 1-6.

[74] S. J. Andersen, C. D. Marioara, A. Frseth, R. Vissers, H. W. Zandbergen, Materials Science and Engineering A 390 (2005) 127-138.

[75] R. Vissers, M. A. van Huis, J. Jansen, H. W. Zandbergen, C. D. Marioara, S. J. Andersen, Acta Materialia 55 (2007) 3815-3823.

[76] K. Matsuda, V. Sakaguchi, V. Miyata, V. Uetani, T. Sato, A. Kamio, S. Ikeno, Journal of Materials Science 35 (2000) 179-189.

[77] S. J. Andersen, C. D. Marioara, R. Vissers, A. Froseth, H. W. Zandbergen, Materials Science & Engineering A (Structural Materials: Properties, Microstructure and Processing) 444 (2007) 157-169.

[78] S. D. Dumolt, D. E. Laughlin, J. C. Williams, Scripta Metallurgica 18 (1984) 1347-1350.

[79] L. Arnberg, B. Aurivillius, Acta Chem. Scand. A 34 (1980) 1.

[80] J. F. Nie, B. C. Muddle, H. I. Aaronson, S. P. Ringer, J. P. Hirth, Metallurgical and Materials Transactions A (Physical Metallurgy and Materials Science) 33A (2002) 1649-1658.

[81] M. Murayama, K. Hono, Acta Materialia 47 (1999) 1537-1548.

[82] A. Wilm, Metallurgie 8 (1911) 25.

[83] A. Guinier, Nature 142 (1938) 569.

[84] A. Preston, Nature 142 (1938) 570.

[85] D. W. Pashley, J. W. Rhodes, A. Sendorek, Journal of the Institute of Metals 94 (1966) 41-49.

[86] T. Hirata, S. Matsuo, Transactions of the Japan Institute of Metals 13 (1972) 231-237.

[87] H. Bichsel, A. Ried, Wärmebehandlung (1973).

[88] J. Royset, T. Stene, J. A. Saeter, O. Reiso, Materials Science Forum 519-521 (2006) 239-244.

[89] S. Pogatscher, H. Antrekowitsch, T. Ebner, P. J. Uggowitzer, Light Metals 2012 (2012) 415-420.

[90] C. S. T. Chang, J. Banhart, Metallurgical and Materials Transactions A 42 (2010) 1960-1964.

[91] A. Serizawa, S. Hirosawa, T. Sato, Materials Science Forum 519-521 (2006) 245-250.

[92] M. J. Starink, L. F. Cao, P. A. Rometsch, Acta Materialia 60 (2012) 4194-4207.

[93] P. A. Rometsch, L. F. Cao, X. Y. Xiong, B. C. Muddle, Ultramicroscopy 111 (2011) 690-694.

[94] M. D. H. Lay, H. S. Zurob, C. R. Hutchinson, T. J. Bastow, A. J. Hill, Metallurgical and Materials Transactions A: Physical Metallurgy and Materials Science (2012) 1-7.

[95] J. Banhart, C. S. T. Chang, Z. Liang, N. Wanderka, M. D. H. Lay, A. J. Hill, Advanced Engineering Materials 12 (2010) 559-571.

[96] J. Banhart, M. D. H. Lay, C. S. T. Chang, A. J. Hill, Physical Review B (Condensed Matter and Materials Physics) 83 (2011).

[97] J. Banhart, M. Liu, Y. Yong, Z. Liang, C. S. T. Chang, M. Elsayed, M. D. H. Lay, Physica B: Condensed Matter 407 (2012) 2689-2696.

[98] C. S. T. Chang, I. Wieler, N. Wanderka, J. Banhart, Ultramicroscopy 109 (2009) 585-592.

[99] M. Murayama, K. Hono, M. Saga, M. Kikuchi, Materials Sience and Engineering A A250 (1998) 127-132.

[100] A. I. Morley, M. W. Zandbergen, A. Cerezo, G. D. W. Smith, Materials Science Forum 519-521 (2006) 543-548.

[101] S. Esmaeili, D. J. Lloyd, Scripta Materialia 50 (2004) 155-158.

[102] C. D. Marioara, S. J. Anderson, J. Jansen, H. W. Zandbergen, Acta Materialia 51 (2003) 789-796.

[103] K. Matsuda, S. Taniguchi, K. Kido, Y. Uetani, S. Ikeno, Materials Transactions 43 (2002) 2789-2795.

[104] M. J. Couper, 6XXX series aluminium alloy, in: 2002.

[105] A. K. Gupta, D. J. Lloyd, S. A. Court, Materials Science & Engineering A (Structural Materials: Properties, Microstructure and Processing) A316 (2001) 11-17.

[106] T. Saito, S. Muraishi, C. Marioara, R. Holmestad, Effect of low Cu amounts and pre-deformation on the precipitationin Al-Mg-Si alloys, in: H. Weiland, A. Rollett, W. Cassada (Eds.), 13th International Conference on Aluminum Alloys (ICAA13), TMS (The Minerals, Metals & Materials Society), Pittsburgh, PA, 2012, pp. 1063-1068.

[107] M. Murayama, K. Hono, W. F. Miao, D. E. Laughlin, Metallurgical and Materials Transactions A (Physical Metallurgy and Materials Science) 32A (2001) 239-246.

[108] S. Zajac, B. Bengtsson, A. Johansson, L.-O. Gullman, Materials Science Forum 217-222 (1996) 397-402.

[109] J. Holze, R. Ehlers, B. Beyer, Neue Huette 22 (1977) 29-32.

[110] T. F. Morgeneyer, M. J. Starink, S. C. Wang, I. Sinclair, Acta Materialia 56 (2008) 2872-2884.

[111] B. Milkereit, N. Wanderka, C. Schick, O. Kessler, Materials Science and Engineering A 550 (2012) 87-96.

[112] M. J. Starink, International Materials Reviews 49 (2004) 191-226.

[113] Y. Birol, Journal of Thermal Analysis and Calorimetry 93 (2008) 977-981.

[114] M. J. Starink, P. J. Gregson, Scripta Metallurgica et Materialia 33 (1995) 893-900.

[115] M. J. Starink, Thermochimica Acta 404 (2003) 163-176.

[116] http://emaps.mrl.uiuc.edu/, J. M. Zuo, M. J.C., Editor, accessed

[117] R. Ferragut, A. Somoza, A. Dupasquier, Journal of Physics: Condensed Matter 10 (1998) 3903-3918.

[118] G. Dlubek, Material Science Forum 13-14 (1987) 11-32.

[119] M. Lay, H. Zurob, C. Hutchinson, T. Bastow, A. Hill, Metallurgical and Materials Transactions A (2012) 1-7.

[120] A. Somoza, A. Dupasquier, I. J. Polmear, P. Folegati, R. Ferragut, Physical Review B (Condensed Matter) 61 (2000) 14454-14463.

[121] A. Dupasquier, G. Kogel, A. Somoza, Acta Materialia 52 (2004) 4707-4726.

[122] I. Kohlbach, B. Korff, T. Staab, Physica Status Solidi B 247 (2010) 2168-2178.

[123] R. Krause-Rehberg, H. S. Leipner, Positron Annihilation in Semiconductors, Springer, Berlin, 1999.

[124] T. E. M. Staab, B. Klobes, I. Kohlbach, B. Korff, M. Haaks, E. Dudzik, K. Maier, Journal of Physics: Conference Series 265 (2011).

[125] P. Folegati, I. Makkonen, R. Ferragut, M. J. Puska, Physical Review B (Condensed Matter and Materials Physics) 75 (2007) 54201-54201.

[126] J. M. Campillo Robles, E. Ogando, F. Plazaola, Calculation of Positron Characteristics for Elements of the Periodic Table, in: International Workshop on Positron Studies of Defects, vol 265, IOP Publishing Ltd., UK, 2011, pp. 1-10.

[127] J. Kansy, Nuclear Instruments and Methods in Physics Research Section A: Accelerators, Spectrometers, Detectors and Associated Equipment 374 (1996) 235-244.

[128] L. Cao, P. A. Rometsch, H. Zhong, Y. Mulji, S. Gao, B. C. Muddle, Effect of Natural Ageing on the Artificial Ageing Response of an Al-Mg-Si-Cu Alloy, in: S. Kumai, O. Umezawa, Y. Takayama, T. Tsuchida, T. Sato (Eds.), 12th International Conference on Aluminium Alloys, The Japan Institude of Light Metals, Yokohama, 2010, pp. 395-400.

[129] A. Serizawa, S. Hirosawa, T. Sato, Metallurgical and Materials Transactions A 39 (2008) 243-251.

[130] K. Strobel, E. Sweet, M. Easton, J.-F. Nie, M. Couper, Dispersoid phases in 6xxx series aluminium alloys, in: A. M. J.-F. Nie (Ed.) The 7th Pacific Rim International Conference on Advanced Materials and Processing, vol 654-656, Trans Tech Publications Ltd, Cairns, QLD, Australia, 2010, pp. 926-929.

[131] K. Yamada, T. Sato, A. Kamio, Material Science Forum 331-337 (2000) 669-674.

[132] K. Strobel, M. A. Easton, L. Sweet, M. J. Couper, J.-F. Nie, Materials Transactions 52 (2011) 914-919.

[133] M. Manninen, R. Nieminen, P. Hautojarvi, J. Arponen, Physical Review B (Solid State) 12 (1975) 4012-4022.

[134] A. Seeger, F. Banhart, Physica Status Solidi A 102 (1987) 171-179.

[135] M. D. H. Lay, H. S. Zurob, C. R. Hutchinson, T. J. Bastow, A. J. Hill, Metallurgical and Materials Transactions A accepted (2012).

[136] O. Reiso, J. Royset, J. A. Saeter, U. Tundal, G. Gjertsen, Al-Mg-Si alloy suited for extrusion, in: vol US 2007/0039669 A1, Norsk Hydro ASA, US, 2004.

[137] A. Ried, P. Schwellinger, H. Bichsel, Aluminium 53 (1977) 595-599.

[138] M. A. Gaffar, A. Gaber, M. S. Mostafa, E. F. A. Zeid, Journal of Alloys and Compounds 429 (2007) 167-175.

[139] M. J. Starink, Journal of Alloys and Compounds 433 (2007) 4-6.

[140] Y. Du, Y. A. Chang, H. Baiyun, G. Weiping, J. Zhanpeng, X. Honghui, Y. Zhaohui, L. Yong, H. Yuehui, F. Y. Xie, Materials Science & Engineering A (Structural Materials: Properties, Microstructure and Processing) A363 (2003) 140-151.

[141] M. G. Ortega, S. B. R. De Debiaggi, A. M. Monti, Physica Status Solidi B 234 (2002) 506-521.

[142] Z. Liang, C. S. T. Chang, N. Wanderka, J. Banhart, J. Hirsch, The effect of Fe, Mn and trace elements on precipitation in Al-Mg-Si alloy, in: 12th International Conference on Aluminium Alloys, The Japan Institute of Light Metals, Yokohama, Japan, 2010, pp. 492-497.

[143] C. Panseri, T. Federighi, Institute of Metals -- Journal 94 (1966) 99-107.

[144] K. Matsuda, R. Fujii, T. Kawabata, Y. Uetani, S. Ikeno, Journal of Japan Institute of Light Metals 51 (2001).

[145] K. Matsuda, Metallurgical and Materials Transactions; A; Physical Metallurgy and Materials Science 36 (2005) 2007-2012.

[146] C. D. Marioara, Metallurgical and Materials Transactions; A; Physical Metallurgy and Materials Science 36A (2005) 691-702.

[147] A. L. Dons, Journal of Light Metals (2001) 133-149.

[148] C. Cayron, P. A. Buffat, Acta Materialia 48 (2000) 2639-2653.

[149] S. Pogatscher, H. Antrekowitsch, H. Leitner, A. S. Sologubenko, P. J. Uggowitzer, Scripta Materialia 68 (2013) 158-161.

[150] S. Pogatscher, H. Antrekowitsch, H. Leitner, D. Poeschmann, Z. L. Zhang, P. J. Uggowitzer, Acta Materialia 60 (2012) 4496-4497.